DISSERTATION

DEVELOPMENT OF A PREDICTION MODEL FOR WINDBORNE DEBRIS DAMAGE ASSESSMENT OF COAST COMMUNITIES UNDER HURRICANES

Submitted by

Yue Dong

Department of Civil and Environmental Engineering

In partial fulfillment of the requirements

For the Degree of Doctor of Philosophy

Colorado State University

Fort Collins, Colorado

Fall 2023

Doctoral Committee:

Advisor: Yanlin Guo

John W. van de Lindt
Bruce R. Ellingwood
Xinfeng Gao

ABSTRACT

DEVELOPMENT OF A PREDICTION MODEL FOR WINDBORNE DEBRIS DAMAGE ASSESSMENT OF COAST COMMUNITIES UNDER HURRICANES

Urban high-rise building envelopes may suffer severe damage induced by windborne debris during hurricanes. Breaches in urban building envelopes may lead to cascading building content loss due to rain intrusion and building functionality loss for long periods of time, thus disrupting the resilience of urban coastal communities. Such a societal disruption may become worse due to the rapid growth of population and development of economy in coastal communities. Objective of this dissertation is to develop an efficient prediction model for assessing windborne debris damage to building envelopes and apply it to the hurricane scenarios identified through a de-aggregation process to enable risk-informed resilience assessment of coastal communities for windborne debris impact. A set of scenario hurricanes corresponding to a stipulated return period (RP) for resilience assessment of coastal communities for debris impact is systematically identified using the de-aggregation approach proposed in this dissertation. The existing building envelope damage assessment models for urban high/mid-rise buildings often neglect the geometry of building clusters or simply assume a homogeneous configuration, which can introduce errors and uncertainties for urban building clusters with varying geometries and layouts. This dissertation proposes a new fragility modeling approach for urban buildings envelopes, which explicitly considers geometric configurations of urban buildings, to improve the accuracy of risk assessment for urban buildings. Estimating the urban wind field that drives the debris flight is critical for constructing fragilities for debris damage. The traditional tools for simulating urban wind fields,

such as wind tunnel tests and Computational Fluid Dynamic (CFD), are usually expensive or time-consuming for complex urban environments and cannot offer an efficient prediction of the urban wind field that is sufficient for risk assessment at a community level. Therefore, an efficient machine learning (ML) based prediction model of wind fields around building clusters is proposed using conditional Generative Adversarial Networks (cGANs). Uncertainty analysis is conducted on the models and parameters involved in this procedure of debris damage assessment. The uncertainty in the final prediction of windborne debris damage is evaluated through uncertainty propagation among models and parameters. Sensitivity analysis with some critical factors is also conducted to identify the dominant contributors to the uncertainty in the estimation of debris damage. In the end, windborne debris damage on building envelopes in virtual communities under synthetic hurricanes scenarios is investigated to illustrate the damage assessment procedure for windborne debris impact at the community level.

ACKNOWLEDGEMENTS

I would like to express my deep appreciation to my advisor Dr. Yanlin Guo for her great guidance and encouragement over the past five years. I am grateful to the opportunity she gave to work on my dissertation research topics. Her knowledge and patience have enabled me to overcome challenges. Without her patience and encouragement, the completion of my dissertation would not have been possible.

I would also like to thank my committee members, Dr. John W. van de Lindt, Dr. Bruce R. Ellingwood, and Dr. Xinfeng Gao for their invaluable suggestions and comments to this dissertation.

In addition, I would like to thank my friends in Colorado State University, Qilin Zou, Lisa Wang, Min Li, and Perry Brandon. Their friendship and support help me a lot.

Last but not least, I would like to thank my parents and my brother for their support and understanding throughout my research journey.

DEDICATION

To my parents

TABLE OF CONTENT

LIST OF TABLES

LIST OF FIGURES

CHAPTER 1 INTRODUCTION

1.1 Background and motivation

Hurricanes pose an increasing threat to structures along coasts worldwide (Snaiki et al 2020). Rapid urbanization in coastal areas has prompted more exposure of high /mid-rise buildings to hurricane strikes. Therefore, understanding the hurricane risk to urban high-rise/mid-rise buildings is critical for reducing the potential economic loss and enhancing the community's resilience. The damage patterns of high/mid-rise buildings under hurricanes are significantly different from those of low-rise buildings, which normally include failure of roof, wall, and wall-to-roof connections (Sparks et.al 1994; Li and Ellingwood 2006; van de Lindt et al. 2007). Urban high/mid-rise buildings have fully engineered main wind force-resisting systems, which perform very well with stresses remaining in the elastic range during hurricanes (Kareem 1985). However, the non-structural building envelope components such as façade and cladding systems, especially the glass portion, often experience damage due to windborne debris impact (Kareem and Bashor 2006). Apart from wind pressure, surveys over the past three decades have revealed that missile impact from windborne debris is one of the most important damage sources to building envelopes, which may cause more than 80% of glass breakage (Neunlist 1983; Kareem 1986). Recently, the broken windows of the Capital One Tower in Lake Charles, Louisiana, during Hurricane Laura in 2020 indicated unusual damage mechanisms. The preliminary analysis revealed that the combined air pressure and windborne debris generated from previously broken glass may have been the source of damage (Giusti 2020), which coincides with what was reported in large-scale field observations of window damage of over 500 buildings in Hong Kong (Yu et.al 2020) during Typhoon Mangkhut in 2018. The envelope damage then becomes the driver of the cascading interior damage due to water intrusion from the breached building envelope (Minor 2005). Therefore, modeling glass façade and cladding damage due to debris impact are crucial in assessing the risk of urban buildings under hurricane hazards. An accurate and effective prediction model for debris impact damage under hurricane scenarios, as the first step, is critical for risk mitigation and enhanced the resilience of the community against such hazards.

The framework of community resilience assessment for debris impact damage requires fragility models for damage assessment. Unlike low-rise structures and residential buildings, which are typically homogeneously distributed and often only one to three stories, urban high /mid-rise buildings have exhibited themselves with various shapes, highly varying heights, and layouts and can modify the surrounding urban wind field, thus representing unique and yet unsolved challenges in fragility analysis and development. Indeed, compared to the vast existing literature on the fragility/vulnerability of low-rise buildings (Rosowsky and Ellingwood 2002; Ellingwood et al. 2004; van de Lindt and Dao 2009) the research on urban high/mid-rise buildings is rather limited. Although the well-known FEMA's HAZUS-MH model (FEMA 2015) and Florida Public Hurricane Loss Projection Model (FPHLP) (Vickery et al. 2006; Gurley et al. 2005) have developed hurricane risk models for high-rise buildings, they both used simplified models for debris damage, where the configuration/environment of debris sources is either considered at a single location or assumed as a homogeneous distribution. This simplification might not be appropriate for high/mid-rise buildings in urban areas, whose geometry and layouts usually vary significantly. More importantly, the uncertainties inherent in these simplifications are not determined, which may render the reliability of risk models questionable. Therefore, more research is needed to develop reliable fragility models for hurricane-induced damage to urban high/mid-rise buildings, which can consider the variations of building geometry and complex built-in environment of urban areas and can be extended to risk assessment of community levels.

Apart from the configuration of debris source, which is critical for the debris impact risk assessment of high-rise buildings, several other key components need to be considered for the prediction of windborne debris damage. These components include the debris trajectory and the wind field. The debris trajectory model can be divided into two-dimensional (2D) and three-dimensional (3D) models. The 2D models are primarily based on the research of Tachikawa (1983) and utilize simplified dimensionless equations to de-couple the basic equations of motion (e.g., Tachikawa 1988; Holmes 2004; Lin et al.2006); A 6-degree-of-freedom model is used in 3D models to describe the debris motion in 3D space. Twisdale et.al (1996) employed a random orientation 6-degree of freedom model to account for the orientation of the debris during flight. Subsequently, Richards et.al (2008) presented the deterministic 6-degree-of-freedom model, and Noda and Nagao (2010) employed experimentally determined force and moment coefficients to calculate the appropriate orientation of the debris during flight.

To evaluate the windborne debris damage to urban buildings, the local wind field over the community that drives the debris flight trajectory must be characterized. Computational fluid dynamic (CFD) (Thordal et al. 2019) and wind tunnel tests are common tools for simulating the wind field. However, the aerodynamic interaction between high-rise buildings and surroundings becomes complex in large urban areas (Elshaer et al. 2016, 2017; Dagnew and Bitsuamlak 2014), and the CFD simulation and wind tunnel test are expensive and time-consuming for large-scale and high-density building clusters. Thus, the existing tools cannot provide efficient estimates of the wind field under scenario-based risk assessments. In recent years, a growing interest in the application of machine learning (LeCun et al. 2015; Krizhevsky et al. 2012; Hinton et al.2012) has been observed with the availability of large datasets, the development of algorithms, and the computing power explosion. The machine learning approaches have shown great success in learning representation from data as a universal non-linear approximator and are receiving much attention in building data-driven models for replacing or improving CFD of high dimensionality fields with low computation cost (Calzolari and Liu 2021). There is already a lot of work that applies machine learning approaches as surrogate models for wind field simulation around buildings (Ding and Lam 2019; Zhang and You 2013; Warey et al.2020).

In the 1980s, Kutler et al. (1984) speculated about applying an Artificial Intelligence (AI) based approach in fluid mechanics and investigated the computational cost. Artificial Neural Networks (ANNs) are widely applied in heat transfer data analysis (Thibault and Grandjean 1991), flow pattern estimation (Zhang et al.1996), particle image velocimetry (Teo et al.1991) and aerodynamic design (Rai and Madavan 2001) in the 1990s. In recent years, Generative Adversarial Networks (GANs), which is one of the most promising newly developed techniques in machine learning, have attracted worldwide interest. Hu et.al. (2020) investigate the performance of four machine learning including decision tree, random forest, XGBoost, and generative adversarial networks on predicting the wind pressure coefficient, and GANs works the best with the highest R^2 values. Kim et.al. (2021) used the generative adversarial imputation network (GAIN), which is a subset of GANs, along with the multiple imputations by chained equations and the neighbored distanced imputation for predicting wind velocity field, and GAIN works the best with minimum variance and standard deviation. However, there does not exist a robust machine learning model for predicting the wind field considering the surrounding buildings. Hu et.al. (2020) and Kim et.al. (2021) only considered the interaction between two buildings. A newly proposed machine learning model of wind field can consider the interaction between three buildings via ANNs (Konka et.al, 2021). In addition, most of these machine learning models have been developed for low-rise buildings.

Scenario-based approaches are necessary for damage assessment of windborne debris due to the requirement of the time-varying wind velocity. Only studying the scenarios based on historical events or synthetic hurricanes with a certain category is insufficient for assessing community resilience. Community resilience assessment and public decision-making often require that a set of plausible scenario events be identified to capture the spatial variability in demand from a hazard event with a large footprint. In addition, the spatial nonuniformity of hurricane wind over a large community should be considered in the selection of scenarios. The U.S. Geological Survey prepares de-aggregation plots of ground motion intensities (e.g., spectral accelerations, Sa, associated with a return period (RP) of 2,475 years), which are used to develop ground motion ensembles that are used in nonlinear time history analyses that support performance-based earthquake engineering (Harmsen and Frankel 2001). An example of such a de-aggregation plot for Memphis, TN is illustrated in Fig.1.1, which shows the seismic events (magnitudes, M, epicentral distances, R, and ground motion uncertainty parameter, ε, and their relative contributions to that hazard intensity) that are dominant contributors to a spectral acceleration of 0.154 g (1.51 m/s2) at a fundamental period of 2 s from the Maximum Considered Earthquake (MCE) with RP = 2,475 years at a site in Memphis, TN. A similar de-aggregation of hurricanes that contribute to the RP wind speeds used in individual building design would provide insight into the wind field characteristics that should be considered in identifying scenario storms for resilience assessment coastal communities.

1.2 Objectives

This dissertation focuses on developing a prediction model for windborne debris damage assessment on community-level under hurricanes. The main objectives of the dissertation are:

(1) Generate hurricane scenarios with a statistical approach and identify the scenarios for community resilience assessment via a de-aggregation approach.

(2) Develop the fragility models with the hurricane intensity measures for damage assessment in the community resilience framework.

(3) Develop machine learning based prediction models using cGANs to estimate the urban wind velocity field for two-building clusters.

(4) Conduct uncertainty analysis and propagation for windborne debris damage assessment using Monte Carlo (MC) approaches.

(5) Investigate the windborne debris damage in virtual community to illustrate the procedure of windborne debris damage assessment on community level.

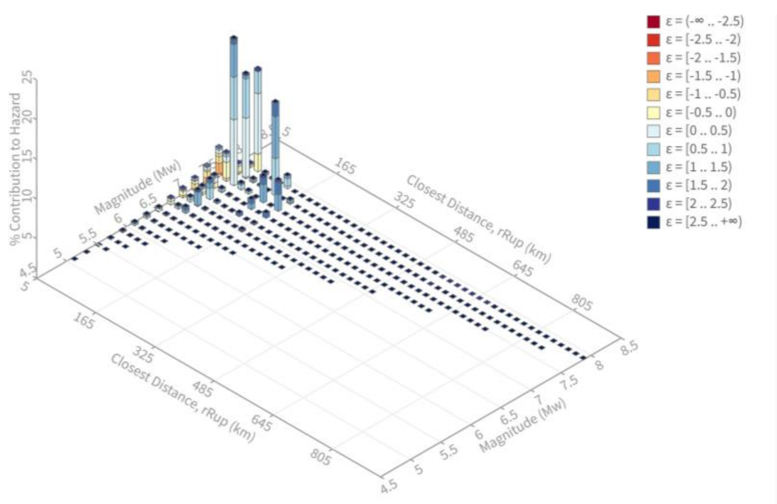

Figure 1.1 De-aggregation of Maximum Considered Earthquake at Memphis, TN (adapted from USGS 2014)

1.3 Dissertation structure

The procedure of windborne debris damage assessment is divided into three subsystems. Chapter 2 presents the subsystem responsible for simulation and selection of hurricane scenarios.

Hurricane scenarios for 200,000 years are first simulated using a statistical track and intensity prediction model. Then the de-aggregation approach is applied to select representative scenarios from the synthetic hurricane events corresponding to a stipulated return period. The performance of the proposed de-aggregation approach is investigated by conducting wind pressure damage assessments of wind pressure for city of Miami, FL. Chapter 3 presents the subsystem responsible for modeling wind borne debris damage. The debris generation, transportation and impact are investigated in this Chapter. This debris damage assessment model is validated by comparing the estimated damage with the measured damage on the envelope of one high-rise building in Kendall, Florida. The fragilities of this high-rise building on both component level and building level are constructed. Chapter 4 presents the subsystem responsible for predicting urban wind velocity field. Machine learning based wind prediction model for local urban wind velocity field is proposed using cGANs. The training data is generated through CFD simulations with Reynolds-averaged Navier–Stokes (RANS) model and efficient sampling strategy is applied to increase the prediction accuracy with limited size of training data.

The procedure of debris damage assessment includes models in both macroscale (simulation of hurricanes) and microscale (prediction of urban wind field). Besides, models with numerous parameters are involved in this procedure. Thus, Chapter 5 presents uncertainty analysis and propagation for debris damage assessment. Sensitivity analysis is also conducted to check the importance of interested factors in the uncertainty propagation.

Chapter 6 presents the debris damage assessment in designed virtual communities to illustrate the procedure of debris damage assessment on community level. The hurricane scenarios obtained in Chapter 2 and the fragilities developed in Chapter 3 with the urban wind field predicted using the data-driven model in Chapter 4 are used for debris damage assessment, and uncertainties in the predictions of damage are analyzed using the methods introduced in Chapter 5. Finally, Chapter 7 presents major findings and conclusions, recommends additional studies, and summarizes the relevance of the study for professional wind engineering practices.

CHAPTER 2 DE-AGGREGATION OF WIND SPEEDS FOR HURRICANE SCENARIOS USED IN RISK-INFORMED RESILIENCE ASSESSMENT OF COASTAL COMMUNITIES[1]

2.1 Introduction

This Chapter introduces a method for identifying a set of scenario hurricanes corresponding to a stipulated RP at a site using a de-aggregation approach. These scenario hurricanes represent the dominant contributors to community risk at this RP and provide a basis for resilience assessment of coastal communities. In contrast to previous studies that simply utilize historical records or arbitrarily chosen hurricane scenarios, the proposed approach allows a rigorous consideration of uncertainties of hurricane winds in community resilience analysis, thereby leading to improved and unbiased estimates of severe hurricane wind fields and damage at the community level as well as cost-effective risk mitigation strategies. Furthermore, the de-aggregation process establishes a direct link to the hazard levels stipulated for buildings of different Risk Categories (ASCE 2016[2]), thus relating the scenario identification to the design requirements on which the building regulatory process is based. To the best of the authors' knowledge, such a de-aggregation approach to hurricane scenario identification has yet to be attempted.

The scope of this study (Dong et.al., 2022) is limited to damage due to wind pressures on an inventory of buildings because the hurricane wind field is the starting point for a coupled hurricane wind/surge/wave assessment. Furthermore, while recovery is an essential component of community resilience assessment, the recovery phase is strongly dependent on community damage modeled as a stochastic field which, in turn, is a function of the hurricane scenarios identified.

[1] This chapter is adapted from a published paper by the author (Dong et.al., 2022).
[2] The latest version of ASCE 7 standard is ASCE 7-22. However, most of this study is done before the publication of ASCE 7-22 and the differences between these two editions have no influence on this study.

2.2 Identification of hurricane wind scenarios through a new hazard de-aggregation approach

This section introduces the methodology for de-aggregating RP wind speeds to a set of scenario hurricanes. First, synthetic hurricanes are simulated for a chosen site. Hurricanes that result in the maximum wind speed close to a stipulated RP wind speed are selected for de-aggregation. Then, a new de-aggregation approach is proposed based on parametric analysis of the hurricane wind models to identify hurricane scenarios for resilience analysis. Finally, the uncertainties associated with the modeling of scenario hurricanes are discussed. Fig.2.1 summarizes de-aggregation procedure and implementation for further damage assessment.

2.2.1 Hurricane wind simulation

The hurricane simulation models the hurricane track, intensity, and wind field. The storm tracks are created using an empirical model proposed by Vickery et al. (2000a), in which the genesis location, time, initial translation speed and heading angle of synthetic hurricanes are randomly sampled from the historical hurricanes recorded in the HURDAT2 database (Landsea et al. 2012). The changes of translation speed, $\Delta \ln s$ and heading angle, $\Delta\theta$ are modeled as the linear function of previous values:

$$\begin{aligned} \Delta \ln s &= a_1 + a_2\psi + a_3\lambda + a_4 \ln s_i + a_5\theta_i + \varepsilon_1 \\ \Delta\theta &= b_1 + b_2\psi + b_3\lambda + b_4 s_i + b_5\theta_i + b_6\theta_{i-1} + \varepsilon_2 \end{aligned} \tag{2.1}$$

where $a_1,\ldots,a_5,b_1,\ldots,b_6$ = constant coefficients; Ψ = latitude, and λ = longitude of the hurricane center location, respectively; s_i = translation speed at the time step i ; θ_i = heading angle at time step i ; and $\varepsilon_1, \varepsilon_2$ = random errors. The coefficients $a_1,\ldots,a_5,b_1,\ldots,b_6$ are determined by regression analysis using historical data on $5^{\circ}\times 5^{\circ}$ grids over the Atlantic basin. Two different sets of coefficients are estimated and used for simulating hurricane tracks heading east and west, respectively. Using Eq. (2.1), the hurricane tracks are simulated using the updated translation speed and heading angle with a 6-*h* time step and the process is terminated when the hurricane center is either out of the Atlantic basin or the travel time reaches 30 days.

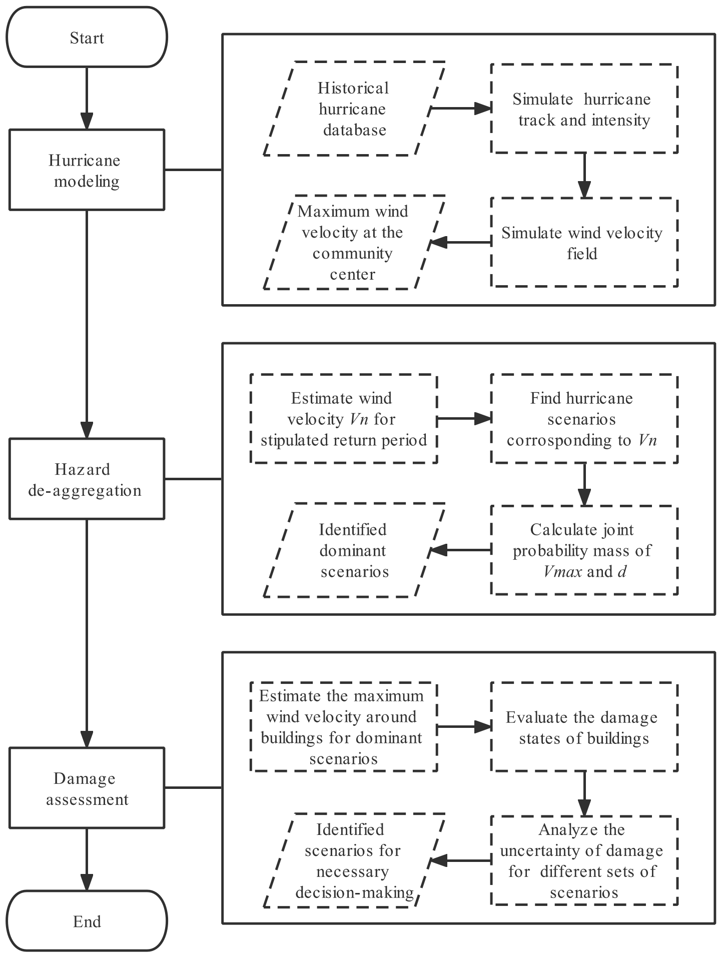

Figure 2. 1 Flow chart for the hurricane de-aggregation procedure and damage assessment

An empirical intensity model is used to update the central pressure over time. A relative intensity parameter (Darling 1991), which is determined by the central pressure and sea surface temperature (SST), is used in the intensity model instead of using the central pressure directly. The relative intensity parameter is modeled as a linear function of the previous three recent values and sea surface temperature:

$$\ln(I_{i+1}) = c_0 + c_1 \ln(I_i) + c_2 \ln(I_{i-1}) + c_3 \ln(I_{i-2}) + c_4 T_{s_{i+1}} + c_5 (T_{s_{i+1}} - T_{s_i}) + \varepsilon_3 \tag{2.2}$$

where $c_0,\ldots,c_5$ = constant coefficients; I_i = the relative intensity parameter at the time step i, T_{s_i} = the sea surface temperature at time step i and ε_3 = random error. The coefficients $c_0,\ldots,c_5$ are determined via regression analysis of historical data on 2º × 2º grids over the Atlantic basin according to the grid resolution of SST data. The SST data are obtained from the NCEP-NCAR reanalysis dataset (Kalnay et al. 1996), and the SST at the positions of the hurricane center are estimated by linear interpolation in space and time. The initial central pressure is sampled from historical data in HURDAT2 and used along with the corresponding SST to determine the initial relative intensity. The simulated relative intensities are used to update the central pressure for the corresponding hurricane center locations (Eqs. (A.1-A.5) in the Appendix). Eq. (2.2) is applicable to the intensity change of a hurricane before landfall. After the hurricane makes landfall, a hurricane filling model proposed by Vickery and Twisdale (1995) is used to model the reduction of central pressure.

Based on the simulated track and intensity (central pressure), the wind velocity field is simulated using the Holland model (Holland 1980), adjusted for the translation speed (Georgiou 1985):

$$V_G(r) = \left\{ \left(\frac{RMW}{r}\right)^B \frac{B\Delta p \exp\left[-\left(\frac{RMW}{r}\right)^B\right]}{\rho} + \frac{\left(s\sin(\beta) - fr\right)^2}{4} \right\}^{1/2} + \frac{1}{2}\left(s\sin(\beta) - fr\right) \tag{2.3}$$

where $V_G(r)$ is the gradient balance velocity at radius r, RMW is the radius of the maximum wind velocity, Δp is the deficit between the ambient pressure and the central pressure, B is Holland's pressure profile parameter, ρ is the density of air, f is the Coriolis parameter, s is the translation speed and β is the angle from the translation direction to the site (clockwise positive). The Coriolis force term fr at *RMW* is small and the maximum wind speed at *RMW* can be estimated from Eq. (2.3) as:

$$V_{G\max} \approx \sqrt{\frac{B\Delta p}{e\rho}} + \frac{s}{2} \tag{2.4}$$

Parameters *RMW* and *B* are determined by the central pressure through the empirical models (Vickery et al. 2000a):

$$\ln R_{\max} = 2.636 - 0.00005086\Delta p^2 + 0.0394899\psi + \varepsilon_4 \tag{2.5}$$

where the random error term ε_4 is assumed to follow a normal distribution with zero mean and standard deviations of 0.4164 and 0.3778 for hurricanes located south of 30°N and north of 30°N, respectively.

$$B = 1.38 + 0.00184\Delta p - 0.00309 R_{\max} \tag{2.6}$$

The sampling interval of wind field speed simulation is 20-*min* and the simulated wind speed is a 10-*min* mean wind speed at gradient height (Vickery et al 2009c; Georgiou 1985). This gradient wind speed is converted to the 10-*min* sustained wind speed at 10 *m* height for open water by multiplying by a marine surface wind reduction factor equal to 0.85 (Vickery et al. 2009b). Finally, the 10-*min* surface wind speed is converted to the 3-*sec* gust wind speed in open terrain by multiplying by a sea-land transition ratio equal to 0.86 (Vickery et al. 2000b; Simiu et al. 2007) and a gust factor equal to 1.38 (Harper et al. 2010; Simiu and Yeo 2019).

Synthetic hurricanes in the Atlantic basin for 200,000 years are simulated using the method described above. The number of hurricanes simulated each year is sampled from a negative binomial distribution (Vickery et al. 2000a). Tracks that pass through a circle centered at the milepost of interest on the coast with a 100-*km* radius are selected to determine the RP wind speed at that milepost. First, the annual non-exceedance probability is obtained by fitting the annual extreme maximum 3-*sec* gust wind speeds at the milepost induced by these selected synthetic hurricanes to a Gumbel distribution (Simiu and Yeo 2019):

$$P(U < U_R) = \exp\left\{-\exp\left[-a\left(U_R - b\right)\right]\right\} \tag{2.7}$$

where U_R = wind speed of RP of R, a=dispersion parameter, and b=mode parameter. Then U_R is calculated using (Kang et al. 2015):

$$U_R = -\frac{1}{a}\ln\left[-\ln\left(1-\frac{1}{R}\right)\right]+b \tag{2.8}$$

2.2.2 De-aggregation of return period wind speed

The simulated hurricanes that induce a maximum wind speed within 97% to 103% of the stipulated RP at the milepost considered are selected for de-aggregation. De-aggregation of hurricane winds involves more variables (identified above) than de-aggregation of earthquake ground motions, where the USGS customarily uses magnitude, *M*, epicentral distance *R* and uncertainty, ε (Figure 1). The description of hurricane wind fields requires a number of parameters including central pressure (pressure deficit), Holland parameter *B*, *RMW*, the shortest distance between the site to a hurricane track (*d*), the translation component ($s\sin(\beta)$ in Eq. (2.3)), and the heading angle (α) when the hurricane makes landfall. Furthermore, the selection of de-aggregation parameters may also depend on the context of decision making. For example, a decision-maker concerned with one specific critical facility might need to understand the risk to that facility and require a different de-aggregation than a decision-maker who oversees the resilience planning of the entire city.

In our study, the de-aggregation is performed to facilitate resilience assessment and decision-making for an entire city with an area comparable to that of a severe hurricane. Accordingly, there are two basic considerations in the de-aggregation analysis. First, although the selected hurricanes result in very similar RP wind speeds, they may present different characteristics in terms of footprint size, wind track and wind field distribution, all of which are important if one is interested in the hurricane impact over a large area. Thus, the de-aggregation should allow representations of hurricanes with the most distinct spatial characteristics. Second, the number of variables that describe distinct features of the hurricane scenarios should be small enough to facilitate easy understanding by non-experts, such as community planners. Recent studies (Mei et al, 2012; Kossin, 2018) have indicated that the translation speed of historical major hurricanes averages around 5 m/s and only half of the translation speed, which is less than 5% of their maximum wind speeds, is accounted for the final wind velocity in Eq. (2.3); thus, the translation speed is an insignificant contributor to the wind velocity field and is not considered in the de-aggregation process. Parameters *B* and *RMW* are determined by the central pressure (pressure deficit) (Eqs. (2.5-2.6)). Furthermore, the central pressure can be replaced by the maximum sustained wind speed ($V_{\max}$), which is a more common indicator of the intensity of a hurricane (and more easily understood by a lay person). $V_{\max}$ can be determined using central pressure and parameter *B* (Eq. (2.4)). Therefore, the important parameters can be reduced to three independent variables, $V_{\max}$, d and α. A preliminary de-aggregation based on these three variables shows that α approximately follows a uniform distribution in the range of all possible hurricane heading angles and has no significant influence on the de-aggregation results. Thus, only two variables, $V_{\max}$ and d are required for de-aggregation.

The significance of hurricane wind hazard de-aggregation on community resilience assessment is demonstrated using hurricane scenarios that have been de-aggregated from 700-*yr* and 1700-*yr* RP winds at Miami, selected for the following reasons: 1) De-aggregation of events with RPs in the range of 500 to 2,000 years is more informative for community resilience assessment because a number of hurricanes with different wind field characteristics can give rise to a RP wind of this magnitude, each of which may have a different impact on the community; 2) The maximum expected losses during the remainder of the 21st century are likely to occur from events with a RP of on the order of 500 to 2,000 years because the probability of occurrence of much larger events is very small. The wind speeds for the 700-*yr* and 1700- *yr* RP events at the center of Miami calculated using the above simulation from Eq. (2.8), are 74 *m/s* and 80 *m/s*, respectively. These RP wind speeds agree well with those provided in ASCE 7-16 (76 *m/s* for 700-*yr* and 80 *m/s* for 1700- *yr* RP winds). The de-aggregation showing 131 hurricanes that result in the 700-yr RP wind speed at Miami is presented in Fig. 2.2(a). The positive and negative values of d indicate that the hurricane center is on the south and north of the city center, respectively. The likelihoods of events with various combinations of $V_{\max}$ and d are presented using the probability masses (i.e. columns in Figs. 2.2) based on 2 *m/s* by 15 *km* grids. The ten highest probability masses contribute most of this RP wind with a total probability of 64.9% of all events. The scenarios from these ten highest probability masses represent the most plausible hurricane scenarios. A similar result is presented for the de-aggregated 1,700-*yr* wind speed in Fig. 2.2(b).

2.2.3 Uncertainties in scenario hurricane wind field

The proposed de-aggregation and identification of the hurricane scenarios enables a rigorous propagation of uncertainties in hurricane winds to community resilience analysis, which is not possible using a single scenario-based (or historical) hurricane analysis. Uncertainties related to hurricane winds are both aleatory and epistemic in nature. The aleatory uncertainty is related to the hazard itself and includes the uncertainties in occurrence, track (translational speed and heading angle), intensity (e.g., relative intensity, pressure deficit), and wind field (e.g., *RMW*). The

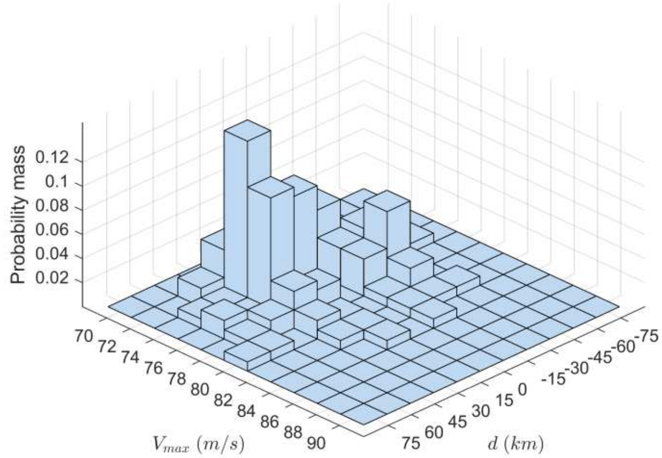

Figure 2.2(a). 700-*yr* RP wind at Miami – risk category II buildings

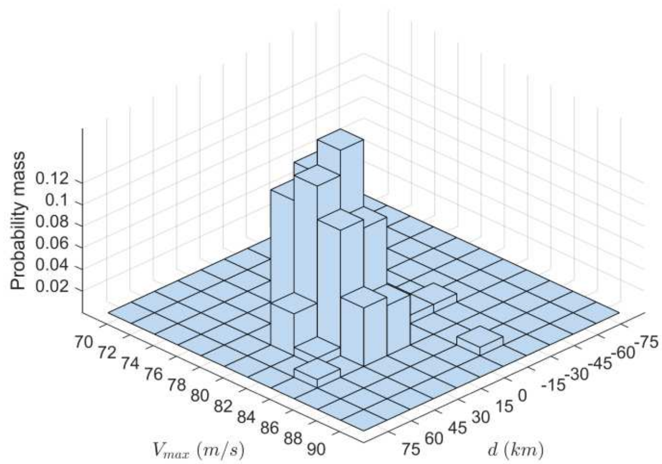

Figure 2.2(b). 1700-*yr* RP wind at Miami – risk category III buildings

Figure 2.2 De-aggregation of hurricane winds at Miami, FL for risk category II and III buildings

epistemic uncertainty mainly represents the uncertainties in the *models* of track, intensity and wind field (including uncertainties in both model form/class and parameters), as well as the uncertainties of measurement/re-analysis data. For aleatory uncertainties, the annual occurrence is modeled using a negative binomial distribution in this study. The uncertainties of the translation speed, heading angle, intensity (central pressure/pressure deficit) and *RMW* are considered using the random error terms in Eqs. (2.1), (2.2) and (2.5), which are modeled as zero-mean normal random variables with standard deviations estimated using historical data. Since only one set of models is used for track, intensity and wind field, epistemic uncertainties associated with model class/form are not considered in this study. The model parameters, such as $a_1,\cdots,a_5,b_1,\cdots,b_6$ in Eq. (2.1) and $c_0,...,c_5$ in Eq. (2.2), are obtained from the regression analysis and treated as deterministic. Therefore, the modeling uncertainties due to model parameters are not considered for the track and intensity models. The uncertainty of Holland model parameter B in Eq. (2.3) is implicitly considered by propagating the uncertainties from the pressure deficit and *RMW* (Eq. (2.5)).

Among the various sources of uncertainty, the Holland parameter B and the central pressure (pressure deficit) account for about 70% of the overall uncertainty in wind speed prediction (Vickery and Wadhera 2008; Vickery et al. 2009a). In addition, the distance between the hurricane center and the chosen site (governed by the hurricane track) as well as the *RMW* determine the spatial variation of wind field/pressure on the chosen community and may significantly impact the characteristics of damage patterns within the community. The proposed hurricane de-aggregation method has considered all these important uncertainty sources in the hurricane scenarios that have been identified, and thus supports more rational resilience planning and decision making.

2.3 Damage assessment methodology

The assessment of hurricane wind-induced damage to buildings in a coastal community has several ingredients in addition to the demands from the selected hurricane scenarios discussed in the previous section: probabilistic models of the capacity of the buildings in a community (building fragility assessment); estimation of damages to individual buildings; aggregation of building damages due to each scenario; and statistical analysis of damage profiles to determine a basis for the risk-informed decision.

2.3.1 Building fragility modeling for hurricane winds

The wind load on the main wind force-resisting system (MWFRS) or the components and cladding (C&C) elements comprising the building envelope is (ASCE 2016):

$$W = q_z\,(GC_p) - q_i\,(GC_{pi}) \tag{2.9}$$

in which q_z *and* q_i = velocity pressures applied to the exterior and interior surfaces:

$$q = 0.00256\,K_z\,K_{zt}\,K_d\,V^2 \quad (\textit{in psf; V in mph}) \tag{2.10}$$

$$q = 0.613\,K_z\,K_{zt}\,K_d\,V^2 \quad (\textit{in Pa; V in m/s}) \tag{2.11}$$

where V = the 3-*sec* gust wind speed at 10 *m* (33 *ft*) elevation, K_z = exposure factor, K_{zt} = topographic factor (assumed to be 1.0 in this study), K_d = directionality factor, and the GC_p terms are aerodynamic coefficients. The hurricane hazard wind field, intensity, track, etc., are encapsulated in the probability $P(V > v)$. However, the other terms play a non-negligible role in the uncertainty in the wind pressure acting on the structure. The velocity pressures q_z and q_i depend on whether the mean roof height of the building is less than or greater than 18 *m* (60 *ft*) and whether the MWFRS or the building envelope are considered.

Post-disaster investigations have revealed that engineered buildings seldom suffer damage to their MWFRS due to hurricanes; most damages and economic losses are related to breach of the building envelope (designated as components and cladding, or C&C in ASCE 7), followed by severe water damage to the building contents (Manning and Nicholas 1991; Sparks 1994). Assuming that the governing limit states for the building envelope involve suction or uplift on the exterior surfaces of the building combined with pressure on the interior surfaces and that the wind load and dead load effects counteract one another, the component or system fragility is:

$$Fragility = F_R(v) = P(R < W - D \mid V = v) \tag{2.12}$$

in which R = component or subsystem resistance (capacity), D = dead load, and the expressions for W are defined in Eqs. (2.9-2.11), where the stipulated ASCE 7-16 nominal wind parameters are replaced with random variables to capture all uncertainties.

A hurricane wind fragility is a reflection of the uncertainties in the non-velocity terms in Eq. (2.12), under the condition that $V = v$ (the control variable). More precisely, the fragility is defined as the conditional probability of reaching a performance limit state (e.g., $R < W - D$ in Eq. (2.12)), conditioned on hurricane wind, $V = v$, for the structure, component or system considered (Ellingwood 1990; Singhal and Kiremidjian 1996; Shinozuka et al. 2000; Rosowsky and Ellingwood 2002; Li and Ellingwood 2006; Porter et al. 2015). As a conditional probability, it is not as informative measure of risk as a fully coupled analysis involving the convolution of capacity and demand. However, the fragility enables a risk-informed evaluation of infrastructure performance when the hazard can be identified as a scenario event, and this is especially useful in community resilience assessment. Fragility modeling is the first step toward modeling damage to the built environment.

The most common method of describing the fragility of a structure or component is with a two-parameter lognormal distribution:

$$F_R(v) = \Phi\ (\ln\ [m_R\ /\ m_W(v)]\ /\ \beta_R) \tag{2.13}$$

in which m_R and β_R are respectively, the median capacity (50$^{\text{th}}$ percentile) of the component and the logarithmic standard deviation in its capacity, $m_W(v)$ = median wind pressure, given that $V = v$, and $\Phi(\ )$ = standard normal probability integral (Ellingwood 1990). All fragilities in this study, defined by Eq. (2.13), are keyed to a 3-*sec* gust wind speed measured in an open country exposure at an elevation of 10 *m* (33 *ft*).

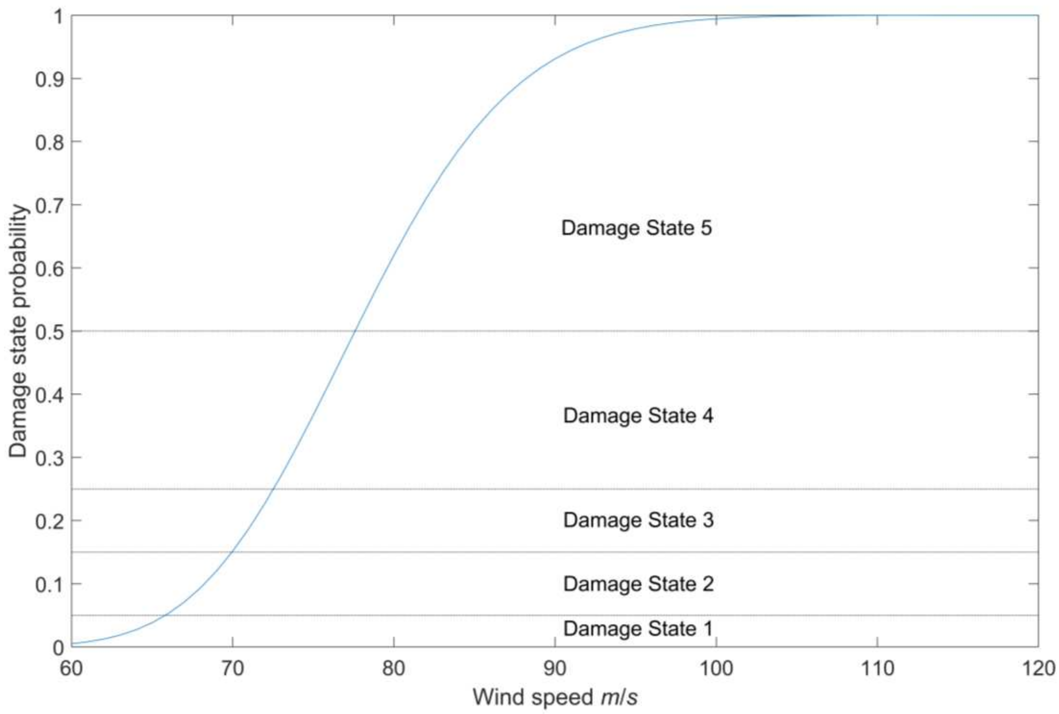

Figure 2.3 Hurricane wind fragility and damage state identification (Risk Category II (ASCE 2016))

2.3.2 Damage assessment for individual building

Each scenario hurricane identified using the simulation methods described previously is moved over the built environment of the coastal community, with wind speeds at successive 20-*min* intervals noted, to estimate damages. Since the overarching purpose of the study is to examine the impact of alternative de-aggregated hurricane wind scenarios on the estimated damage to a large urban area on a scale in the order of 10-100 *km* (a scale comparable to the scale of the wind field of a severe hurricane), we assume that the level of damage can be related to the maximum wind speed at each building site, as illustrated from the fragility illustrated in Fig. 2.3. More specifically, we assume that five damage states (described qualitatively) are possible, with ordinal ranks 1 – 5, as summarized in Table 2.1:

Table 2.1 Hurricane damage states vs building fragility

Damage state	Description	Fragility, $F_R(v)$
1	Negligible	$0 < F_R(v) \leq 0.05$
2	Minor	$0.05 < F_R(v) \leq 0.15$
3	Moderate	$0.15 < F_R(v) \leq 0.25$
4	Major	$0.25 < F_R(v) \leq 0.50$
5	Complete	$0.50 < F_R(v) \leq 1.0$

For example, if the maximum wind speed at the building site falls in the range where $0.05 < F_R(v) < 0.15$, building damage is assumed to be minor. This approach gives an estimate of the damage to each building without the need to estimate the costs of repairing the building envelope or replacing the building contents damaged by wind and water. We believe that this is adequate for the purposes of this study. Further details are provided in the illustrations that follow.

2.3.3 Aggregation of building damages across building portfolio

Consider a coastal community consists of N_B buildings. The aggregated damage to the community building portfolio can be determined as follows:

1. Identify N_S hurricane scenarios using the approach described previously;
2. Simulate the passage of hurricane scenario n =1 over the community;
3. Determine the maximum wind speeds at each building site, $k = 1, 2, \ldots, N_B$, during the passage of the hurricane;
4. Determine the damage state of each building, $k = 1, 2, \ldots, N_B$, by comparing the fragility determined via Eq. (2.13) to the discretization of damage in Table 2.1, as described in the previous subsection;
5. Repeat the above analysis for each of the remaining scenarios, $n = 2, \ldots, N_S$.

The result of this simulation is N_S sets of N_B damage states for the N_B buildings in the building inventory. There are a number of ways to post-process the data, among them:

1. Using hurricane scenario n, estimate the mean and standard deviation of aggregated damage states, μ_{Dn} and σ_{Dn}, for the N_B buildings in the community using the method of moments. Such an analysis might be performed to determine the sensitivity of community damage to scenario selection.
2. Using all N_S scenarios, estimate the mean and standard deviation, μ_{Dk} and σ_{Dk} of the damage states observed for building k in the portfolio, $1 \leq k \leq N_B$. Such an analysis might be performed to identify the vulnerability of a hospital or critical facility to risk-consistent hurricane scenarios.

2.4 Description of building infrastructure

To illustrate the de-aggregation process in hurricane damage assessment, we considered an urban community patterned after Miami, FL in Southeast Florida, extending approximately 18*km* (11.2 *mi*) along the Atlantic coastline and approximately 8 *km* (5 *mi*) inland to the Everglades, with approximately 460 thousand people and an area of approximately 93.23 km^2 (36 mi^2). This area is sufficiently large that the variation in the hurricane wind field may be expected to influence the damage sustained within the coastal community. The 3-*sec* gust wind speed for Risk Category II buildings in ASCE 7-16, comprising the majority of building construction, with a RP of 700 years (equivalent to a mean annual frequency (MAF) equal to 0.0014) over this region is 76 *m/s* (170 *mph*). We considered representative hurricane wind field scenarios de-aggregated from 700-*yr* and 1,700-*yr* RP wind speeds (Risk Category III buildings) in our hurricane damage assessment to estimate the mean and uncertainty in damage to selected buildings in Miami caused by a storm of this intensity. We also considered the damage to the same community due to Hurricane Andrew of 1992, which had approximately the same peak gust wind speed as the 700-*yr* event, to show the implications for decision-making analysis when using the proposed de-aggregation approach versus a single scenario-based analysis.

2.4.1 Building archetypes for damage assessment

To achieve the fundamental purpose of this study, which is to examine the role played by de-aggregation of extreme hurricane winds on community damage assessment, we simplify the Miami building inventory by distributing surrogate buildings classified by ASCE 7 in risk Categories II, III and IV over its urban area. These buildings are designed using the requirements specified in *ASCE Standard 7* (ASCE 2016). All buildings considered are assumed to be engineered; thus, the damage is assumed to be due to breach of the building envelope. Single-family residences are not considered. For most ordinary buildings falling in Risk Category II, the wind speed is stipulated at the 700-*yr* RP. For Risk Category III buildings (typically public assembly occupancies where large numbers of people gather) and Risk Category IV buildings (typically hospitals, fire stations and other buildings needed to function to meet the community needs in a post-disaster environment), the RPs are 1,700 and 3,000 years, respectively. The Risk Category III and IV buildings are placed at their actual locations to maintain the same scale as the footprint from a realistic scenario hurricane while the Risk Category II buildings are distributed uniformly throughout the urban area.

2.4.2 Basic assumptions in damage assessment

Exterior building envelope materials and components on engineered buildings, including windows, doors, multiple types of sidings, sheathing materials, typically are designed or rated based on an allowable stress design procedure. Such building envelope products that have been tested to pressure standards, such as ASTM E330-02 (2021), are typically rated for an allowable stress design wind pressure (W_{50}) rather than a strength design pressure ($1.0W_{700}$) (the subscript of W denotes the RP). Their *median* capacities must be scaled up to reflect the rating process.

The reliabilities of C&C elements are less than the targets in Table 1.3-1 of ASCE 7-16 for MWFRS (ASCE 2016). A previous analysis of the reliability of components and cladding on low-rise buildings (Li and Ellingwood 2006) revealed that the median probability of failure of C&C elements, conditioned on the occurrence of the design wind (either $1.6W_{50}$ or W_{700}), was on the order of 40 – 60%. This observation, coupled with the component rating procedure described above, suggests that the median roof and wall C&C elements, m_R, may be keyed to the nominal wind pressure, W_n. Furthermore, the logarithmic standard deviations define the slopes of the fragility curves, $\beta_R \approx (V_R^2 + V_W^2)^{1/2}$ in which V_R = COV in strength and V_W = COV in wind pressure, given that random variable, $V = v$. The uncertainties in the resistance of building components are considered in β_R.

The following assumptions are common to all buildings considered:

1. The building inventory considered in our study in Miami can be described by the six engineered surrogate building archetypes summarized in Table 2.2.
2. All buildings represent post-Andrew construction.
3. Buildings are assumed to be located in Exposure B. This assumption is acceptable for the purposes of this study since the exposures are distinguished solely by the parameter K_z.
4. The building envelope components considered are cladding panels located in the region of flow separation at the mean roof height, h, of the building. Since it is customary engineering practice to design the cladding for the local wind pressures, the performance of these panels is assumed to be representative of the performance of the building envelope as a whole. The dead load is negligible for such panels.

5. The median cladding resistance, m_R, typically is on the order of $1.05W_n$, in which W_n is calculated using the basic design wind speed, V_{700} using Eq. (2.9). This reflects a typical conservative bias in component strength.
6. The *median* wind load effect, $m_W(v)$, is approximately equal to $W(v)$ determined by Eqs (2.9) - (2.11); conservatism in the exposure and aerodynamic coefficients in Eq. (2.9) is neglected.
7. The logarithmic standard deviation β_R can vary from 0.17 to 0.23, as noted in previous studies (Rosowsky and Ellingwood 2002; Li and Ellingwood 2009).
8. For buildings in which the mean roof height is less than 18 *m* (60 *ft*), wind pressures on the panels are determined from Section 30.3 of ASCE 7-16 (ASCE 2016).
9. For buildings in which the mean roof height is greater than 18 *m* (60 *ft*), wind pressures on the panels are determined from Section 30.5 of ASCE 7-16 (ASCE 2016).

As an example of fragility calculation, consider the two-story public school building in Table 2.2. Public schools in hurricane-prone areas are designed as Risk Category III because they may be used for temporary shelter. The design wind speed for a Risk Category III structure in Miami (1,700-*yr* RP) is 80 *m/s* (180 *mph*). The building envelope consists of glass exterior cladding panels (A = 9.3 m^2 (100 ft^2)) on walls. Using ASCE 7-16, Section 30.3 (h < 18 *m* (60 *ft*)):

q_h = 0.613 (0.73) (0.85) $(80)^2$ = 2434 *Pa* (50.75 *psf*)

GC_p = -1.05 (Figure 30.3-1, ASCE 2016)

$GPpi$ = -0.18 (Table 26.13-1, ASCE 2016)

W_n = 2434 [-1.05 – 0.18] = -2993 *Pa* (-62.45 *psf*) (suction)

Fragility parameters: m_R = 3100 *Pa* (65 *psf*) , β_R = 0.20

Wind speed corresponding to m_R: 82 *m/s* (184 *mph*) (Fig.2.3)

Table 2.2 Fragilities for building archetypes used in damage assessment

Engineered buildings (damage to building envelope only)	Number	Risk Category	Design wind speed (*m/s*)	m_R C & C (*m/s*)	β_R
3-story commercial building (h = 15.2 *m*)	12084	II	76	2800 *Pa* (77 *m/s*)	0.20
2-story school building (h = 10.7 *m*)	199	III	80	3100 *Pa* (82 *m/s*)	0.20
Public assembly building (h = 27.4 *m*)	22	III	80	4500 *Pa* (82 *m/s*)	0.20
2-story fire station (h = 12.2 *m*)	13	IV	85	3600 *Pa* (86 *m/s*)	0.20
2-story police station (h = 15.2 *m*)	22	IV	85	3600 *Pa* (87 *m/s*)	0.22
4-story hospital (h = 22.9 *m*)	13	IV	85	5000 *Pa* (88 *m/s*)	0.18

2.5 Building damage assessment of Miami, FL

The selection of hurricane scenarios should consider both their relative likelihood and their damage potential for the community. In this section, the selection of hurricane scenarios and their role in damage assessment within Miami under these hurricane scenarios is investigated.

2.5.1 Damage estimates for one scenario

The damage to the building portfolio in a large community depends on the hurricane track and wind velocity field, the location of the buildings and their risk categories. We first illustrate the damage assessment approach with one hurricane scenario de-aggregated from the 700-*yr* wind speed, which shows the influence of the latter two factors on wind damage. In this scenario, $V_{\max}$ equals 82 *m/s* and the distance between the hurricane and community centers is 32.8 *km*. Fig. 2.4 shows the wind speed contours over Miami and the damage states of four representative public-school buildings with different locations. The wind speeds range from 66 *m/s* to 78 *m/s* and increase from north to south. The damage states range from 2 to 4, with the schools located at the southern part of Miami tending to have more serious damage. The spatial distribution of the damage states for the schools at different locations is consistent with the wind speed. Therefore, simply applying a uniform wind speed obtained at one location under one hurricane event to assess damage to the whole community will lead to an erroneous estimate of damage to buildings at other locations, especially if the community has a large area.

The damage assessment results of the six building archetypes introduced in Table 2.2 are summarized in Table 2.3 and the damage index, which is defined as the average value of the damage state for buildings with the same archetype, is used to evaluate the overall damage level of one building archetype in the community. The damage index is smaller for buildings in the higher risk categories because buildings with higher design wind speeds generally will suffer less damage under 700-*yr* de-aggregated scenarios. Furthermore, the coefficient of variation (COV) in Table 2.3 also indicates that the damage state for the same building archetype may vary with the location of the building. Therefore, simulation of the wind velocity field and wind speed at each building site is important for community level damage assessment. Although a few extreme cases may occur due to the footprint size of the community and the wind velocity field, i.e., the school located at the southwest corner of the community reaches damage state four as shown in Fig. 2.4, the overall performance of buildings under one hurricane scenario is consistent with the risk category.

2.5.2 Damage estimates for two distinct scenarios

The de-aggregated hurricane events for the same return period may have different characteristics and induce distinct building damage patterns throughout the community, as shown by a comparison of damage patterns caused by the scenario considered in the previous subsection (Scenario 1) and a second event (Scenario 2). The $V_{\max}$ is equal to 76 *m/s* and the distance between the hurricane and community centers is 33.9 *km* for Scenario 2. The hurricane track and wind velocity curve associated with the radius of the two hurricane scenarios are illustrated in Fig. 2.5. These two hurricane events represent two different wind speed distributions over the community. The distance between the hurricane center and the community is larger than the *RMW* in Scenario 1 while the corresponding distance in Scenario 2 is close to the *RMW* as shown in Fig. 2.5. Thus,

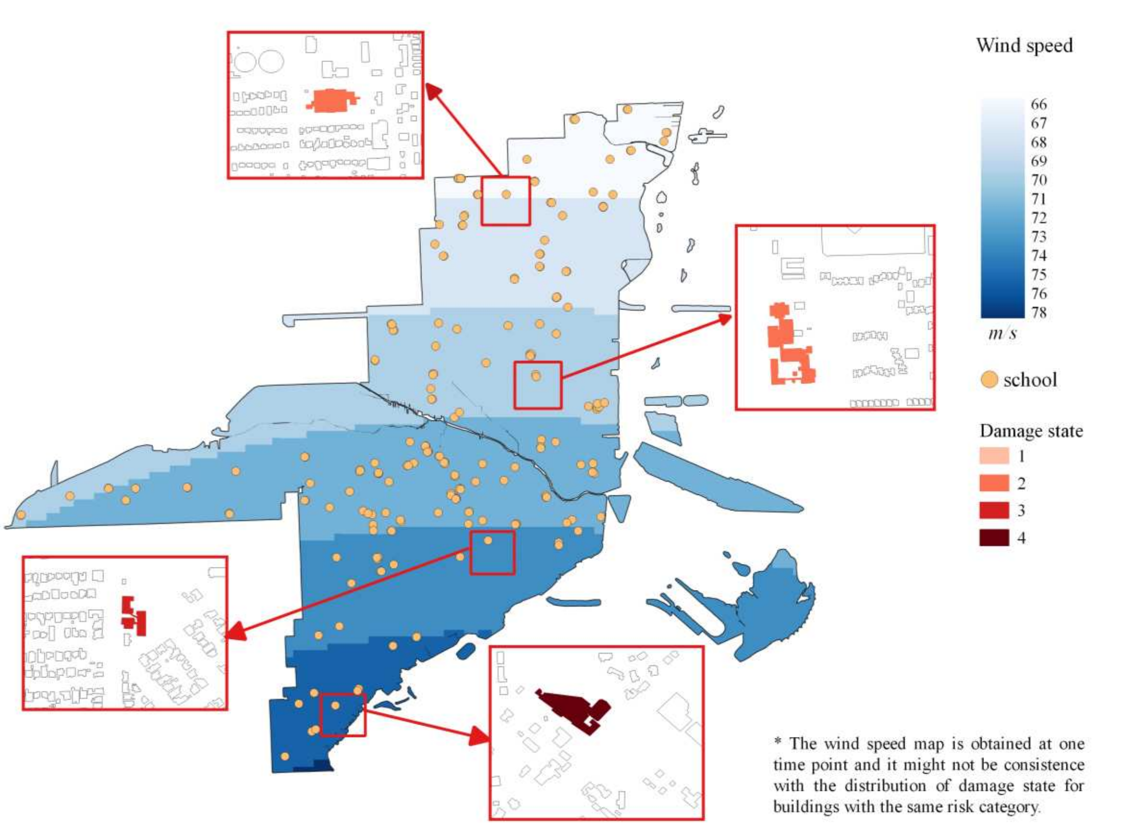

Figure 2.4 Wind contours of the community and the damage state of schools under one scenario hurricane

Table 2.3 Damage index of building inventory under one scenario hurricane

Building type	Number	Risk Category	Damage index	COV
Commercial building	12084	II	3.56	0.22
Public school building	199	III	2.66	0.33
Public assembly building	22	III	3.08	0.25
Fire station	22	IV	1.62	0.54
Police station	13	IV	1.05	0.20
Hospital	13	IV	1.15	0.33

the entire community is located in the region with a negative slope in the wind speed curve for Scenario 1 while the entire community is located in the region close to $V_{\max}$ for Scenario 2. As a result, the wind speed for Scenario 1 within the community varies over a large range and decreases with the increase of distance between the hurricane center and the wind profile location, as discussed in the previous subsection, while the wind speed for Scenario 2 varies over a small range and increases when the distance is close to the *RMW*.

The damage states of the four schools considered in Scenario1 and the wind speed contours for Scenario 2 are shown in Fig. 2.6. The wind speed for Scenario 2 ranges from 68.8 *m/s* to 73.6 *m/s* and increases from the north and south to the middle of the community. The damage states of schools under scenario 2 follow the wind speed distribution and most are in damage state two. The overall performance of the same building archetype for these two scenarios is different and the smaller COV values in scenario 2, as shown in Table 2.4, indicate that the damage states of the buildings with the same archetype is more similar compared to scenario 1. Therefore, selecting one hurricane scenario (or one real hurricane event) to represent all hurricanes associated with a stipulated return period is not sufficient to represent likely damage patterns within the community. Hurricanes with the characteristic of Scenario 1 always have large intensity ($V_{\max}$) and may induce extreme damage for some buildings. For example, some schools reach damage state four in Scenario 1 even though this scenario is de-aggregated from a 700-*yr* RP event. Thus, this type of hurricane is more dangerous to the community compared to the hurricane with the characteristic of Scenario 2.

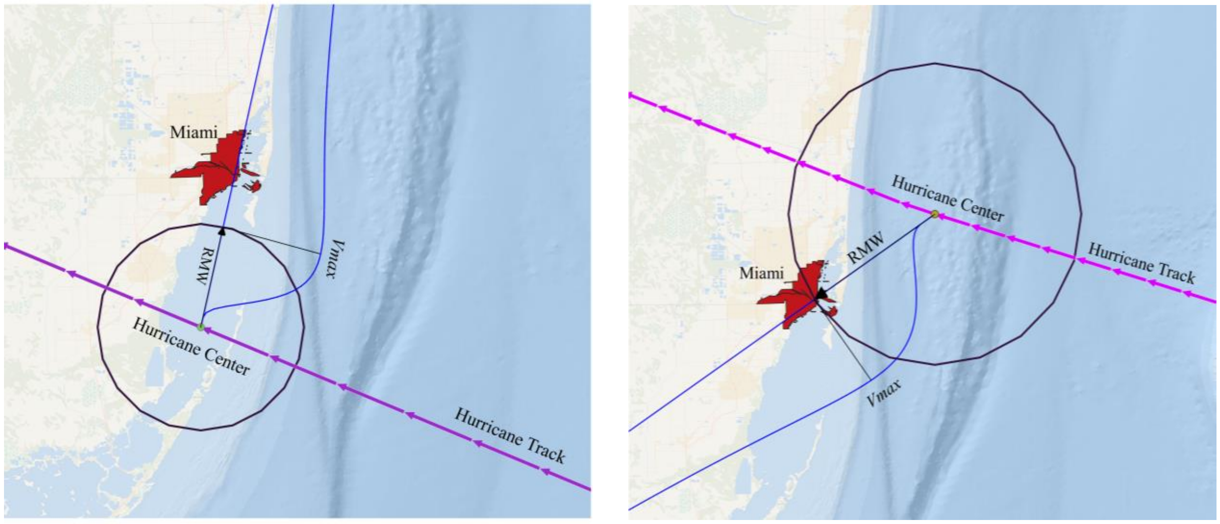

(a) (b)

Figure 2.5 Relative locations of hurricane track and community under two scenarios: (a) Scenario 1, (b) Scenario 2

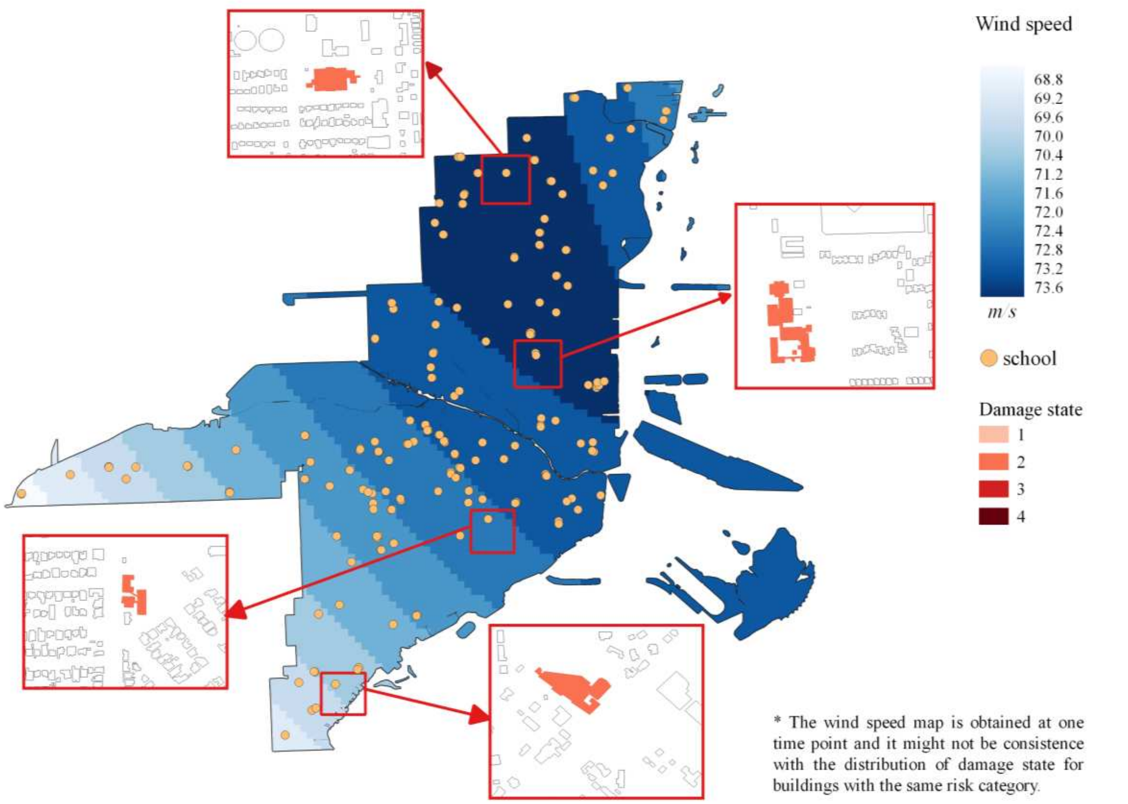

Figure 2.6 Wind contours of the community and the damage state of schools under scenario 2

Table 2.4 Damage index of building inventory under scenario 2

Building type	Number	Risk Category	Damage index	COV
Commercial building	12084	II	3.70	0.12
Public school building	199	III	2.11	0.15
Public assembly building	22	III	2.15	0.17
Fire station	22	IV	1.62	0.31
Police station	13	IV	1.00	0.00
Hospital	13	IV	1.00	0.00

2.5.3 Damage estimates for multiple scenarios de-aggregated from RP events

The previous discussion indicated that the hurricane scenarios de-aggregated from the same RP event can induce distinct damage patterns over the community due to the location of the buildings and the hurricane characteristics. Thus, the scenarios selected should cover most of the dominant contributors to the 700-*yr* or 1,700-*yr* RP event of interest, for reasons noted. However, the number of scenarios should be manageable for community damage assessment. We investigated four sets of scenarios, two for each return period. The scenarios in the highest probability mass in the de-aggregation for 700-*yr* RP (Fig. 2.2(a)) are selected as the first set of scenarios and all scenarios in the highest 10 probability masses are selected as the second set of scenarios. The third and fourth sets of scenarios corresponding to 1700-*yr* RP are obtained similarly. Scenarios in the highest probability mass represent the dominant contributors to the 700-*yr* or 1700-*yr* event. Scenarios represented by the highest 10 probability masses include about 60% of all the hurricane scenarios associated with the stipulated RP and would cover a broader spectrum of distinct damage patterns.

Tables 2.5 and 2.6 show the damage index for the six building archetypes under the first set of scenarios and the third set of scenarios. Scenarios in the first or second set of scenarios have similarities in the hurricane feature, but the damage index still slightly varies. To better compare the two sets of scenarios for the same return period, three individual buildings, which are shown in Fig. 2.7, for each building archetype are selected and the individual damage states of these buildings under the two set of scenarios are compared. The comparison results are shown in Tables 2.7 and 2.8. The mean value and COV of damage state for individual buildings under the two sets of scenarios for the 700-*yr* RP are similar and the damage assessment result for the 1700-*yr* RP has the same behavior. Therefore, the decision-maker need only consider the hurricane scenario under the dominant probability mass for a stipulated return period for the following reasons: 1). the number of hurricane events in the top probability mass is 18, which is manageable for community damage assessment; 2). the hurricane events in the top probability mass can have different damage patterns and the similarity in the COV value of the two sets of scenarios shows that considering the top 10 probability masses does not significantly increase the variance in the damage pattern: 3). the hurricane events in the top probability mass are the dominant contributors to the return period event considered.

We also considered the damage caused by Hurricane Andrew, which is presented for comparison in the last column of Table 2.7. The wind velocity field of Hurricane Andrew is calculated based on the H*wind data (Powell et al. 1998, 2010) and the maximum 3-*sec* surface wind speed at the center of Miami is about 72 *m/s*, which is slightly lower than the wind speed for 700-*yr* RP. The differences between the scenario averages presented in Columns (2) and (4) of Table 2.7 and the damages caused by Hurricane Andrew reveal that consideration of only one scenario hurricane, regardless of how severe, may lead to the underestimation of the damage to a community.

Table 2.5 Damage index of building inventory under multiple scenarios (700-*yr* RP)

Scenario	Risk Category					
	II	III		IV		
	Commercial building	Public school building	Public assembly building	Fire station	Police station	Hospital
#1	4.00	3.00	3.00	2.00	2.00	1.00
#2	4.00	2.15	3.00	2.00	2.00	1.00
#3	3.76	2.00	2.00	1.46	1.91	1.00
#4	3.00	2.00	2.00	1.00	1.00	1.00
#5	3.98	2.00	2.00	1.77	2.00	1.00
#6	3.00	2.00	2.00	1.00	1.00	1.00
#7	4.00	2.00	2.85	1.92	2.00	1.00
#8	3.52	2.00	2.00	1.00	1.77	1.00
#9	3.81	2.00	2.00	1.69	1.95	1.00
#10	4.00	2.29	2.77	1.69	2.00	1.00
#11	3.47	2.00	2.00	1.15	1.73	1.00
#12	2.69	1.83	2.00	1.08	1.00	1.00
#13	3.80	2.12	2.85	1.62	1.82	1.00
#14	4.00	2.86	3.00	2.00	2.00	1.00
#15	3.89	2.00	2.00	1.46	2.00	1.00
#16	3.00	2.00	2.00	1.00	1.00	1.00
#17	3.87	2.02	2.69	1.77	1.91	1.00
#18	3.88	2.26	2.85	1.92	1.95	1.00

Table 2.6 Damage index of building inventory under several scenarios (1700-*yr* RP)

Scenario	Risk Category					
	II	III		IV		
	Commercial building	Public school building	Public assembly building	Fire station	Police station	Hospital
#1	4.64	4.00	4.00	2.77	2.73	2.00
#2	4.14	3.96	4.00	2.38	2.50	2.00
#3	4.72	4.00	4.00	2.77	2.73	2.00
#4	4.46	3.57	3.85	2.23	2.59	1.92
#5	4.60	3.96	4.00	2.77	2.73	2.00
#6	3.92	3.26	3.77	1.92	2.05	1.15
#7	4.82	3.92	4.00	2.77	2.82	2.00
#8	4.77	3.77	4.00	2.85	2.77	2.77
#9	4.94	4.00	4.00	2.85	2.95	2.69
#10	4.41	3.53	3.85	2.15	2.55	1.85
#11	4.86	3.98	4.00	2.77	2.73	2.08
#12	4.37	3.46	3.92	2.23	2.55	1.85
#13	4.58	3.68	4.00	2.46	2.82	1.92
#14	4.85	3.93	4.00	2.92	3.00	2.85
#15	4.88	3.95	4.00	2.77	2.86	2.08
#16	4.32	3.38	3.92	2.54	2.64	1.92
#17	3.77	3.02	3.54	1.92	2.05	1.15
#18	4.74	3.94	4.00	2.69	2.64	2.00
#19	4.95	4.00	4.00	2.85	2.95	2.77
#20	4.93	3.97	4.00	2.85	2.91	2.00
#21	4.96	4.00	4.00	2.92	2.95	2.00
#22	4.83	4.00	4.00	2.69	2.91	2.00

Table 2.7 Damage assessment of building inventory under multiple scenarios (700-*yr* RP)

Individual buildings	18 scenarios		85 scenarios		Andrew
	Mean	COV	Mean	COV	Damage state
Commercial building # 1	3.72	0.12	3.64	0.14	2
Commercial building # 2	3.61	0.17	3.52	0.23	1
Commercial building # 3	3.61	0.17	3.52	0.23	1
Public school building # 1	2.06	0.20	2.20	0.25	2
Public school building # 2	2.11	0.15	2.33	0.29	1
Public school building # 3	2.17	0.18	2.34	0.22	2
Public assembly building # 1	2.33	0.21	2.44	0.24	4
Public assembly building # 2	2.44	0.21	2.58	0.22	2
Public assembly building # 3	2.44	0.21	2.59	0.22	1
Fire station # 1	1.61	0.31	1.61	0.30	1
Fire station # 2	1.72	0.27	1.68	0.28	1
Fire station # 3	1.56	0.33	1.64	0.30	1
Police station # 1	1.78	0.24	1.71	0.27	1
Police station # 2	1.78	0.24	1.72	0.26	1
Police station # 3	1.78	0.24	1.69	0.27	1
Hospital # 1	1.00	0.00	1.05	0.20	1
Hospital # 2	1.00	0.00	1.05	0.20	2
Hospital # 3	1.00	0.00	1.05	0.20	1

Table 2.8 Damage assessment of building inventory under multiple scenarios (1700-*yr* RP)

Individual buildings	22 scenarios		123 scenarios	
	Mean	COV	Mean	COV
Commercial building # 1	4.77	0.09	4.71	0.10
Commercial building # 2	4.32	0.19	4.43	0.14
Commercial building # 3	4.36	0.19	4.43	0.14
Public school building # 1	3.95	0.05	3.81	0.12
Public school building # 2	3.32	0.30	3.54	0.25
Public school building # 3	4.00	0.00	4.00	0.03
Public assembly building # 1	4.00	0.00	4.02	0.07
Public assembly building # 2	4.00	0.00	4.08	0.07
Public assembly building # 3	3.95	0.05	4.08	0.07
Fire station # 1	1.86	0.42	2.26	0.40
Fire station # 2	2.86	0.16	3.01	0.18
Fire station # 3	2.73	0.17	2.80	0.24
Police station # 1	2.95	0.13	2.97	0.19
Police station # 2	2.82	0.14	2.91	0.20
Police station # 3	2.73	0.17	2.78	0.24
Hospital # 1	2.09	0.25	2.19	0.22
Hospital # 2	2.14	0.16	2.23	0.20
Hospital # 3	2.09	0.25	2.19	0.24

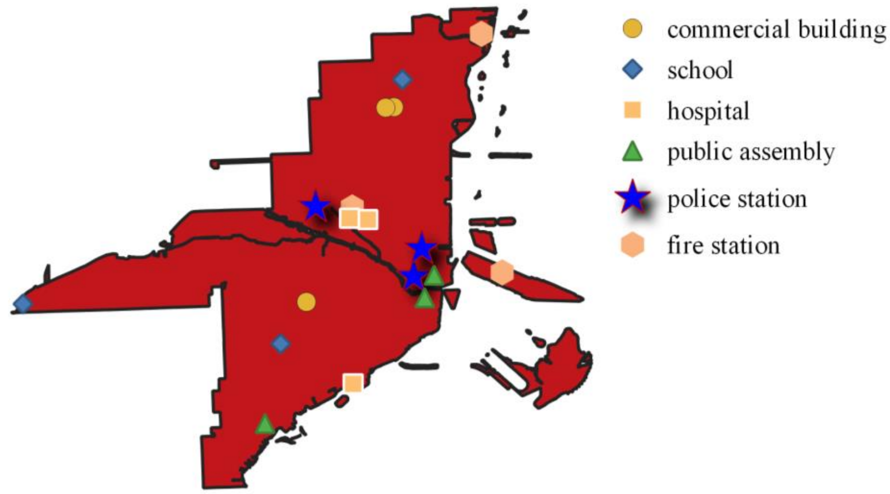

Figure 2.7 Locations of selected buildings

2.5.4 Implications for risk-informed decision analysis

The proposed de-aggregation process allows for the identification of scenarios that represent dominant contributors to specific return period hurricane events, thus establishing a direct connection to the building regulatory process. These scenarios represent the most plausible hurricane scenarios for the community, allowing for the consideration of specific wind speeds that could arise from different hurricane tracks. This process also can permit a decision-maker to select a specific wind speed that will cause maximum tolerable damage to a critical facility and calculate the functionality of the facility as impacted by the spatial distribution of damage in other infrastructure across the community. For example, if the functionality of a hospital is of concern, then a maximum level of damage to the hospital can be specified. Based on this maximum damage level, the wind speed and the associated RP can be calculated and the scenarios that contribute the most to this RP can be selected. These different hurricane scenarios will give rise to different levels of damage across the community to other infrastructure on which the hospital depends. Because the operation of the hospital relies heavily on the operation of other infrastructure such as water, transportation, power (Hassan and Mahmoud 2019, 2020), the decision-maker can then institute mitigation strategies so that damage to interdependent infrastructure does not exceed a threshold value to ensure a minimum level of operation for the hospital.

2.6 Conclusions

The building regulatory design process in hurricane-prone regions is based on design for a wind speed at a specific return period (RP) event, which depends on the Risk Category of the building or other structure. The wind speed is determined at a point and is not useful for community resilience assessment because it does not capture the spatial characteristics of the hurricane wind field and their uncertainties properly. In alternative scenario-based resilience analyses, hurricane scenarios are based either on historical events or on synthetic hurricanes in a specified Saffir-Simpson category to answer the common question: “What would happen if Hurricane X struck our community?” While this approach may personalize the threat for community planners by relating the resilience analysis to a well-known event, the uncertainties inherent in future hurricanes are not taken into account. This Chapter has presented a novel approach that establishes, for the first time, a relation between hurricane scenario selection for community resilience assessment and the building regulatory process, which is based on wind speeds associated with specific RPs. The notion of de-aggregating demand at a specific RP, which is common in the earthquake engineering community in performance-based design, also is applicable to assessing the impact of hurricanes and other natural hazards with large geographic footprints on communities. These hurricane scenarios represent the dominant contributors to community risk at this RP and provide a basis for resilience and risk assessment of coastal communities.

In contrast to existing scenario approaches, the de-aggregation process herein permits a rigorous consideration of uncertainties of hurricane winds in community resilience analysis, thereby leading to improved and unbiased estimates of severe hurricane wind fields and damage at the community level and represents an advance for estimating statistics of damage and loss realistically for community decision-making. Furthermore, since hurricane winds are the drivers of other coastal hazards such as storm surge, waves and coastal flooding, the hurricane scenarios identified by the proposed approach provide a basis for simulating multiple coupled hazards with distinct characteristics while accounting for the uncertainties in these coupled hazards.

As a first step, the current study focuses on the impact of hurricane winds on a representative building inventory in a coastal city in Florida. Significant differences are found in the damages predicted from this de-aggregated hurricane scenario approach from the damages predicted by applying the wind speeds from one extreme historical event, such as Hurricane Andrew, or those stipulated in building codes and standards based on ASCE 7-16, to a community. In particular, the results show that there is a distinct possibility that the damage estimated from a single scenario or a historical hurricane will underestimate the damage sustained by the community by a significant margin. This is due to an underestimation of uncertainties associated with the hurricane track, hurricane wind field modeled as a stochastic field, and positive correlation in wind demand over the hurricane footprint. Additional research is needed in the future to investigate the effectiveness of the de-aggregation procedure for multi-coastal hazards.

CHAPTER 3 FRAGILITY MODELING OF URBAN BUILDING ENVELOPES SUBJECTED TO WINDBORNE DEBRIS HAZARD[3]

3.1 Introduction

The existing fragilities for debris impact focus on the residential building and the intensity measure is selected according to the types of building envelope. Three fragility models of debris impact for residential buildings with different types of envelopes are listed in Table 3.1. To the best of the author's knowledge, there is no existing fragility model of debris impact on high/mid-rise buildings. Low-rise and residential buildings are usually homogeneously distributed while urban high/mid-rise often have various shapes, heights and layouts, and can modify the surrounding urban wind field. However, the geometric information of urban high/mid-rise buildings in current hurricane risk models (Vickery et al. 2006; Gurley et al. 2005; FEMA 2015) for high/mid-rise buildings is either neglected or simplified as homogeneous configurations which may introduce errors and uncertainties in windborne debris induced damage on urban buildings with varying geometries and layouts. Therefore, reliable fragility analysis of windborne debris damage on high/mid-rise building envelopes considering the variations of building geometry and complex built-in environment of urban areas is necessary.

Table 3.1 Fragility models for debris impact on residential buildings

Author	Intensity measure (Input parameter)	Type of building envelope
Chen et al (2015)	Impact velocity (*m*/*s*)	Corrugated panel
Alphonso and Barbato (2014)	Impact kinetic energy ($kg/(m/s)^2$)	Aluminum storm panel
Stone and Pang (2019)	Impact kinetic energy ($kg/(m/s)^2$)	Cross-Laminated timber panel

[3] This chapter is adapted from a published paper by the author (Dong et.al., 2023).

In light of this need, this Chapter focuses on the development of fragilities for hurricane-induced windborne debris damage to urban building envelopes. The geometry and distribution of debris sources in an arbitrary urban area are explicitly accounted for through modeling the urban wind field and environment of the debris sources collectively. A physics-based windborne debris impact model for compact debris involving debris generation and transport is developed. The three-dimensional fragilities as functions of the maximum wind speed, direction and duration of a hurricane are formulated for both component and building levels. Reduced-order and surrogate modeling are employed to facilitate fragility development. The implementation of the proposed fragility modeling approach is demonstrated through an illustrative example.

3.2 Modeling of urban wind fields under hurricanes

The hurricane wind field around urban buildings that drives the flight of the debris is complex due to the flow separation, formation of local vortices, interference of the adjacent buildings, etc. A full description of an urban wind field typically requires the use of either experimental (e.g., wind tunnel testing) or computational (computational fluid dynamics) tools. Both these tools are very costly and time-demanding, thus posing challenges for fragility analysis that requires a large data set. Therefore, this study proposes an efficient parametric urban wind field model, which decomposes the wind field around the debris source building into the main flow region (velocity is the approaching hurricane wind speed), and local flow regions on the rooftop and wake region. This simplified urban wind field model is applicable for debris impact analysis when upstream or neighboring buildings are far away enough and do not present significant aerodynamic interference effects on the debris source building. The modeling of three flow regions is essential in predicting debris-induced damage. This is because the main flow (i.e., the global hurricane wind field) to a large extent, determines the direction of possible debris flight and consequently the victim buildings downstream. The local flow regions on the rooftop drive the initiation of the flight of the rooftop debris elements. The wake region flow modifies the debris flight trajectory and influences the final debris impact location and momentum. The modeling of wind flow in each region is introduced below.

3.2.1 Simulation of main flow (hurricane wind)

The simulation of the main flow is achieved by simulating hurricane winds. The damage patterns of urban building envelopes due to windborne debris are strongly dependent on hurricane wind speed, direction, and duration. Therefore, it is important to model the change of hurricane wind speed and direction as time-dependent processes. The time-dependent hurricane wind can be decomposed into the time-varying mean and a zero-mean fluctuating component.

The time-varying mean wind velocity is simulated using an asymmetric data-driven hurricane wind field model developed by Guo and van de Lindt (2019). Using the re-analysis surface wind data from H*Wind (Powell et al. 1998, 2010) for a user-specified hurricane event, as well as its track, this data-driven model simulates a two-dimensional (2D) surface hurricane wind field (10 *m* height) along the track at any time instant for open terrain exposure. By extracting the wind speed at an urban site of interest for all time points and converting the wind speed to hourly mean for the site-specific exposure, the time history of mean wind velocity at the site is obtained. The simulated surface mean wind velocity is converted to building height by using the boundary layer wind profile for the corresponding terrain exposure (Simiu and Yeo 2019).

The fluctuating component of windstorms, depending on their nature, may be simulated under either stationary or non-stationary frameworks. For tropical cyclones (hurricanes and typhoons), the non-stationary/transient characteristics in turbulent (fluctuating) components are normally not obvious. Thus, it is assumed that fluctuating wind speed is a stationary random process in this study. Accordingly, the Fast Fourier Transform (FFT) is applied to simulate time history according to the user-specified turbulence spectrum (e.g., Kaimal Spectrum, von Karman Spectrum) (Rose and Apt 2012).

3.2.2 Modeling of local wind field in rooftop region

The local wind field is complicated by the separated turbulent flow, which usually forms intense vortices with high wind velocity and local suction underneath the vortices (Fig. 3.1a). The characteristics of these vortices have been studied extensively through wind tunnel studies, CFD simulations and full-scale testing (He and Song 1997; Meroney et.al 1999). Based on these numerical simulations and experimental measurements, a parametric vortex model on the rooftop has been developed by Banks and Meroney (2001). This study will employ Banks and Meroney model to estimate the local wind field on the rooftop. The Banks and Meroney model was validated for low-rise buildings through wind tunnel tests. It is speculated that for high/mid-rise buildings, where the observed flow pattern on the rooftop is similar to the flow pattern of low-rise buildings (Hemida et al. 2015), this model should still be viable. However, the characteristic length for nondimensionalization needs to be selected differently. While the characteristic length is often selected as the building height (Lin et al., 1995; Tryggeson and Lyberg, 2010; Banks and Meroney, 2001) for low-rise buildings, the characteristic length is selected as building width while for high/mid-rise buildings concerned in this study (Tyggeson and Lyberg, 2010; Kind and Wardlaw 1977).

The Banks and Meroney model describes the location (ϕ_c), size (radius h) and vertical velocity profile of conical vortices (Fig. 3.1). The location and size of the vortices are a function of wind approaching angle ω and are estimated by fitting the experimental data (Fig. B.1). The vertical velocity profile (Fig. 3.1c) is a function of the approaching wind velocity (i.e., reference wind velocity U_{ref}) at the rooftop height and diameter of the vortices. Specifically, first, the data-driven hurricane wind field model described in the previous section and a log-law vertical wind profile are applied to obtain the time history of the approaching mean wind speed at the roof height (i.e. U_{ref} in Fig.3.1a). Second, the accelerated wind velocity above the flow separation zone (normally three times the mean core height of conical vortices) at point M (U_M) is determined by multiplying the U_{ref} by a "speed-up ratio", which is estimated from experimental data (Fig. B.2). Then using U_M and *h* as the parameters, the vertical velocity profile associated with different flow regions within the conical vortex is estimated by the expressions given in Table B.1.

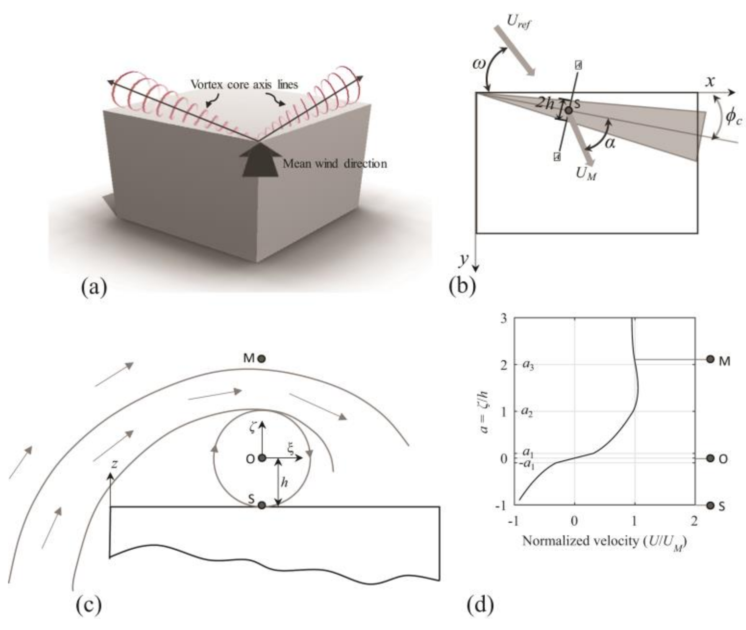

Figure 3.1 Illustration of parametric vortex model on the rooftop: (a) Three-dimension view of conical vortices, (b) Plan view of conical vortices on the roof, (c) Front view of conical vortices on the roof (section A-A), (d) Velocity profile above the conical vortices (adapted from Banks and Meroney, 2001)

3.2.3 Modeling of wake region flow and turbulence

Once debris flies behind the building, the wind velocity decreases significantly due to the wake effect, which is expected to alter the debris flight trajectory. Therefore, modeling the wind field in the wake region is important. Furthermore, the turbulence effect is another important factor to consider, as it leads to significant uncertainties in the debris flight trajectories and impact locations (Moghim and Caracoglia 2015), which in turn may cause variations in damage patterns to the building envelope. The existing studies on simulating debris flight trajectories with inherent uncertainties caused by turbulence did not consider the wake effect of a building, but rather considers the atmospheric boundary layer (ABL) flow. This study aims to consider both wake and turbulence effects simultaneously. The most straightforward way of modeling turbulent wind fields behind a building is to use wind tunnel testing or CFD simulation. However, these approaches are too expensive to be used for fragility analysis. Therefore, a simplified wind model is proposed in this study to model turbulence and the wake effect. Since the initial wind velocity of debris flight is most critical, the turbulence is only considered at the beginning of debris flight and is simulated using the Eulerian spectra for ABL, specifically turbulence spectra proposed by Solari and Tubino (2002). Note that the debris is moving, and the relative wind speed is changing; strictly speaking, the turbulence seen by the debris is neither Eulerian nor Lagrangian. However, using an Eulerian spectrum is appropriate here because the velocity of debris is low at the beginning. To justify the efficacy of using this simplified approach to model the turbulence effect, a comparative study was conducted. In this study, the statistics of the trajectories of debris flight within uniform flow using two approaches for turbulence were compared. The first approach (Method 1) is the one typically adopted in the literature (Holmes 2004). The turbulent velocity at a fixed point is simulated according to Eulerian spectra and the time history is used to drive the debris flight under the assumption that the horizontal speed of debris is typically no more than one-half of the mean wind speed and the effect of turbulence on mean trajectories is quite small. The second approach (Method 2) is the one used in this study, where only the turbulence in initial wind speed is considered rather than using a time history of turbulent wind during the flight. Both approaches simulated the trajectories of compact debris of diameter 8mm and density of 2000 *kg*/*m*^3 starting the flight at the height of 75 *m* with a mean wind speed of 26.6 *m*/*s*. The mean and standard deviation of displacement and velocity of debris from the two approaches showed good agreement (Table B.2), indicating that the proposed simplified method can effectively consider the turbulence effect. After the debris falls into the wake region, the wind velocity is updated for each time step according to the location of the object using a velocity deduction ratio. The velocity deduction ratio is a function of space and obtained from wind tunnel testing results on the wake effects of tall buildings (Meng and Hibi 1998; Taichi et.al 2003; Yoshie et.al 2007).

3.3 Modeling of debris impact mechanism

This section introduces the modeling of the physical process for debris impact, which is comprised of debris generation, flight (transport), and impact. The methodologies for modeling of this physical process are dependent on the debris types. In this study, compact debris, specifically rooftop gravel, is considered. While the proposed debris generation model is specific for gravel, the proposed modeling techniques for flight (transport) and impact can be adapted to model other types of compact debris, such as small glass pieces, by using a different debris generation model (e.g., wind pressure induced glass broken).

3.3.1 Debris generation

The mechanism of gravel scouring and flying has been investigated both theoretically and experimentally. For boundary layer winds, the critical velocity for gravel scouring can be estimated by Shields' diagram (with the consideration of Reynolds number dependency) or Bagnold's equation (without the consideration of Reynolds number dependency) (Hager 2018; Karimpour and Kaye 2012). However, these critical velocities developed for boundary layer wind might not be appropriate for this application considering the distinct features of rooftop vortices. Therefore, this study adopted the critical velocity obtained from the large-scale (1:10) wind tunnel tests on rooftop gravel scouring by Kind and Wardlaw (1984). Note that the critical wind velocity for small-scale wind tunnel tests is sensitive to the Reynolds number effects, while the Reynolds number effects are assumed to be negligible in Kind and Wardlaw's study considering that Reynolds number correction factors for 1:10 scale models are of the order 1.02 (Kind 1986; Karimpour and Kaye 2012). Kind reported the velocity speed for 19 *mm* gravel and found that the critical speed was proportional to the square root of the diameter of gravel. This finding is consistent with Shields' diagram and Bagnold's equation at ranges where the Reynolds number has a similar magnitude, which is the case for gravel size ranges in practice. Kind and Wardlaw only determined the critical velocity at the worst wind direction, i.e., 45º and the critical velocity at other wind directions is higher than that for the 45º angle (Kind and Wardlaw 1977). Therefore, the critical velocity used in this study is considered to be conservative and can be updated when more data become available. The critical velocity in Kind and Wardlaw's study was determined using low-rise building models, however, it is felt to be applicable to high/mid-rise buildings considering the similarity of roof-top flow patterns between high/mid-rise and low-rise buildings (Hemida et al. 2015). The debris flight is initiated if the approaching wind speed at the rooftop height is greater than the critical velocity.

The initial location and frequency of debris generation have a significant influence on the final impact locations on the target building. The typical gravel scour patterns on rooftops suggest that the initial locations of debris are the most likely under the conical vortices (Kind and Wardlaw

1984). Accordingly, three sampling locations indicated in Fig. 3.2 under each vortex core axis line are selected as debris generation locations to represent all the possible initial locations. The debris generation rate determines the number of debris impacting the target building, and thus the damage extent. In this study, the debris generation process is modeled as a Poisson process with a rate λ, which represents the mean number of debris generated during a certain period. The debris generation rate λ is dependent on the wind velocity on a rooftop (λ is larger for a larger approaching wind velocity).

Note that the Poisson model for debris generation is independent of the critical velocity. The debris generated with approaching wind velocity lower than the critical velocity is abandoned in further analysis.

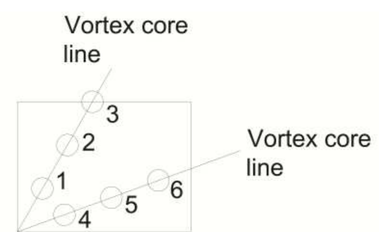

Figure 3.2 Possible gravel initial locations on the rooftop

The debris size also can affect the trajectory and the impact momentum. Compared with small debris, large debris cannot be easily accelerated in the wind field but can provide large momentum with a large mass. Typically, debris that is too small may not induce enough impact momentum when hitting windows and debris that is too large may hit the ground before hitting windows. Thus, only debris within a specific size range will hit and damage windows. The size of gravel on rooftops is assumed to follow a normal distribution and the corresponding parameters can be determined by measurement (ASTM 2000). According to the previous discussion, only debris samples with sizes in a certain range will be utilized for further trajectory and damage simulation.

3.3.2 Modeling of debris flight trajectory and impact

The trajectory of compact debris flight can be simulated using the fully coupled three-dimensional motion equations proposed by Richards et al (2008).

$$\begin{aligned}
\frac{d^2x}{dt^2} &= k\left(U_x - u_x\right)\cdot\sqrt{\left(U_x - u_x\right)^2 + \left(U_y - u_y\right)^2 + \left(U_z - u_z\right)^2} \\
\frac{d^2y}{dt^2} &= k\left(U_y - u_y\right)\cdot\sqrt{\left(U_x - u_x\right)^2 + \left(U_y - u_y\right)^2 + \left(U_z - u_z\right)^2} \\
\frac{d^2z}{dt^2} &= k\left(U_z - u_z\right)\cdot\sqrt{\left(U_x - u_x\right)^2 + \left(U_y - u_y\right)^2 + \left(U_z - u_z\right)^2} - g
\end{aligned} \tag{3.1}$$

where $k = \dfrac{\rho_a C_D}{2\rho_g l}$, ρ_a = density of air, ρ_g = density of gravel, C_D = drag coefficient, l = characteristic length of gravel, g = gravity acceleration, x, y, z are the displacements in *x*-, *y*- and *z*- directions, U_x, U_y, U_z are the wind velocities in *x*-, *y*- and *z*- directions, u_x, u_y, u_z are the velocities of gravel in x-, y- and z-directions.

Once the debris is generated, it is first accelerated in the local wind field on the rooftop. The debris is considered to leave the local wind field when it is out of the transition region (Fig. 3.1c). Then the gravel enters the main wind flow field and subsequently the wake region. By updating the wind velocity for different flow regions (based on the models proposed in the Section 3.2) at each time step, Eq. (3.1) is used to calculate the trajectory of debris. The ordinary differential equation solver in Simulink is employed to solve Eq. (3.1). By tracing the coordinate/location of the flight trajectory, the final status (i.e., hitting the building or ground) of debris is determined. The impact location, velocity, and momentum of the debris that hits the building envelopes are recorded. A damage hit occurs if the impact momentum is larger than the resistance of envelope components (e.g., window panel). An envelope component is damaged when more than one damaging hit occurs in the model.

3.4 Modeling fragility of urban building envelopes subjected to windborne debris impact

3.4.1 Formulation of fragility functions

Fragilities are popular tools for accessing damage to buildings and other infrastructures (Ellingwood, 1990; Porter, 2015). A fragility describes the probability of exceeding a performance limit state conditional to a hazard intensity measure and is generally defined as:

$$F_r(x) = P(LS \,|\, X = x) \tag{3.2}$$

where *P*(*A*|*B*) is the conditional probability, *LS* is the specified limit state for the component, *x* is the random variable of hazard intensity and *x* is one deterministic value of *x*. In this study, the fragility function is first formulated for each building envelope component (e.g. one window pane). Considering that the hurricane wind speed ($V_{\max}$, maximum 3-*sec* gust wind speed at 10-*m* height), direction ($\theta_{\max}$, corresponding to $V_{\max}$) and duration (ΔT) are all important in determining the damage extent to building envelopes, all these three variables are adopted as the hazard intensity measures. Accordingly, the fragility of a building envelope component is expressed as

$$P\left(d_j = 1 \,|\, V_{\max}, \theta_{\max}, \Delta T\right) = \iiint P\left(d_j = 1 \,|\, V_{loc}, t, r\right) P\left(\mathbf{V}_{loc} \,|\, V_{\max}, \theta_{\max}, \Delta T\right) P(r) P(t)\, d\mathbf{V}_{loc}\, dt\, dr \tag{3.3}$$

where j is the identification number of the window panel, d_j is the damage indicator (d_j, if window panel j is damaged, d_j, otherwise), $P\left(d_j = 1 \,|\, \mathbf{V}_{loc}, t, r\right)$ is the conditional probability that the panel j is damaged, $P(r)$ is the probability that the characteristic size of debris is equal to r and $P(t)$ is the probability of at least one piece of gravel being generated in the time interval (*t*, *t*+1] at all initial locations. The uncertainties from the resistance of window panels, the wind turbulence, debris size and the debris generation are described in $P\left(d_j = 1 \,|\, \mathbf{V}_{loc}, t, r\right)$, $P\left(\mathbf{V}_{loc} \,|\, V_{\max}, \theta_{\max}, \Delta T\right)$, $P(r)$ and $P(t)$ respectively. $V_{\max}$, $\theta_{\max}$ and ΔT are the site-specific hazard intensity measure and can be estimated from wind hazard analysis (Wang and Wu 2022). $\mathbf{V}_{loc}$ is the interaction parameter modeling the interaction between the global wind hazard environment and the urban building cluster of interest; specifically, it represents the wind field around buildings that drives the debris flight. The resistance of the window panel to an impact momentum is assumed to follow a lognormal distribution, correspondingly,

$$P(d_j = 1 \mid \mathbf{V}_{loc}, t, r) = P(d_j = 1 \mid m, x, \mathbf{V}_{loc}, t, r) = F_j(m, x) = \phi\left(\ln\left(\frac{m}{m_R} \right) \Big/ \beta_R \right) \quad (3.4)$$

where m and x are the impact momentum and final location of debris, respectively, and are directly determined by $\mathbf{V}_{loc}$, m_R and β_R are the median capacity and the logarithmic standard deviation of the window panel j, respectively. The impact momentum is assumed to be zero if the final location of debris is out of the range of window panel j. Substituting Eq. (3.4) to Eq. (3.3), the fragility function of panel j is given by

$$\begin{aligned} F_j\left(V_{\max}, \theta_{\max}, \Delta T\right) &= P\left(d_j = 1 \mid V_{\max}, \theta_{\max}, \Delta T\right) \\ &= \iiint \phi\left(\ln\left(\frac{m}{m_R} \right) \frac{1}{\beta_R} \right) P\left(\mathbf{V}_{loc} \mid V_{\max}, \theta_{\max}, \Delta T\right) P(r) P(t)\, d\mathbf{V}_{loc}\, dt\, dr \end{aligned} \quad (3.5)$$

Based on the fragility function for an envelope component (Eq. (3.5)), the fragility of the entire building envelope is also defined. To facilitate the performance-based wind engineering, the fragility functions for multiple damage states are desired. Since the definition of damage states for high/mid-rise building envelopes are not available from previous studies, this study adopts the performance descriptors originally developed for performance-based wind engineering of wood-frame buildings by van de Lindt and Dao (2009). In this adaptation, the metrics of structural damage are replaced by that of window damage. The damage states are modified to reflect the distinct role of building envelopes (i.e., the loss of building envelopes leads to loss of functionality and building contents rather than loss of structural integrity). The four damage states are defined in Table 3.2. To construct the fragility function for each damage state, initially, the probability of l windows damaged within the entire envelope needs to be quantified. It is assumed that the failure of each window panel is independent since only the debris damage is considered and the window damage caused by the wind pressure is not investigated in this study. Thus, the change in internal pressure is not accounted, and the local wind field is not affected when one window fails. Accordingly, the probability of l windows being damaged follows a Poisson binomial distribution (Hong 2013):

$$P(L=l\,|\,V_{\max},\theta_{\max},\Delta T)=\sum_{A\in D_l}\left(\prod_{i\in A}F_i(V_{\max},\theta_{\max},\Delta T)\right)\left(\prod_{j\in A^c}(1-F_j(V_{\max},\theta_{\max},\Delta T)\right)\qquad l\in[0,K]\tag{3.6}$$

where K is the total number of windows on the building envelope, l is the number of damaged windows, D_l is a set of all possible subsets of l integers that are selected from $\{0,1,2,\ldots,K\}$, A is one subset of D_l, A^c is the complement of A and F_j is the fragility of window panel j. The percentage damage to windows can be calculated by l/K, the fragilities for different damage states are defined as follows:

$$F_s(V_{\max},\theta_{\max},\Delta T)=\sum_{l=1+p_sK}^{l=K}P(L=l\,|\,V_{\max},\theta_{\max},\Delta T)\tag{3.7}$$

where F_s represents the probability of exceedance for each damage state, where $p_s=0,0.05,0.2,0.5$ for $s=1,2,3,4$, respectively.

3.4.2 Reduced-Order and surrogate modeling for efficient computation of fragility functions

3.4.2.1 A reduced-order hurricane wind model

The fragility analysis requires the modeling of wind fields around urban buildings (i.e., $\mathbf{V}_{loc}$ in Eq. (3.5)), as described in Section 3.2. The first step is to simulate time-varying mean hurricane

Table 3.2 The building performance expectations for window damage

Damage state	Description	Percentage of window damage
1	No or little reduction in living/working comfort	<5%
2	No threat to the safety of occupant; small economic losses	5% to 20%
3	The safety of occupant is threatened; large economic losses	20% to 50%
4	Severe cascading content and building functionality losses; significant economic losses	>50%

wind. However, the data-driven hurricane model introduced in the Subsection 3.2.1 cannot be efficiently applied to fragility analysis, as the number of the model parameters is relatively large. Therefore, this section proposes two new reduced-order models to simulate time-varying mean hurricane wind speed and direction, respectively. The two models are developed as a function of $V_{\max}$, $\theta_{\max}$ and ΔT to allow the transition from global wind hazard intensity measures to the local urban wind field. Note that there are two different basic shapes of the time history of mean hurricane wind speed, i.e., single-peak or double-peak (Fig. 3.3). If the shortest distance between the interested site and the hurricane eye is greater than the radius of the maximum wind speed of the hurricane, the time history of mean wind speed only has one peak. Otherwise, the wind speed time history exhibits two peaks. The reduced-order model of wind speed is proposed based on the single-peak shape, while the double-peak case is not considered due to the following two reasons: 1) considering the double-peak case can greatly increase the input dimension of the fragility model; 2) using the single-peak shape can serve as a conservative approximation for the double-peak case. As shown in Fig. 3.3a, the time-varying wind speed can be characterized by two hazard intensity measures, i.e., the maximum 3-*sec* gust $V_{\max}$ and duration ΔT of a hurricane. ΔT is defined by the period when the wind speed is larger than 30% of the maximum wind speed (Fig. 3.3a). The reduced-order model for time-varying mean wind speed $U(t)$ is expressed by the following equation:

$$U(t) = Min\left[V_{\max} e^{-\left(\frac{t-\frac{\Delta T}{2}}{\Delta T} \bullet \frac{V_{\max}}{a}\right)^2} + 0.3V_{\max}\left(\frac{-1}{e^{\left|(t-\frac{\Delta T}{2})\frac{b}{\Delta T}\right|}} + 1\right), V_{\max} \right], t \in [0, \Delta T] \tag{3.8}$$

where t is the time points, a is an empirical constant for modification of variance, b is an empirical constant for modification of boundary and kurtosis. In this study, $a = 240\, m/s, b = 10$. This equation is proposed to ensure that the maximum wind speed and the change of wind speed resemble the time-varying wind speed in real hurricanes. The accuracy of this method is evaluated by comparing simulation results using Eq. (3.8) and the data-driven hurricane model described in the Subsection 3.2.1 (Fig. 3.4a, Hurricane Andrew (1992) is used as an example). As shown in Fig. 3.4a, the simulation results using the two models agree well. The difference is mainly due to the asymmetry of the time-varying wind speed related to the hurricane track, while Eq. (3.8) is a symmetric function and the effect of the track is not considered.

The time history of wind direction is simulated using the following model:

$$\begin{aligned} \theta_g(t) &= \cos^{-1}\left(\frac{U(t)}{V_{\max}}\right) \\ \theta_{30} &= \theta_{\max} + \max\left(\theta_g(t)\right) \\ \theta_l(t) &= \theta_g(t) + \theta_{30} - \max\left(\theta_g(t)\right) \end{aligned} \tag{3.9}$$

where $\theta_g(t)$ is the time-varying wind direction in the global coordinate system, θ_{30} is the wind direction corresponding to the later time point with 30% of $V_{\max}$ and $\theta_l(t)$ is the time-varying wind direction in the local coordinate system at the building site. The simulated wind direction using the reduced-order model shows a good agreement with that obtained using the data-driven model described in the Subsection 3.2.1 (Fig. 3.4b), which validates the accuracy of this new model.

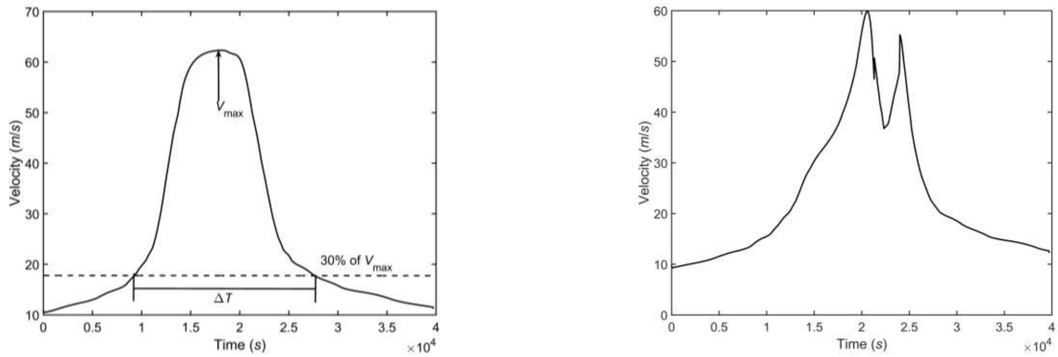

(a) (b)

Figure 3.3 Two typical shapes of time-varying mean hurricane wind speed: (a) single-peak, (b) double-peak

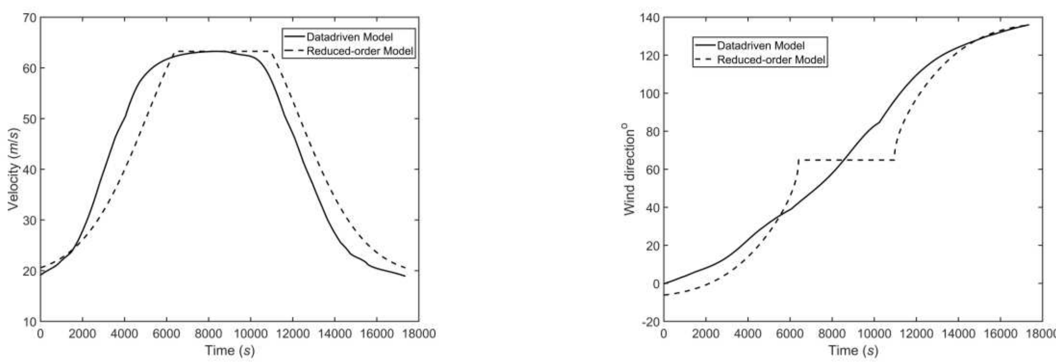

(a) (b)

Figure 3.4 Comparison of wind simulation results of Hurricane Andrew (1992) between reduced-order models and data-driven hurricane models: (a) wind speed, (b) wind direction

3.4.2.2Surrogate modeling of debris flight trajectory

The physics-based model of debris flight trajectory introduced in Subsection 3.3.2 is not computationally efficient for a large number of simulations. To facilitate simulation-based fragility analysis, this section builds surrogate models based on the physical model to increase computational efficiency. In particular, the kriging method based on the Gaussian process model is adopted for surrogate modeling. The kriging is a statistical interpolation method and the interpolated values are modeled based on the spatial correction between the sampled points. The kriging method is selected because of its unique advantages: (1) it can provide the best linear unbiased prediction of interpolated values; and (2) it is theoretically principled for quantification of model prediction uncertainties at the interpolated values (Jia and Taflanidis 2013). The inputs of the physical trajectory model include approaching wind velocity (vector form including both speed and direction) and location of debris, and the output is the impact location, velocity and the status of whether the debris can reach the vertical plane of the building before hitting the ground. In surrogate modeling, different surrogate models are built for different initial locations (as described in Subsection 3.3.1) to reduce the dimension of inputs. Accordingly, only the initial velocity is the input for the surrogate models. This dimension reduction is reasonable considering the fact that the studied initial location of debris is a function of the initial velocity (the initial locations align with the vortex core axis lines, and the direction of the vortex core axis lines is determined by the initial velocity). Since the response surfaces of different types of outputs (impact location and velocity) are distinct, separate surrogate models are built for each output. The training data for surrogate modeling is obtained by running the physical trajectory models with uniformly sampled inputs. The sampling range and frequency are determined considering the characteristic of hurricanes, the critical velocity of debris generation (direction and speed) and computational efficiency. It is assumed that the debris with an initial wind speed lower than a threshold would not hit the building. Accordingly, kriging models are built only for the debris with an initial velocity greater than the threshold velocity (the crucial velocity of debris generation can be used) to improve the computational efficiency.

3.4.3 Construction of fragilities

To construct the fragilities for envelope components and the entire building envelope, one needs to evaluate the stochastic integrals in Eqs. (3.5) and (3.7), respectively. Monte Carlo simulation can be used for this purpose. The reduced-order model for hurricane wind and surrogate model for debris flight trajectory proposed in the previous subsection are used to improve the computational efficiency of the Monte Carlo simulation. The fragility functions in Eqs. (3.5) and (3.7) have three hazard intensity measures, including $V_{\max}$, $\theta_{\max}$ and ΔT. It should be noted that $V_{\max}$ for the fragilities is the 3-*sec* gust wind speed obtained at 10 *m* height and $\theta_{\max}$ is defined as an angle between -180º and 180º measured clockwise from North to the wind direction. The fragility curves are generated by directly calculating the fragilities for each grid point in this three-dimensional space using Monte Carlo simulation and 2000 simulations are conducted for each input grid point to guarantee the convergence. Fig. 3.5 summarizes the procedure of developing fragility models of urban building envelopes.

3.5 Illustrative example

An illustrative example using the Marriott-Datran Complex in Kendall, Florida, which suffered severe window damage due to windborne debris impact during Hurricane Andrew (1992), is presented to validate the proposed debris impact model and to demonstrate the implementation of the proposed fragility modeling approach for urban buildings on both component and building levels. The Marriott-Datran Complex is selected as the example because of the availability of well-documented field data.

3.5.1 Validation of models of debris impact

3.5.1.1 Validation of physical models of debris impact

The plan view of the Marriott-Datran Complex is shown in Fig. 3.6a. Datran Towers suffered severe glass damage due to the impact of roof gravels from the Marriott Hotel (Behr and Minor, 1994). The image of the window damage in Tower 1 is shown in Fig. 3.6b (the red block in the figure indicates the unbroken windows). The physics-based modeling approach introduced in the Section 3.3 was used to predict the window damage to Tower 1. Specifically, the time histories of

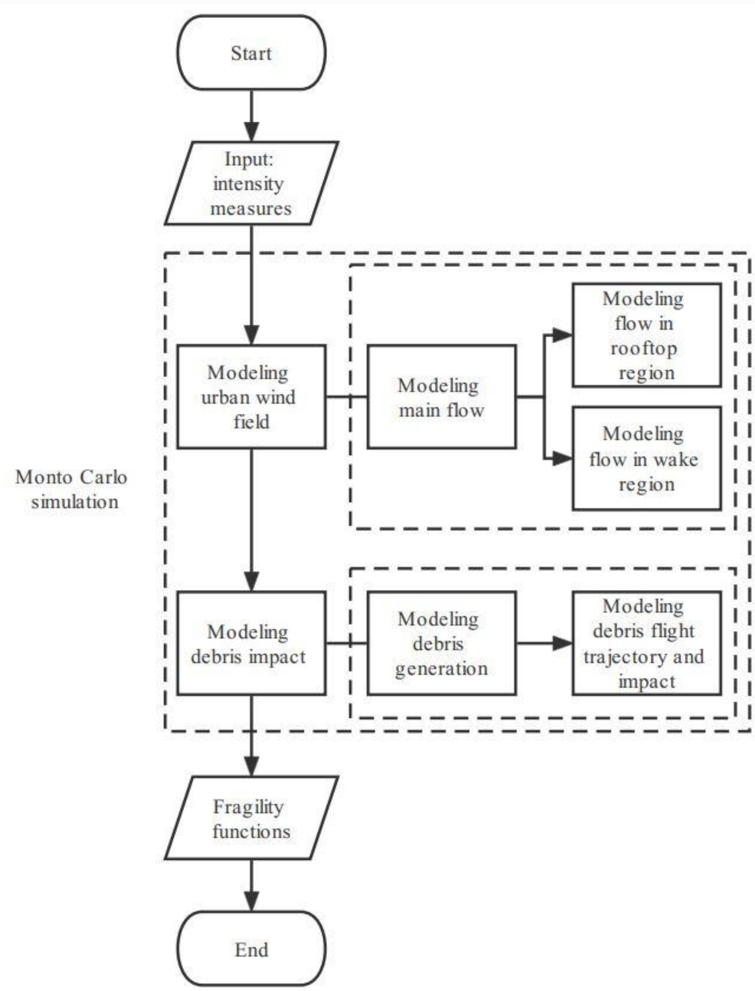

Figure 3.5 Flowchart for developing fragility models of urban building envelopes

1-*hour* mean wind velocity and direction were simulated using the method introduced in Subsection 3.2.1 (Fig. 3.4). The simulated maximum wind speed is about 63 *m/s*, which agrees well with the observed maximum wind speed at the site (62.6 *m/s*) (FEMA 2015). The wind direction changes from northerly to southeasterly (also indicated in Fig. 3.6), agreeing well with the observations (FEMA 2015). The duration $\Delta T = 5$ *hours* is used for simulating the time history of wind speed and direction. If a shorter duration is used in the simulation, less damage will be induced. However, if a longer duration is used, the damage extent will stay the same, because the lower wind velocities associated with the extended duration cannot generate extra windborne debris damage. The turbulent wind velocity was simulated using the Karman turbulence spectrum with a terrain roughness length of 0.5 *m* and turbulence intensity of 0.1824, 0.1353, and 0.0912 *m/s* in longitudinal, transverse, and vertical directions. The diameter of gravel is assumed to follow a normal distribution with a mean value equal to 12 *mm* and a standard deviation equal to 5.5 *mm* (ASTM 2000; FEMA 2015). For simplicity, debris with a diameter of 9 *mm*, 12 *mm* and 15 *mm* are selected to represent the small, medium and large gravel (debris) respectively instead of treating the debris size as a continuous variable. In addition, simulation results of damage analysis indicate that debris with a diameter close to or smaller than 9 *mm* cannot induce damage to the window panel, so only debris with a diameter of 12 *mm* and 15 *mm* are accounted for damage analysis. Debris with a diameter ranging from 9 *mm* to 15 *mm* is treated as debris of 12 *mm* and debris with a diameter ranging from 15 *mm* to 20 *mm* is treated as debris of 15 *mm* in practice. Debris with a diameter larger than 20 *mm* is not considered either as the debris would hit the ground rather than the windows. The critical wind speed for debris of 12 *mm* is about 21 *m/s* and the critical wind speed for debris of 15 *mm* is about 25 *m/s* (Kind and Wardlaw 1977) (considering the parapet height ratio is close to zero for high-rise buildings). The window glass on the Tower 1 is 6 *mm* thick fully tempered monolithic glass and the estimated average momentum resistance is 0.1 *kg-m/s* (Behr and Minor 1994; Minor 1994). The debris generation was simulated as the Poisson process using the method described in Subsection 3.3.1. The selection of debris generation rate λ is empirical. The λ is assumed to change with varying wind velocity during the event (a higher wind speed will lead to a high λ). A parametric study was conducted with various values of λ and showed that the damage extent on Tower 1 was not changing anymore when $\lambda \geq 2$, thus, $\lambda_{\max} = 2$ is used as the maximum generation rate corresponding to the maximum wind velocity during the hurricane event. The effect of debris source reduction as the wind event evolves on the debris generation rate λ is not considered, because the total number of debris generated in this hurricane event is much less than the total number of gravel debris on a rooftop. The simulated window damage is shown in Fig. 3.7a with a failure rate of 95.6% for the top ten floors, which agrees well with the observed failure rate of 97.4% (Fig. 3.6b). The current validation is based on the data for a severe damage case, future validation for low damage case（like 30%） can be done when data becomes available.

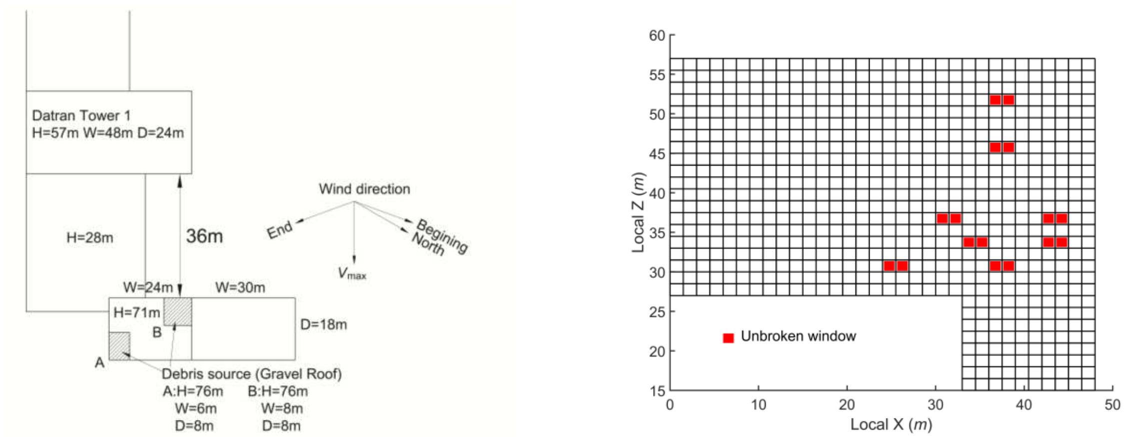

(a) (b)

Figure 3.6 Marriott-Datran Complex in Kendall, Florida: (a) plan view, (b) broken windows of Tower 1 (arrows indicating intact windows) (adapted from FEMA 2015)

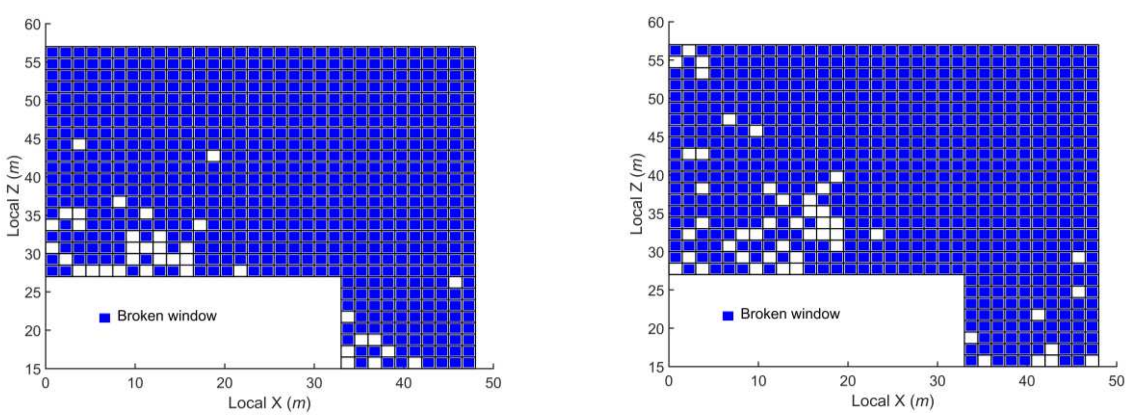

(a) (b)

Figure 3.7 Simulated window damage on Tower 1 using mean wind speed simulated by: (a) data-driven hurricane model (failure rate: 95.6%), (b) reduced-order model (failure rate: 93.6%)

3.5.1.2 Validation of reduced-order hurricane wind model

To validate the reduced-order model for the hurricane wind (developed in Subsection 3.4.2), the damage simulation was performed using the time history of mean hurricane wind velocity and direction simulated using the reduced-order model (Fig.3.4). Comparing Figs. 3.7a and 3.7b, it can be seen that the distribution for the damage pattern and failure rates for the windows using the data-driven hurricane model (window failure rate: 95.6%) and reduced-order model (window failure rate: 93.6%) are similar, validating the reliability of the reduced-order model for single-peak-type time history of mean wind speed. It should be noted that there is a shift of the predicted locations of damaged windows compared to the observation. This discrepancy is mainly due to the modeling errors in wind direction and the fact that the locations of damaged windows are very sensitive to the wind direction. Although the direction of maximum sustained wind velocity obtained from the data-driven hurricane wind field model is validated against the H*wind data with a resolution of 6 *km*, the wind direction at the building site may still have some modeling errors due to the limitation in spatial resolution of the data. For the double-peak-type of mean wind speed, the reduced-order model is expected to overestimate the damage, as discussed earlier and the extent of this overestimation was investigated herein. First, the window failure rate under a synthetic double-peak time history of wind speed simulated using the data-driven model was estimated (79%). Then the failure rate was calculated using the corresponding reduced-order model (88%). Using the reduced-order hurricane model led to about 11% overestimation of the window failure rate, which is still felt to be acceptable since the typical hurricane wind field and track models do not have a direct link to the defined intensity measures in the fragility development.

3.5.1.3 Validation of surrogate models of debris flight trajectory

The kriging models for impact locations, momentum, and the status of whether reaching the building were evaluated. Both the bias error (defined by the slope of the linear regression of predicted values versus the actual values (Bourgault 2021) and the root mean square error (RMSE) of the kriging models compared to the physical models were estimated, showing the high modeling accuracy (Table 3.3). Since debris only has two final states, the bias error is applicable for evaluating the identification result of this parameter. In this illustrative example, about 96.4% of debris is identified with the correct final status.

Table 3.3 Uncertainty of Kriging approach

Output	*X*	*Z*	*Ux*	*Uy*	*Uz*
Bias	1.0760	0.9649	1.0050	1.0250	0.9994
RMSE	6.9910 *m*	5.5080 *m*	1.0900 *m/s*	1.9370 *m/s*	0.6067 *m/s*

3.5.2 Result of fragilities

The fragilities for Datran Tower 1 were developed using the MCS introduced in Subsection 3.4.3 for $V_{\max} \in [50,115]$ *m/s*, $\theta_{\max} \in \left[20^{\circ}, 120^{\circ}\right]$ and $\Delta T \in [1, 11]$ *h*. The ranges of intensity measures were determined by considering the characteristics of hurricanes and the critical wind velocity for inducing damage. To investigate the distinct vulnerabilities of windows at different locations, the fragilities were generated for six representative windows indicated in Fig. 3.8. To allow visualizing the three-dimensional fragilities, fragility surfaces as a function of two intensity measures are shown in Figs. 3.9-3.12 with the third intensity measure fixed. It can be seen that the shapes of the component-level fragilities are quite different for windows at different locations, indicating that the influence of the three intensity measures on the probability of failure varies with the window location. As a general trend, the fragilities increase monotonically with respect to $V_{\max}$ and ΔT, respectively, which is expected. By comparing the gradient of fragility function with respect to $V_{\max}$ and the gradient with respect to ΔT, it is found that the failure probability is more sensitive to $V_{\max}$ than ΔT. The fragilities with respect to $\theta_{\max}$ show local maxima (e.g., Fig. 3.10b). This is because the windows are more vulnerable to certain wind directions. The location and number of the local maxima of the fragilities with respect to $\theta_{\max}$ vary for windows at different lateral locations (see Figs. 3.9b, 3.10b and 3.11b), depending on the lateral location of the window with respect to the debris sources. A comparison between Fig. 3.9a and Fig. 3.11a (or Fig. 3.12a) shows that the failure probability shows a steeper increase with the increase of $V_{\max}$ for the windows at the top than for the windows at the bottom. Accordingly, the windows at the top have a larger probability of failure than those at the bottom when $V_{\max}$ is high (e.g., $V_{\max} \geq 95\, m/s$, $\Delta T = 7h$); while they have a smaller probability of failure than the bottom windows when $V_{\max}$ is low (e.g., $V_{\max} \leq 70\, m/s$, $\Delta T = 7h$). This is because a higher $V_{\max}$ generates debris of higher speed that more likely damages the top windows, while a lower $V_{\max}$ initiates lower speed debris that more likely impacts the bottom windows.

The fragility on the building level evaluates the overall performance of the building envelope. It should be kept in mind that the windows in lower regions are more susceptible to debris generated by lower $V_{\max}$, while windows in the upper regions are more vulnerable under higher $V_{\max}$. For damage state 3, most of the damaged windows are in the low regions. Correspondingly, damage state 3 will be exceeded with a high probability at a relatively low $V_{\max}$ (Fig. 3.13a), which shows similar trends as the component level fragilities of windows in lower regions (e.g., windows No. 3 and No. 5 in Figs. 3.10-3.11). For damage state 4, the damaged windows spread more towards the upper region. Accordingly, the fragility function for damage state 4 (Fig. 3.14) has a similar trend as that for top windows (e.g., window No. 1 in Fig. 3.9), where the high probability of exceedance is associated with a higher $V_{\max}$ compared to that for damage state 3. As mentioned before, the influence of wind direction varies with the lateral location of windows and the fragility on the building level depends on the overall performance of all windows. Thus, the fragility with respect to $\theta_{\max}$ on building level is more uneven and has more local maxima (Fig. 3.14b) than that at the component level (e.g., Fig. 3.11b). A longer duration of hurricane leads to a high failure probability exceeded at a lower $V_{\max}$, indicating that slower-moving hurricanes (or tropical cyclones in general) might be more devastating. The comparison between Fig. 3.13a and Fig. 3.14a shows that such an influence of duration is more significant on damage state 4 than on damage state 3. As mentioned before, the influence of wind direction varies with the lateral location of windows and the fragility curves on the building level depend on the overall performance of all windows. Thus, the fragility curves associated with $\theta_{\max}$ on building level are more uneven and have more local extreme points than the component level.

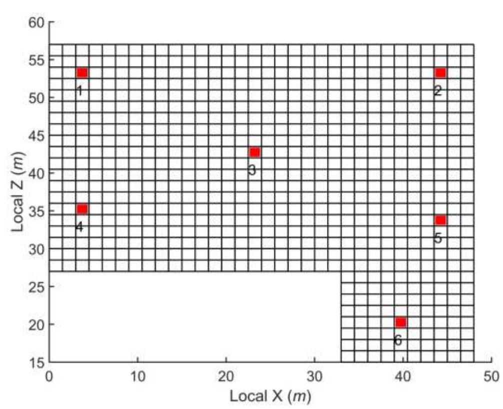

Figure 3.8 Locations of representative windows

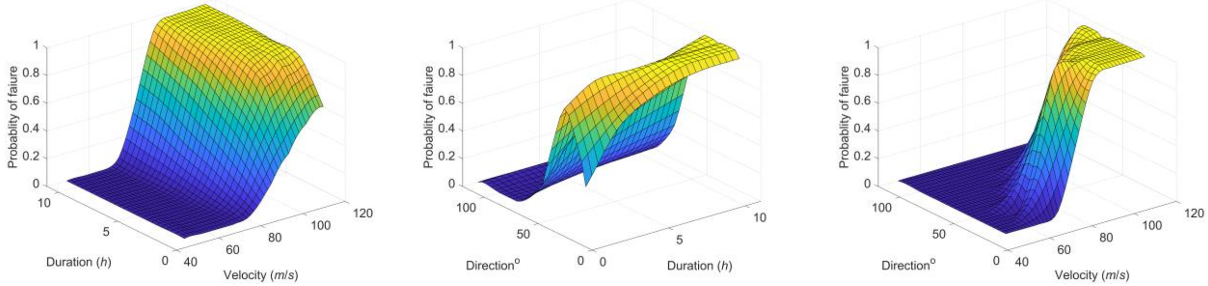

(a) (b) (c)

Figure 3.9 Component level fragility for Window No. 1: (a) $\theta_{\max} = 60^{\circ}$, (b) $V_{\max} = 90$ m/s, (c) $\Delta T = 7\ h$

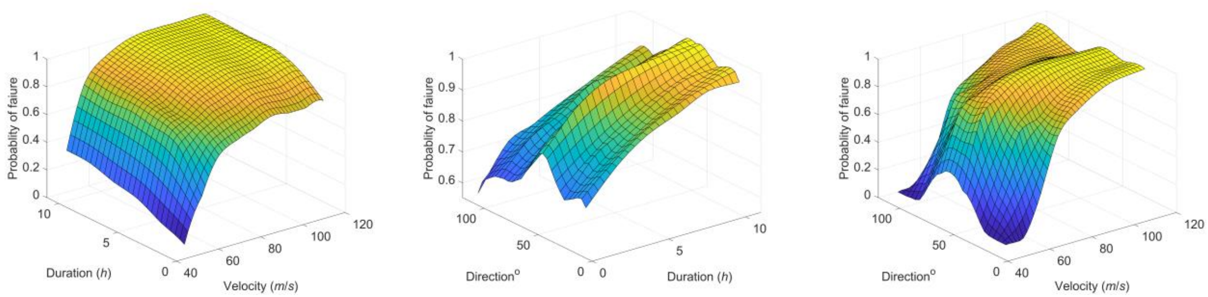

(a) (b) (c)

Figure 3.10 Component level fragility for Window No. 3: (a) $\theta_{\max} = 60^{\circ}$, (b) $V_{\max} = 90$ m/s, (c) $\Delta T = 7\ h$

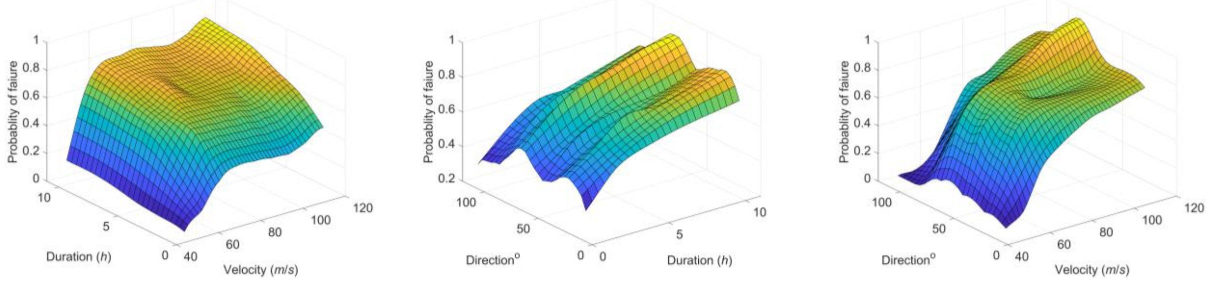

(a) (b) (c)

Figure 3.11 Component level fragility for Window No. 5: (a) $\theta_{\max} = 60^{\circ}$, (b) $V_{\max} = 90$ m/s, (c) $\Delta T = 7\ h$

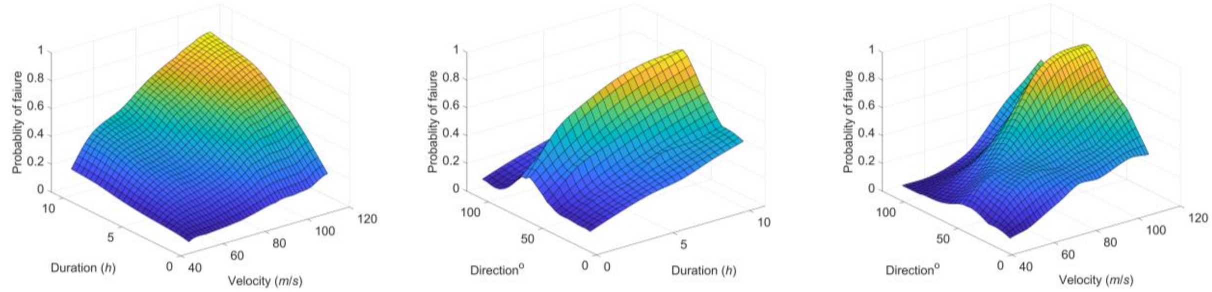

(a) (b) (c)

Figure 3.12 Component level fragility for Window No. 6: (a) $\theta_{max} = 60^{\circ}$, (b) $V_{max} = 90$ m/s, (c) $\Delta T = 7 \ h$

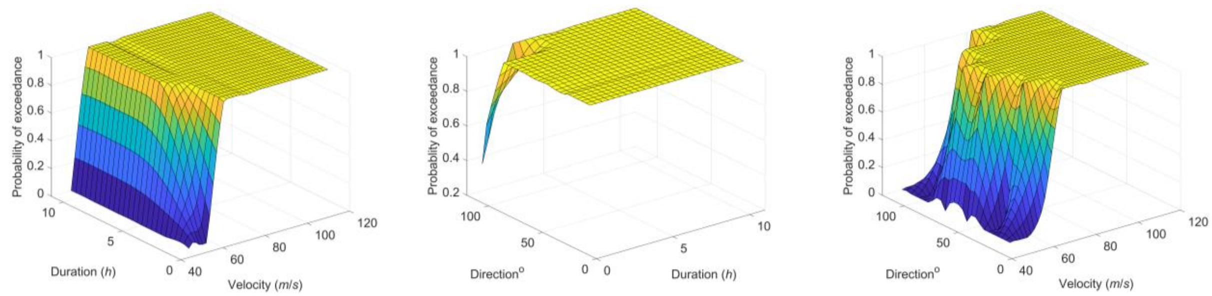

(a) (b) (c)

Figure 3.13 Building level fragility for damage state 3: (a) $\theta_{max} = 60^{\circ}$, (b) $V_{max} = 90$ m/s, (c) $\Delta T = 7 \ h$

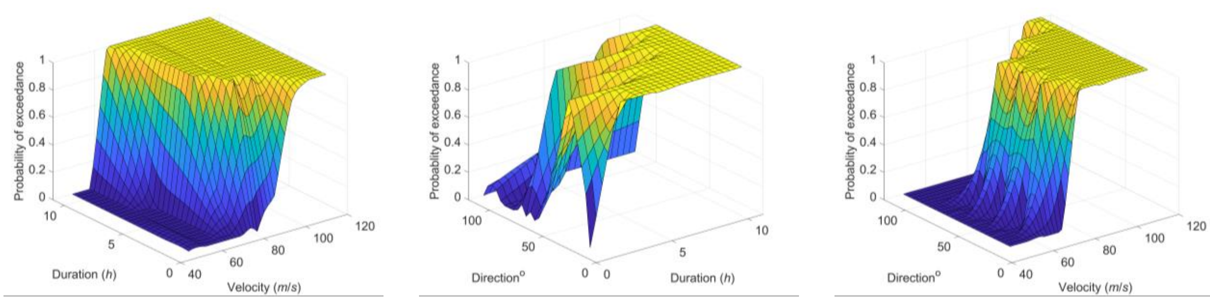

(a) (b) (c)

Figure 3.14 Building level fragility for damage state 4: (a) $\theta_{max} = 60^{\circ}$, (b) $V_{max} = 90$ m/s, (c) $\Delta T = 7 \ h$

3.6 Discussions

The factors influencing the modeling of debris damage can be divided into two groups. One group is the factors associated with the simulation of the wind velocity field, including turbulence, local vortices, and the wake effect. The other group is the factors related to debris generation, including the size, location and generation rate of debris. In this section, the significant role of each factor in debris damage modeling is investigated via the illustrative example of the Marriott-Datran Complex with extra tests, to inform future modeling efforts for more generic debris damage cases.

Turbulence effect: To study the effects of turbulence, the damage pattern simulated without considering turbulence in the main flow (Fig. B.3) was compared to the result with consideration of turbulence (Fig. 3.7). It is seen that the debris damage only occurs in some small areas for the former, while the damage spread out over the entire façade for the latter. This reveals that although the mean wind velocity is the dominant factor governing the final location and velocity of debris, only considering the mean wind will lead to the concentration of the debris in several locations and underestimate the debris damage extent significantly.

Effect of local vortices: To investigate the effect of local vortices on the debris damage, the initial velocity and movement when the debris is leaving the vortex region and flying into the main flow region are investigated. Most of the debris moves less than 0.2 *m* in the vortex region, however, the initial velocity is considerable (Fig. B.4). This suggests that the vortex is quite efficient in accelerating the debris and can induce a large initial velocity of debris. Since the trajectory of debris flight is the most sensitive to initial conditions, the local vortices play an essential role in debris damage modeling.

Wake effect: The damage pattern without considering the wake effect (i.e. using the boundary layer wind profile as the main flow field) (Fig. B.5) is compared with the result with the modeling of the wake effect (Fig. 3.7). For the latter, there is more debris attacking the bottom part of the façade, because the wake effect reduces the horizontal wind velocity, causing debris to fall more downward under gravity. This analysis shows that the modeling of the wake effect is very important for the accurate modeling of debris damage patterns.

Size of debris: The average size of debris in the example of the Marriott-Datran Complex is 12 *mm*, while the actual size may range from 9 to 15 *mm*. The influence of debris size is studied by comparing the damage patterns induced by the debris of 12 and 15 *mm* and debris of 9 *mm* abandoned for reasons mentioned in the previous section, respectively. The result in Fig. B.6 shows that damage simulated using smaller debris tends to cluster on the upper floors and the total damage extent is less compared to larger debris. This is because the smaller debris tends to have a larger horizontal speed and less travel time (dropping down less), meanwhile they have less impact momentum. These difference in damage patterns suggests that modeling the randomness in debris size is necessary to recover the actual damage pattern observed in the field.

Location of debris source: In contrast to the existing studies where the debris source is typically assumed to be at one location (FEMA 2015), this study modeled the debris generation from multiple locations along the axes of roof vortices (Fig. 3.2). The necessity of considering multiple locations is investigated by comparing the debris damage patterns using debris from each of the six locations in Fig. 3.2, respectively (Fig. B.7). It is seen that locations of debris sources can influence the lateral distribution of window damage. The debris generated under the left vortex in Fig 2 which is closer to the target building (e.g., location No. 1, 2, 3) caused concentrated damage to the upper part of the façade, compared to debris under the right vortex due to variation of transport time for debris from different locations. This result shows that the damage pattern is sensitive to the initial debris locations. This is because the dimension of debris source roof A or B is considerable compared to the distance between the source building and the target building. Thus, appropriate modeling of debris generation locations is important in such cases.

Debris generation rate (λ): A higher λ result in more flying debris during a hurricane. More debris tends to attack a larger area on the façade and each window may be attacked by more than one piece of debris, leading to a higher chance of damage and severer damage to the entire façade. However, this effect of higher λ on damage extent tends to saturate when λ is sufficiently high, as indicated in the parametric study to determine λ in Section 3.5. Physically, λ is controlled by multiple factors including the approaching wind velocity, the debris weight and the critical wind velocity, etc. and is difficult to be determined analytically. Before more experimental evidence becomes available, the λ can be empirically determined based on parametric studies as proposed in this Chapter.

3.7 Application of fragilities in building design and risk assessment

In current building design practice, the building envelope is designed and tested to resist debris impact with prescribed impact momentum or energy. The prescribed debris impact momentum and energy are obtained from debris impact speed, which is determined by the basic design wind speed and the risk category of buildings according to the testing procedure of ASTM E1886 standard (ASTM 2013). The impact speed of the small missile is between 0.40 and 0.85 of the basic design wind speed, while the lower and upper bounds of impact speed for the large missile are 0.10 and 0.55 of the basic design wind speed, respectively (ASTM 2013). This prescriptive design approach cannot consider uncertainties of debris sources, building cluster geometry, and the local wind field around the buildings. Due to these limitations, the current design approach may not be sufficient to ensure satisfactory building envelope performance, as evidenced by a large number of building envelopes damaged in hurricanes.

The fragility approach proposed in this Chapter will advance the envelope design by allowing a performance-based design (PBD) approach in the framework of performance based wind engineering (PBWE) (Ouyang and Spence 2020) to address the practical issues of debris-induced damage of tall building envelopes. The steps of application of the developed fragilities in the PBWE framework are exemplified below. Step 1: Determine the target performance. In the PBWE framework, the performance of building envelopes can be defined in terms of the mean annual rate of exceeding a damage state (decision variable). The target performance can be defined as the mean annual rate of building window damage exceeding a certain damage state being less than a threshold. Step 2: Determine the joint probability of hurricane wind speed, direction and duration at the building site using simulated hurricanes. The data of maximum wind speed, direction corresponding to the maximum speed and duration of the simulated hurricane events are used to fit a joint probability function $p(V_{\max}, \theta_{\max}, \Delta T)$. Step 3: Estimate the mean annual rate (λ_s) of building window damage exceeding a certain damage state *s* through convolution of fragilities and hurricane hazards, i.e. $\lambda_s = \lambda_e \int F_s(V_{\max}, \theta_{\max}, \Delta T) p(V_{\max}, \theta_{\max}, \Delta T) dV_{\max} d\theta_{\max} d\Delta T$, where λ_e is the arrival rate of hurricane event. Step 4: Check whether the target performance is achieved. If the target performance is not achieved, increase the resistance of window glass, and repeat steps 1 to 3 until the performance target is achieved.

The proposed fragilities can also be used for community resilience analysis, where an assessment of performance metrics such as building loss, and loss of functionality, can be analyzed. Specifically, given a scenario hurricane, the fragilities are firstly used to estimate the probability of each damage state based on the intensity measures. Then using performance metrics (e.g. loss) associated with each damage state and the probability of each state, the expected value of performance metrics is estimated, which is served as the basis for resilience analysis and planning.

3.8 Concluding remarks

In this study, a new fragility modeling approach for urban high/mid-rise buildings envelopes subjected to hurricane-driven windborne debris hazards at both the component and building level is proposed. These fragilities can be readily used in performance-based engineering through the convolution of fragilities and hurricane hazards (represented as the joint probability distribution of $V_{\max}$, $\theta_{\max}$ and ΔT). These fragilities can also be used to assess the risk of building envelopes for scenario hurricane events and thus are very useful in community resilience analysis. The following conclusions are drawn:

- The proposed fragility model explicitly considers the geometric configuration of urban building clusters and the environment of debris sources, allowing more accurate risk quantification.
- The proposed fragility models enable the rigorous propagation of uncertainties from hurricane wind hazard, local urban wind field, debris size, location and generation, as well as the resistance of envelope component.
- To tackle the challenge of the complexity of the urban wind field, a unique wind field modeling technique is proposed, where the turbulence, wake effect and local vortices are modeled using stochastic simulation, wind tunnel data and parametric models, respectively.
- To facilitate the fragility development, a new reduced-order model is proposed to key the hurricane wind simulation directly to the three intensity measures of fragilities. Kriging models were applied as surrogates of the physics-based trajectory model to improve the efficiency of computing debris trajectory.
- The constructed fragilities of the illustrative example suggest that slower-moving hurricanes with longer duration might be devastating even at a relatively low intensity. Considering the plausible expectation that the translation speed of tropical cyclones has slowed due to global warming (Kossin 2018), building envelopes might be at a higher risk of windborne debris damage under future climate.

CHAPTER 4 DATA-DRIVEN MODELING OF URBAN WIND FIELD USING MACHINE LEARNING APPROACH

4.1 Introduction

In this Chapter, a data driven model of urban wind field that can be used for the simulation of windborne debris trajectories is proposed using a ML approach. The building configurations and inflow wind profile are used as the input, the 3D wind velocity field around buildings are used as the output. The conditional Generative Adversarial Networks (cGANs) is adopted to build this data driven model. Common potential debris sources in urban region include gravels on the building rooftop, other roof components and broken glass pieces of windows from debris source buildings (Lin, 2005). Accordingly, a basic building cluster with two buildings including one debris source building and one target building are studied in this Chapter. Given that fact that there is no existing public data of wind velocity field around high rise building clusters, this study uses CFD simulations to generate data of wind velocity field for different configurations of two building clusters, and then trains a cGANs model to predict the wind field. Typically, ML approaches require a large amount of training data, while the CFD simulation can be expensive for generating the training data. To tackle this challenge, this study proposes a systematic approach to strategically select samples in input space that are most informative for model training to reduce the amount of data needed and computational demand for CFD. This Chapter first presents the composition of input space and output space for this problem. Subsequently, the CFD simulations used for generating the training dataset and the cGANs model applied for developing the data-driven prediction model are described. Following that, an efficient sampling strategy is proposed for reducing the computing cost in generating the training dataset. Finally, the prediction results of wind velocity field are discussed.

4.2 Problem formulation

4.2.1 Model input and output

The first set of input of the data-driven model is the geometric configuration of urban building clusters. The aerodynamic interference among buildings in an urban environment is critical to accurately assessing the debris impact to urban building envelopes, as the genesis and transport of windborne debris is sensitive to the surrounding wind field. Accurate building configurations including the number, location and geometry of buildings are essential for simulating the surrounding wind field with aerodynamic interference effects. To enable debris impact assessment for various building cluster configurations, the configuration of urban building clusters is selected as the input of the data-driven model. In this study, a basic type of building clusters with one source building and one target building are investigated. The building configuration is determined by the relative locations and height of the two buildings. The breadth, depth and height of the target building are 28 *m*, 28 *m* and 112 *m*, respectively. The breadth and depth of the source building are also 28 *m* while the height of the source building hs is assumed to be equal to or lower than 112 *m* in different cases. Note that the building dimensions are selected based on geometries of two-building clusters in the public wind tunnel data from the Tokyo Polytechnic University (TPU) to leverage the existing data for CFD model validations. The relative locations of the two buildings are determined by the horizontal offset distance d_x and the vertical offset distance d_y between the center of building footprints as shown in Fig. 4.1. The layout of the two-building cluster can be controlled using the three parameters hs, d_x and d_y.

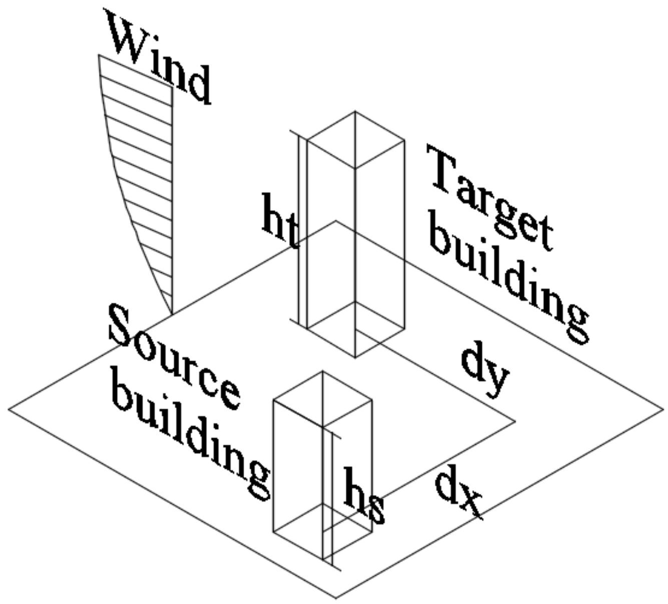

Figure 4.1 Configuration of a generic two-building cluster

The second set of the model input is the inflow wind profile for the building cluster. The inflow wind profile includes the wind speed and direction profile, which can be estimated through spatial downscaling of the global wind field. For example, for a hurricane, the wind speed and direction can be obtained from measurement data (Uhlhorn et.al.,2007), parametric or other types of hurricane wind field model (Li and Hong, 2016), over the urban city. During a windstorm, the mean wind speed and direction at a reference height typically change over time. Turbulence is another important factor in assessing debris impact, as it is one of the major source of uncertainties in debris trajectories. The authors' previous study (Dong et.al., 2023) has shown that only taking the turbulence in the inflow wind speed into account rather than considering turbulence during the debris flight can lead to similar statistical distributions of debris trajectories, while the former is much more computationally efficient. Accordingly, the wind speed and direction of inflow at the reference height are modeled as the summation of time-varying mean and a fluctuating component to consider the turbulence effect. Then taking the wind speed and direction at each time point as the input, the proposed data-driven model aims at predicting the resulting wind field. To this end, this study proposes to use scalars of wind speed and direction at the reference height as the input of the data-driven model. Further, to reduce the dimension of input parameters, only the inflow wind direction α is considered as an input parameter of the data-driven model, while the inflow wind velocity is considered by scaling the output data. The scaling approach for wind speed is applicable in this case considering the fact that the range of wind speed that may induce windborne debris damage in urban region is limited according to authors' previous study (Dong et.al., 2023) and the corresponding Reynolds Numbers should be similar.

In summary, the input space of the data driven model is composed of the height of the source building hs, the horizontal offset distance d_x, the vertical offset distance d_y and the inflow wind direction α. The output space of the data driven model includes the 3D wind velocity field over the building cluster. Furthermore, the range of the four parameters of building configuration and the wind direction is determined considering the computational cost and previous study of debris risk in urban areas (Dong et.al., 2023). Table 4.1 shows the range of all the parameters in the input space. It should be noted that the source building is assumed to be equal to or lower than the target building according to the trajectory of gravel and reports of debris induced damage in urban areas (Jain, 2015).

4.2.2 Formulating wind field prediction problem as a image-to-image transformation task

The problem of wind field prediction is formulated as the problem of image-to-image transformation problem to tap the potential of recent machine learning models, which are very powerful in dealing with image data. Specifically, the aforementioned input and output data discussed in the previous section are represented as 2-D images. For the input, the corresponding image should reflect the three parameters of building configuration and the inflow wind direction.

Table 4.1 Selected range of parameters in the input space

Parameter	Range	Parameter	Range
hs	[56 m, 112 m]	d_y	[0 m, 84 m]
d_x	[56 m, 140 m]	α	$[-30°, 30°]$

The corresponding image of the building cluster in Fig. 4.1 is shown in Fig. 4.2. The building cluster is rotated according to the wind direction in Fig. 4.2 as mentioned before. In this case, the horizontal offset distance dx and the vertical offset distance dy are directly reflected in the projection of building footprints, the height of the source building hs is described through the grayscale number and the inflow wind direction is considered by rotation of the entire building cluster with the corresponding angle. It should be noted that if the building cross-section varies with height, the image will be like a contour map. Furthermore, the data-driven model can be extended for complex building configurations with irregular building geometries by representing the input space using images. The magnitude of wind velocity U_m and the three components of local wind velocity U_x, U_y, U_z at different vertical layers between the ground and the rooftop of the target buildings are illustrated as 2-D wind velocity contours, which can be directly used as the output image for developing the data-driven model after normalization considering the size of building clusters (computational domain) and the range of wind velocity. The images of local wind velocity field with different sizes of building clusters (computational domain) are projected to images of the same size and the same color map is used for wind velocity contour with different wind profiles at the inlet boundary. Examples of the 2D wind velocity contours are shown in Fig. 4.3. The 3D wind velocity field is reconstructed with linear interpolation between the 2D contours at different heights.

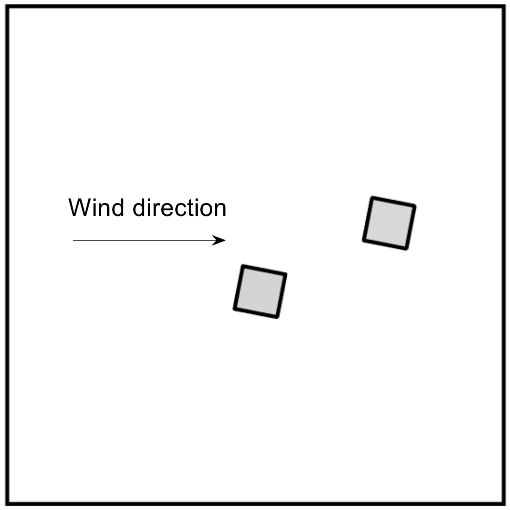

Figure 4.2 2D input image of an example building cluster configuration

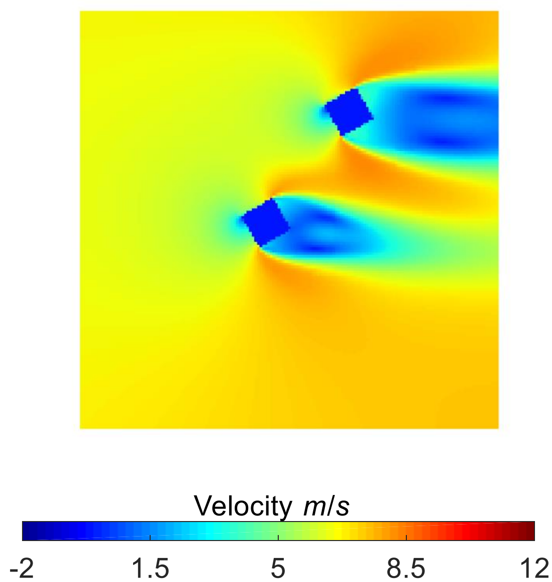

(a)

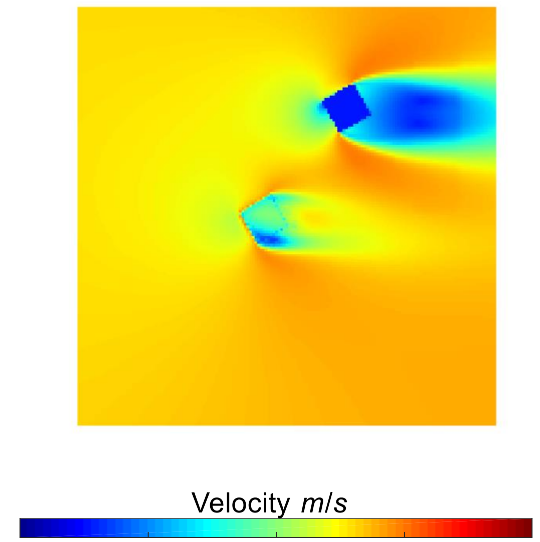

(b)

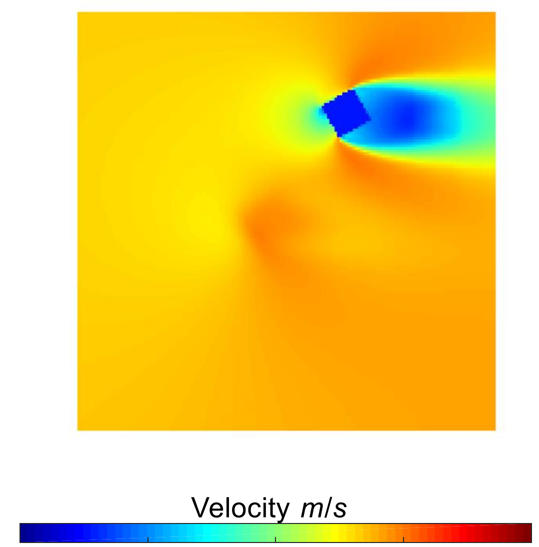

(c)

Figure 4.3 2D contours of wind velocity field at different height level z (Source building $hs = 84$ m, Target building $ht = 112\,m$): (a) $z = 50.4\,m$ (b) $z = 84\,m$ (c) $z = 95.2\,m$

4.3 Generation of wind velocity field data

The training data for the data-driven model is obtained using CFD simulations with the Reynolds-Averaged Navier-Stokes (RANS) model. The commercial software FLUENT was used for numerical simulation and all the simulations were conducted on the Asha High Performance Computing Cluster at Colorado State University. The parameter setting for the numerical simulations is consistent with the TPU aerodynamic dataset for two-building configurations, since the wind tunnel test data in TPU dataset is used for validation of the CFD models. Thus, the scale factors of the numerical simulations are set to be the same as the TPU dataset, i.e. length scale1:400, and time scale 1:80. The size of the computational domain is 6 m long, 2.2 m wide and 1.8 m high (Fig. 4.4), which is the same as TPU wind tunnel tests. The two buildings are both 0.07 m long and 0.07 m wide while the target building is 0.28 m high while the height of source building varies in different cases. The blockage ratio is around 1%, which is acceptable (Liu and Niu, 2016). The inflow wind profile including the mean wind speed $U(z)$ and turbulence intensity $I(z)$ is shown in Fig. 4.5. The power law vertical wind profile is used to simulate mean wind speed of inflow with the exponent $\beta = 0.27$ in urban region. The mean wind speed and turbulence intensity at the roof height of the target building is 8.2 *m/s* and 19.8% respectively. The SST k-omega model is selected for defining the turbulent wind flow, and the turbulence kinetic energy $k(z)$ and the specific dissipation rate $\omega(z)$ are defined in Eq. (4.1),

$$
\begin{aligned}
k(z) &= \frac{3}{2}\left(I(z)U(z)\right)^2 \\
\omega(z) &= C_\mu^{\frac{3}{4}} \frac{k(z)^{\frac{1}{2}}}{l(z)}
\end{aligned}
\tag{4.1}
$$

where C_μ = 0.09, $l(z)$ is the turbulent length scale obtained from the TPU dataset and z is the height.

The computation domain was meshed using the poly-hexcore grids in FLUENT with a minimum grid size equals to 0.005 *m*. The calculation is assumed to be finished with the residuals of continuity less than 10^{-3}, k and ω less than 10^{-4} and the other factors less than 10^{-5}. In this way, the mesh numbers and computing time for each case in this study are around 3.8 million and 2 hours.

The numerical simulation results were validated with the TPU aerodynamic dataset. It should be noted that the TPU dataset only provides the pressure coefficients on the building wall surfaces and the wind tunnel test data for the 3D wind velocity field over the building clusters are lacking. Thus, the numerical simulation results in this study are validated moderately based on pressure data. The validation results of the pressure coefficients on the target building, which is called the principal building in the TPU dataset, for one building cluster ($hs = 0.28\ m$, $d_x = 0.28\ m$, $d_y = 0.14\ m, \alpha = 0°$) are shown in Fig. 4.6. The simulation results of other building clusters are also validated, as summarized in Table 4.2. The bias error (Bourgault 2021) is close to 1 and the root mean square error (RMSE) is low for the comparsion of the numerical simulation results and the wind tunnel test results indicating that the numerical simualtion results have high accuracy and should be trusted.

Table 4.2 Comparison results between the CFD simulation and wind tunel test for some building clusters

Building cluster	Input parameters				Bias error	RMSE
	hs (m)	$dx\,(m)$	$dy\,(m)$	α (°)		
1	0.14	0.28	0.14	0°	0.9744	0.0825
2	0.14	0.35	0	-15°	0.9576	0.0577
3	0.28	0.28	0	0°	1.016	0.0766
4	0.28	0.35	0.14	15°	0.9864	0.0569

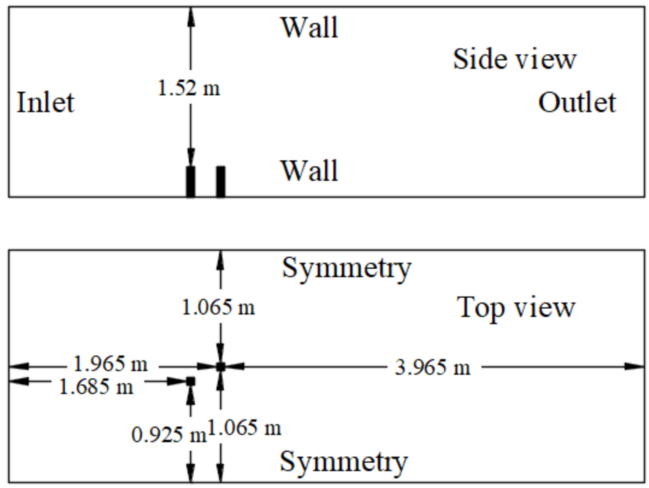

Figure 4.4 Computational domain in CFD simulation

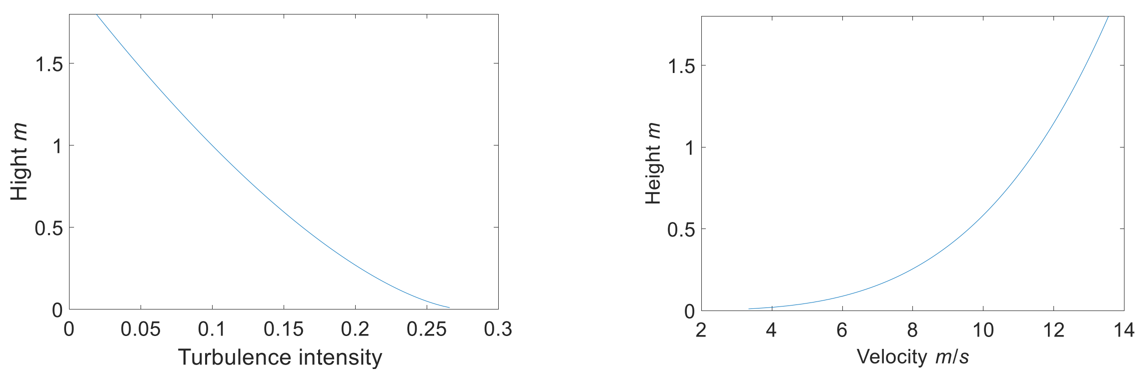

(a) (b)

Figure 4.5 Inflow wind profile: (a) Turbulence intensity (b) Velocity

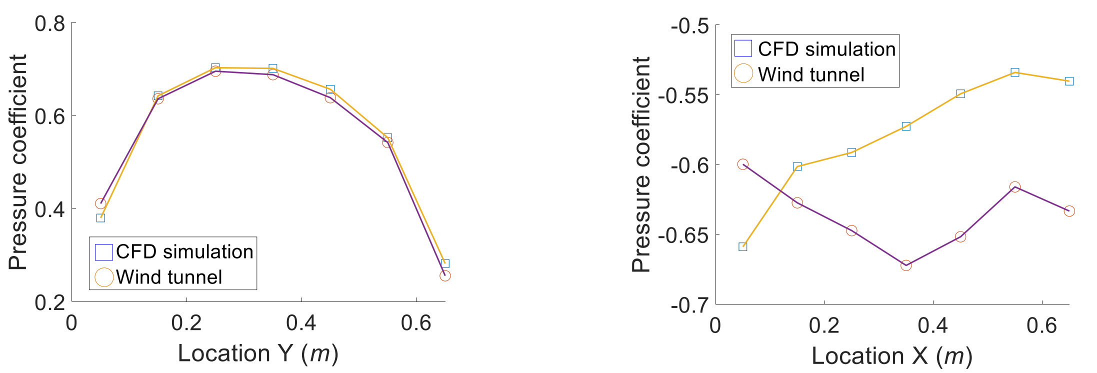

(a) (b)

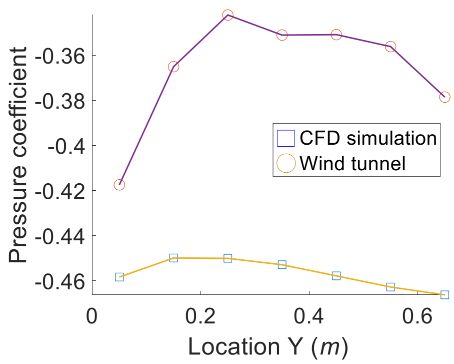

(c)

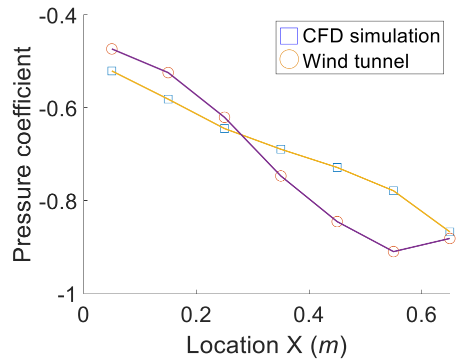

(d)

Figure 4.6 Validation results of numerical simulation: (a) Wardwall at height = 0.19 *m* (b) Right wall at height = 0.19 *m* (c) Leewall at height = 0.19 *m* (d) Left wall at height = 0.19 *m*

4.4 Data-driven modeling for predicting urban wind velocity field

4.4.1 Selection of machine learning model

Data-driven models for the 3D wind field over building clusters are developed with ML approaches. As discussed in Section 4.2, wind field prediction problem has been formulated as an image-to-image transformation task, where the input is the image represents the geometry of building clusters and wind direction (via orientation of building cluster) and the output is the wind velocity field contour map. The ML approaches that are especially effective in handling image prediction include Convolutional Neural Networks (CNN) (Gu et.al.,2018; Yamashita et.al., 2018) and Generative Adversarial Networks (GANs) (Creswell et al. 2018; Wang et al. 2017; Gui et al. 2021). CNN can directly output the predicted image as a supervised machine learning algorithm by minimizing the loss function in the training process. Using the common Euclidean distance based loss function may generate blurry predicted images (Isola et.al 2017). Furthermore, the design of an effective loss function itself is a non-trivial task, so CNN is not adopted in this study. GANs is a form of generative model for images using machine learning methods for unsupervised learning. Since GANs is unsupervised, manually designing the specific loss function is not required. Instead, GANs can automatically learn a loss function to predict realistic images and blurry images will not be accepted since they are different from the input images and considered as fake by GANs. Given the convenience of GANs without the need of designing loss functions, GANs are selected to generate data-driven model in this study.

GANs are comprised of two competing models: a generator model for generating new samples from input space and a discriminator for classifying samples as real or fake. Through iterations, the discriminator is updated for better classifying real and fake samples while the generator is updated based on the performance of discriminator for generating samples that can fool the discriminator. By training the two competing models simultaneously, GANs can automatically generate new examples with the same statistic characteristic as input data by discovering and learning the regularity in the input space. However, since GANs are based on unsupervised learning, the new samples generated are generated randomly from the input space while generating samples with target distributions on the condition of inputs are not achievable. In other words, GANs can only simulate good images of wind fields that resembling the data but the relationships between wind field and inflow wind profile and building configurations cannot be learned. To facilitate the modeling of the input and output relationships in this study, a variation of GANs, namely conditional GANs (cGANs) (Isola et.al 2017) is used. The generative model in cGANs is trained to generate new samples with the same statistic characteristic of the training data conditioned by some additional input. The additional input could be a class label, a digit, or an image. In this study, the images that represent building configuration and inflow wind direction serve as the additional input. The discriminator in the cGANs is also conditioned on the additional input of building configuration and inflow wind direction. In this way, cGANs can be used to generate the wind field associated with the building configuration and inflow wind direction. The code of cGANs models used in this study is developed based on the Pix2Pix approach proposed by Isola et.al (2017). Fig. 4.7 presents a flow chart of cGANs framework for predicting urban wind velocity fields.

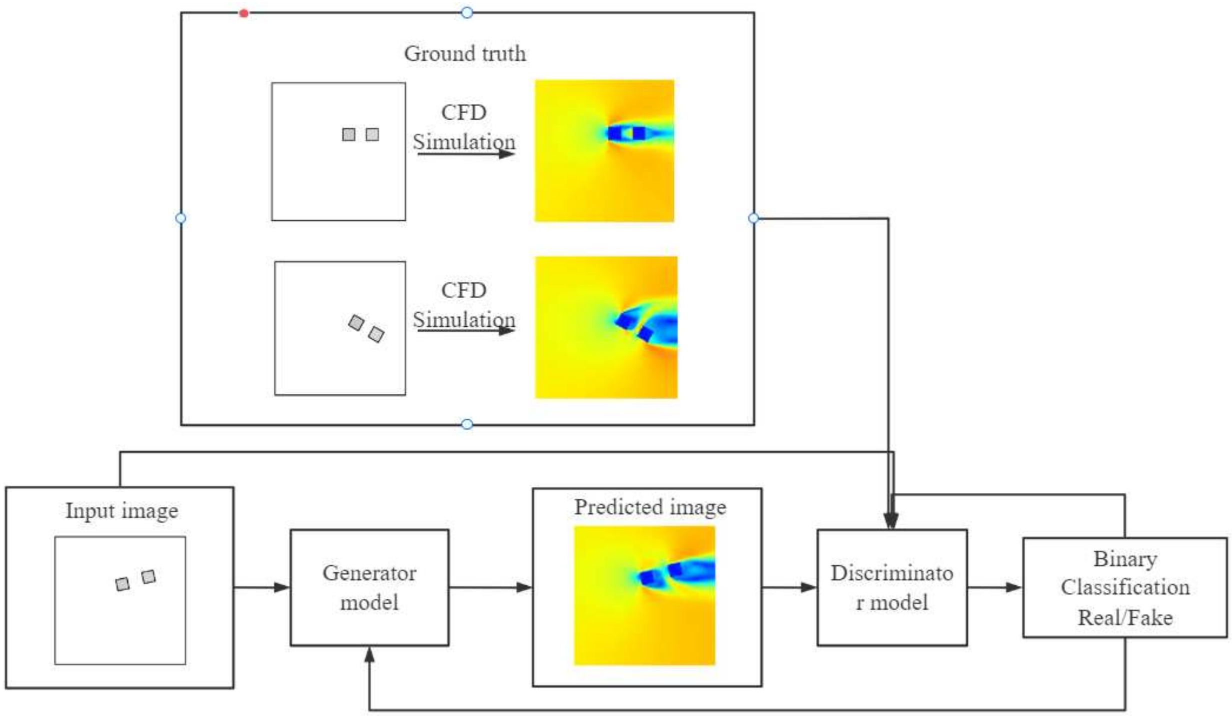

Figure 4.7 A flow chart of cGANs framework for predicting wind velocity field

4.4.2 Strategies to improve accuracy of data-driven model while reducing data need

The cost of generating training data for developing data-driven models is high, even when using RANS models which are cheaper than wind tunnel tests and Large Eddy Simulation (LES) models. This study has developed a set of strategies to reduce the data demand while improving the model accuracy. The *first* strategy is to sample the training data more efficiently based on the importance of input parameters, which will be discussed in Section 4.5. The *second* strategy is to build separate data-driven models for each height level. Considering that the 2D velocity contours at different heights may exhibit different spatial variations due to the 3D flow structures around building clusters as shown in examples in Fig. 4.3, building separate data-driven models for each height is expected to improve the modeling accuracy. Note that 2D velocity colormap at the same height as or lower than the rooftop of the lower building shows the projection of the two buildings, which represents the region of zero velocity (Fig. 4.3a-b), while the 2D velocity colormap between the rooftop of the two buildings only include the projection of the taller building (Fig. 4.3c). To effectively use cGANs, the input images that represent building configuration and wind direction and output images of the 2D wind field should have some similarity, since the common application of cGANs is to transform sketches to photos (Isola et.al., 2019). Accordingly, the input images for the data-driven models at different heights are constructed in such a way that only the footprint of the taller building is shown for predicting wind field between the rooftops of the two buildings, while the footprints of both buildings are present for predicting wind field below the rooftop of the lower building. The grayscale number for the projection image of the taller building is described by the height difference between the two buildings instead of the real height for predicting wind field between the rooftops of the two buildings. Note that the training data is comprised of building cluster configurations with different building heights. The heights of the buildings need to be normalized to allow building prediction models for building cluster configurations with various heights. Specifically, the height values z_n between the ground and the rooftop of the source building is scaled from 0 to 1 and the height values z_n between the rooftop of the two buildings is scaled from 1 to 2 as well. In this way, the 2D contours at the same normalized height level are used to develop the data-driven models. The *third* strategy is to reduce the domain of output to further improve the prediction accuracy. The generation, transport and impact of gravel usually occur in the regions close to the two buildings. Thus, only the prediction of wind velocity fields in the nearby regions are required for data-driven modeling in the context of debris impact simulations. Fig. 4.8 shows the region of wind field studied in the data-driven model, which is much smaller than the computational domain in CFD simulations.

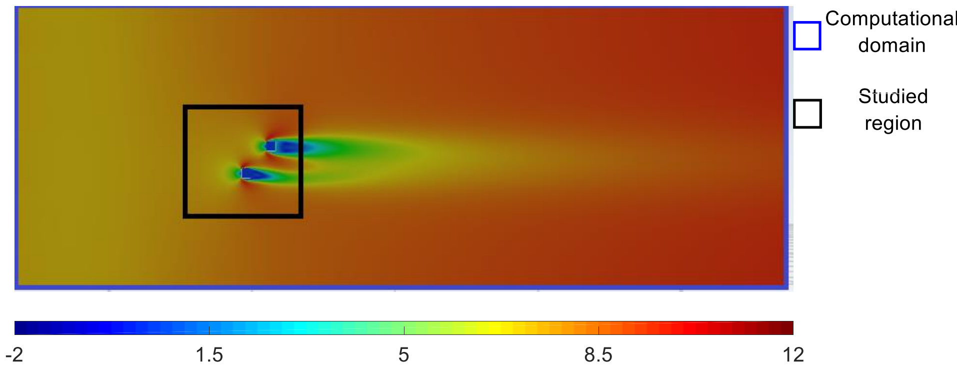

Figure 4.8 Region of wind field studied in the data-driven model

4.5 Sampling strategy

To efficiently sample the input space when generating training data for the data-driven model, a uniform sampling approach guided by sensitivity analysis is proposed. Sensitivity analysis is applied to analyze the influence of four input parameters on the performance of the data-driven model and guide the sampling. The physics-based model of CFD is nonlinear, thus the input parameters are expected to have significant variations in uncertainty in different value ranges. Typically, for this type of nonlinear system, global sensitivity analysis is more suitable than local sensitivity analysis. However, global sensitivity analysis requires densely sampled data to create a output response surface, thus it is very time-consuming considering the high dimension of input space and high cost of CFD simulations. Therefore, local sensitivity analysis is used instead. Due to the limitation of sample size, it is difficult to directly use partial derivatives to facilitate the sensitivity analysis. Thus, one at a time (OAT) technique is applied in this sensitivity analysis. There are four input parameters, so the dimension of the input space is four. In the proposed OAT technique, the baseline training data is expanding by sampling one more grid point in one dimension (i.e. for one input parameter) each time. A data-driven model is built using the expanded training data set and the accuracy of the model is evaluated. This step is repeated for all four dimensions of the input, resulting in four data driven models. By ranking the accuracy of the four data-driven models, the order of importance of the four parameters is determined. Then the training data used for data-driven modeling is expanded by adding more samples in each dimension of the input space subsequently based on the order of parameter importance. The process is iterated until the desired accuracy is achieved. Specifically, after the upsampling is completed for all four dimensions, the resulting dataset becomes the new baseline training data in the next iteration and the sensitivity analysis is conducted again for the four input parameters in the new iteration. Then the baseline dataset is expanded subsequently based on the order of parameter importance. Although the proposed OAT technique cannot explicitly indicate the interference among input parameters, it can guide a best direction for efficient sampling in each iteration. The detailed procedure for updating sampling size of training data using OAT technique is performed with the following steps.

Step 1: Generate test dataset. Test dataset is needed for accessing the accuracy of data-driven models in sensitivity analysis and the upsampling process. The test data should be uniformly distributed over the entire range of the input space to ensure that the data are representative of the entire input space. Total of 16 data points (cases) are obtained from CFD simulations and the corresponding values of input parameters are shown in Table 4.3.

Step 2: Sample the baseline dataset for the 1st iteration and assess the prediction accuracy of the corresponding data-driven model. Two grid points for each dimension of the input space is used to generate samples for the initial baseline dataset. Specifically, the lower and upper bound of each input parameter are the sampling grid points, which results in 16 data points (cases) as shown in Table 4.3. The wind velocity of the 16 cases is simulated using CFD. The data are used to train a prediction model M^1 with cGANs. The accuracy of the model, measured by R^2, is evaluated using the test data generated in Step 1 (Table 4.3). A R^2 value close to 1 indicates the high accuracy of the model.

Step 3: Upsample the training data set in the 1st iteration. Samples are added in training data by subsequently increasing one grid point in one dimension each time. First, one grid point in the middle of the range is increased in h, which leads to a total of 24 data points with 8 of them newly added (Table 4.3). The updated training dataset is used to train a prediction model M_h^1, whose accuracy is also evaluated using the test data. Then this process of adding samples is conducted subsequently by adding one grid point in other dimensions each time, such as *dx*, *dy* and *dir*. Note that the order of increasing the grid point for different dimensions is not important in the first iteration since the number of samples is very small and the grid point will need to be added for all dimensions anyway. After new grid points are added for all dimensions, there are a total of 81 data points (cases) (Table 4.3).

Step 4: Conduct the sensitivity analysis for the i^{th} iteration to determine the order of parameter importance to facilitate upsampling in the $(i+1)^{th}$ iteration. Each time, one more sampling grid is added for one dimension (i.e., input parameter) while the number of sampling grids for other dimensions remains the same. For example, in the 1st iteration (Table 4.4), the number of grids for *h* increases from 2 to 3, while the number of grids for *dir*, *dx* and *dy* remains 2, resulting in 24 data points (cases). The 24 data points are used to train a prediction model M_h^{s1} with cGANs. The accuracy of the model is evaluated using the test dataset (from Step 1) and measured by the R^2 value in Table 4.4. The process is repeated for all four parameters. The order of parameter importance is obtained by ranking the R^2 value from high to low. As a note, although the data-driven model is proposed to predict 3D wind velocity fields, only the prediction model for the wind velocity at one height level is used in the sensitivity analysis. This is because the sensitivity analysis requires frequently generating prediction models with different training dataset and it is time-consuming for investigating the wind velocity contour at all the height levels.

Step 5: Upsample the training data set in the $(i+1)^{\text{th}}$ iteration. Samples are added in training data by subsequently increasing one grid point in one dimension each time. The order of increasing the grid point for different dimensions is based on the order of parameter importance determined in Step 4. After increasing one grid point for each dimension, a data-driven model is built, and the accuracy is evaluated using the test data and measured by R^2 value. If the R^2 value for the prediction model reaches a predefined threshold, the upsampling procedure can be stopped. For instance, in the 2^{nd} iteration, the importance of input parameters is ordered as, *dy*, *dx*, *dir*, and *h* based on R^2 value in Table 4.4. Firstly, the number of grid points for *dy* increases from 3 to 4, resulting in 108 data points and the model M_{dy}^{2}. The corresponding R^2 value is 0.9341 (Table 4.3), which is lower than the pre-defined threshold 0.94, thus the upsampling procedure continues by increasing number of grid points for *dx* next from 3 to 4, which leads to 144 training data points. However, the R^2 value of the corresponding model $M_{dy,dx}^{2}$ is 0.9277, which is lower than M_{dy}^{2}. This is caused by the uncertainty associated with the small size of test data. The upsampling procedure is still stopped even the threshold is not reached in this study due to the limitation of computing cost. The comparison of the prediction with model $M_{dy,dx}^{2}$ and the CFD simulated wind velocity field for one test case is shown in Fig. 4.9.

It should be noted that local sensitivity analysis is usually not considered to be valid for nonlinear systems since it can only provide information at the reference value where it is applied. In the proposed sampling strategy, the sensitivity analysis results at one reference value, e.g., the number of grid points for each parameter equals to 2, are only used to determine the sampling process at the adjacent value, e.g., the number of grid points for each parameter equals to 3. The sensitivity analysis was conducted for each sampling size at each iteration. Adding more sampling points at each iteration allows exploit the non-linearity at more local regions. This sensitivity analysis approach is similar to the Morris method (Morris, 1991), which facilitates a global sensitivity analysis by applying a number of local sensitivity analysis at different reference values in the input space.

Note that the proposed sampling strategy typically only requires a couple of iterations and small number of samples to achieve a high model accuracy, thus it is very efficient.

Table 4.3 Training dataset, test dataset and performance of prediction models in the sampling procedure

	Prediction model	Values of input parameter α (°)	hs (m)	dx (m)	dy (m)	Number of cases	R^2 Mean	Std	Cumulative computational time/ h
Training dataset in 1st iteration	M^1	-30 , 30	56,112	56,140	0,84	16	0.8883	0.0161	32
	M_h^1	-30 , 30	56,84,112	56,140	0,84	24	0.8898	0.0232	48
	$M_{h,dx}^1$	-30 , 30	56,84,112	56,98,140	0,84	36	0.9021	0.0304	72
	$M_{h,dx,dy}^1$	-30 , 30	56,84,112	56,98,140	0,42,84	54	0.9104	0.0313	108
	$M_{h,dx,dy,dir}^1$	-30 ,0, 30	56,84,112	56,98,140	0,42,84	81	0.9205	0.0281	162
Training dataset in 2nd iteration	M^2	-30 ,0, 30	56,84,112	56,98,140	0,42,84	81	0.9205	0.0281	162
	M_{dy}^2	-30 ,0, 30	56,84,112	56,98,140	0,21,42,84	108	0.9341	0.0183	216
	$M_{dy,dx}^2$	-30 ,0, 30	56,84,112	56,77,98,140	0,21,42,84	144	0.9277	0.0205	288
Test dataset	\	-18,18	67.2,100.8	72.8,123.2	16.8,67.2	16	\	\	\

Table 4.4 Training dataset, test dataset and performance of prediction models for sensitivity analysis

	Prediction model	Values of input parameter α (°)	hs (m)	dx (m)	dy (m)	Number of cases	R^2 Mean	Std
1st iteration	M_h^{s1}	-30 , 30	56,84,112	56,140	0,84	24	0.8898	0.0232
	M_{dx}^{s1}	-30 , 30	56,112	56,98,140	0,84	24	0.9161	0.0288
	M_{dy}^{s1}	-30 , 30	56,112	56,140	0,42,84	24	0.9174	0.0238
	M_{dir}^{s1}	-30 ,0, 30	56,112	56,140	0,84	24	0.9063	0.0233
Test dataset	\	-18,18	67.2,100.8	72.8,123.2	16.8,67.2	16	\	\

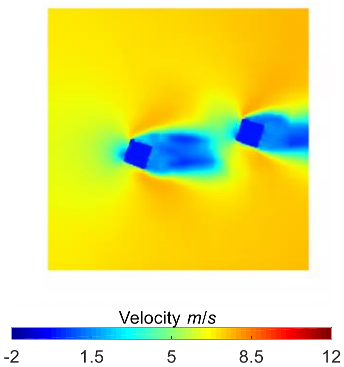

(a)

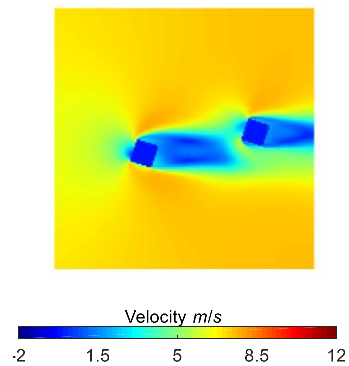

(b)

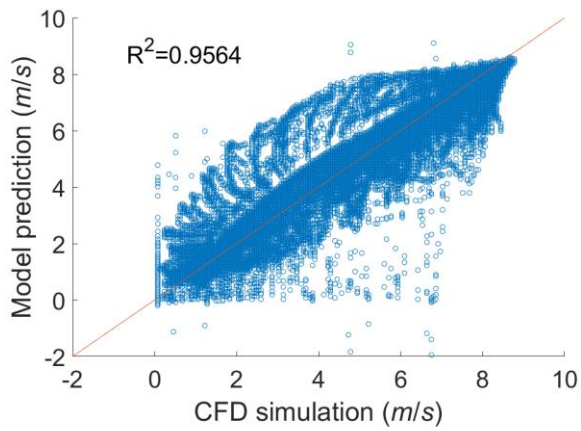

(c)

Figure 4.9 Comparison of the prediction result and the simulation result: (a) Model prediction (b) CFD simulation (c) Comparison of simulated and predicted data

4.6 Results

According to the aforementioned sampling strategy, a prediction model $M_{dy,dx}^{2}$ for the magnitude value of wind velocity at the height level equal to 0.6 is generated with the training dataset including 144 cases. As mentioned in the previous section, the 144 training data points and 16 test data points used for sensitivity analysis in Table 4.3 are combined to train the final data-driven model. The prediction models for the component of wind velocity at other height levels are trained in the same way. It should be noted that the investigated region and the composition of input images may differ for various prediction models for different heights. Since the aforementioned test data is part of the training data for final data-driven models, new test data for evaluating the accuracy the final data-driven models should be determined. Similar to the test data used in the sampling process, the test data for the final data-driven models should be representative of entire prediction range and the size of test data is determined considering the variability of wind velocity field. Considering the high cost of CFD simulation, the size of test data is set to 30. The mean prediction accuracy of the population of all possible realizations of the input parameters is evaluated using the point estimation obtained from the test dataset. Then, the margin of error for predicted wind fields is calculated via the following equation.

$$\varepsilon = \frac{z\sigma}{\sqrt{s}} \tag{4.2}$$

where z is the z-score for the desired confidence level, σ is the standard deviation of the prediction accuracy of wind velocity for test data, s is the size of test data and ε is the margin of error. In this study, the confidence level is set to be 90% and the corresponding z-score is 1.645. The four parameters associate with the building configuration and wind direction for the test data are obtained by randomly sampling from a uniform distribution in the prediction range. The values in the input space associated with the 30 test cases are listed in Table 4.5. The comparison between the simulated wind field and the predicted wind field for some final data-driven models in the testing process are shown in Figs 4.10 and 4.11. The prediction accuracy for all the data-driven models are listed in Table 4.6 and $M_{0.2}^{Um}$ represents the final prediction model for U_m at $z_n = 0.2$. It should be noted the vertical wind velocity component U_z is calculated using the predicted magnitude of wind velocity U_m and the horizontal components U_x and U_y instead of generating prediction models for U_z. Since the magnitude of wind velocity is important for assessment of wind damage, accurate prediction of U_m is necessary and building the data-driven prediction model for U_z is avoided for saving computing cost. Furthermore, avoiding the use of the data-driven prediction model of U_z saves 25% of storage space for the predicted wind velocity data, which is significant for a wind velocity field with a high spatial resolution.

The prediction accuracy for U_m and U_x is high, while the prediction accuracy for U_y is lower as shown in Table. 4.6. Since the proposed sampling strategery is conducted for U_m, the resulting samples may not be as efficient for U_y. Besides, the wind velocity data obtained from CFD simulations indicates that U_y has larger uncertainty than U_m, thus more training data is needed for the prediction of U_y to achieve the same accuracy as U_m and U_x. The prediction accuracy for U_y at $z_n = 1.2$, which represent for the vortex region over the rooftop of the source buildings, is relatively low compared to other heights. This is because the air flow pattern in the vortex region is much more complex than in the other regions. It is worthy to generate separate prediction models for the vortex region in future research, since the vortex region is critical for the debris generation on the rooftop of the source building.

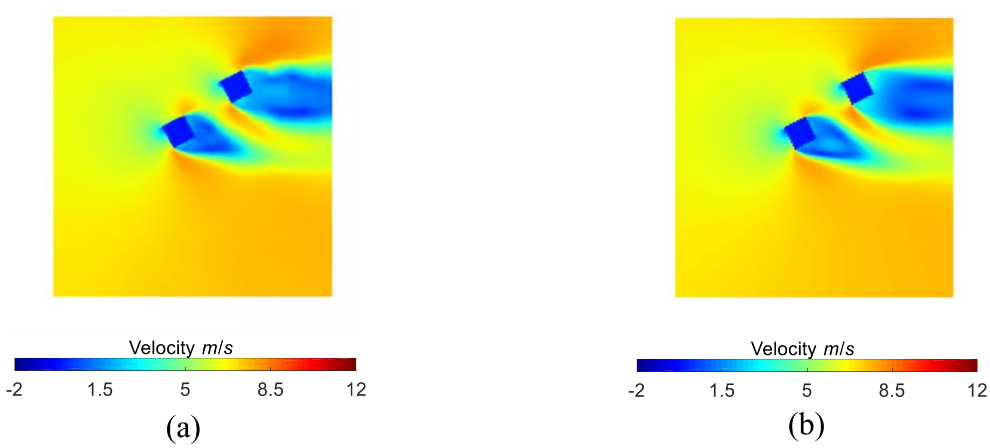

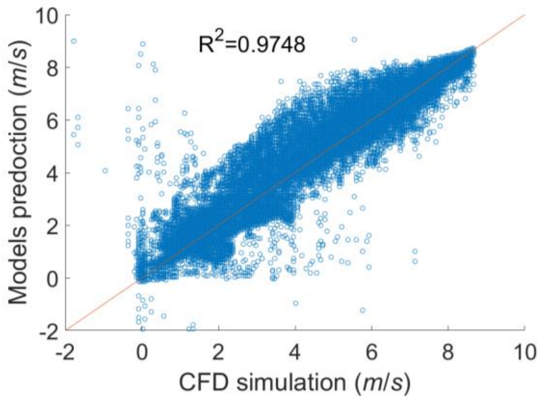

(c)

Figure 4.10 Comparison of the prediction results and the simulation results (U_m, $z_n = 0.6$): (a) Model prediction (b) CFD simulation (c) Comparison of simulated and predicted data

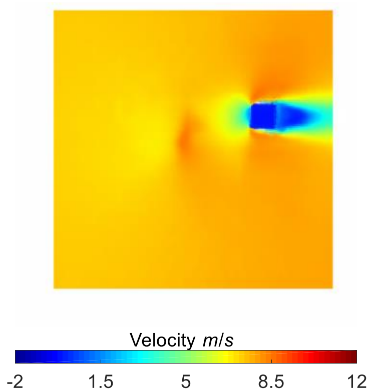

(a)

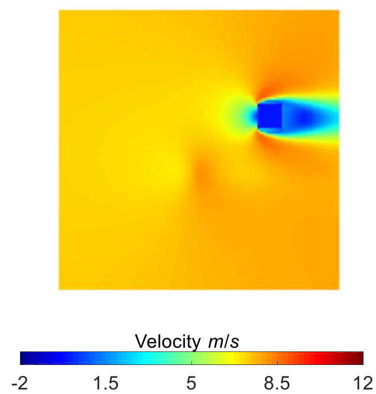

(b)

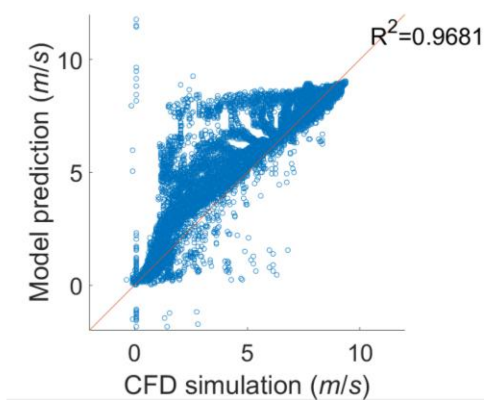

(c)

Figure 4.11 Comparison of the prediction results and the simulation results (U_m, $z_n = 1.4$): (a) Model prediction (b) CFD simulation (c) Comparison of simulated and predicted data

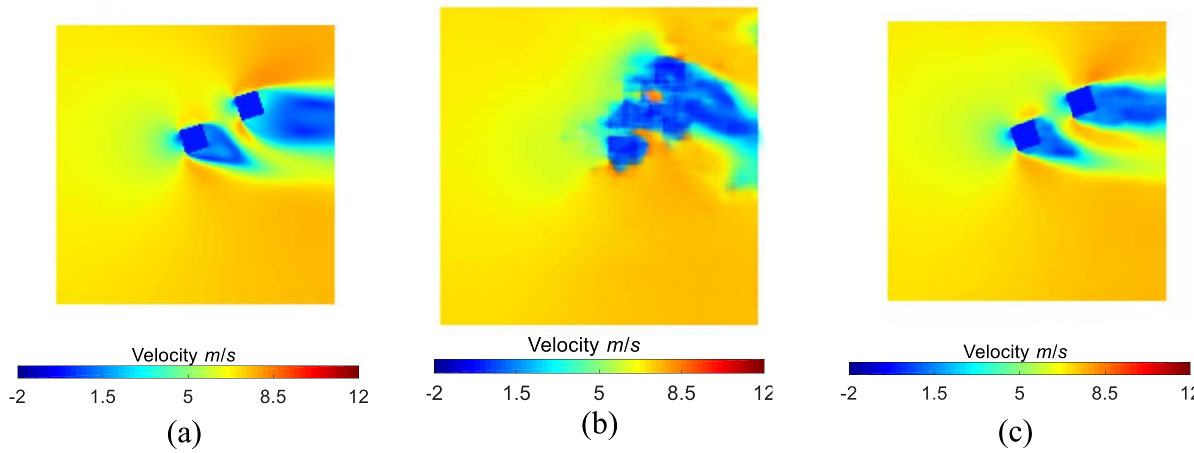

Figure 4.12 Comparison of the prediction results for two types of input images: (a) Ground truth (b) Prediction for input images with the projection of two buildings (c) Prediction for input images with the projection of one building

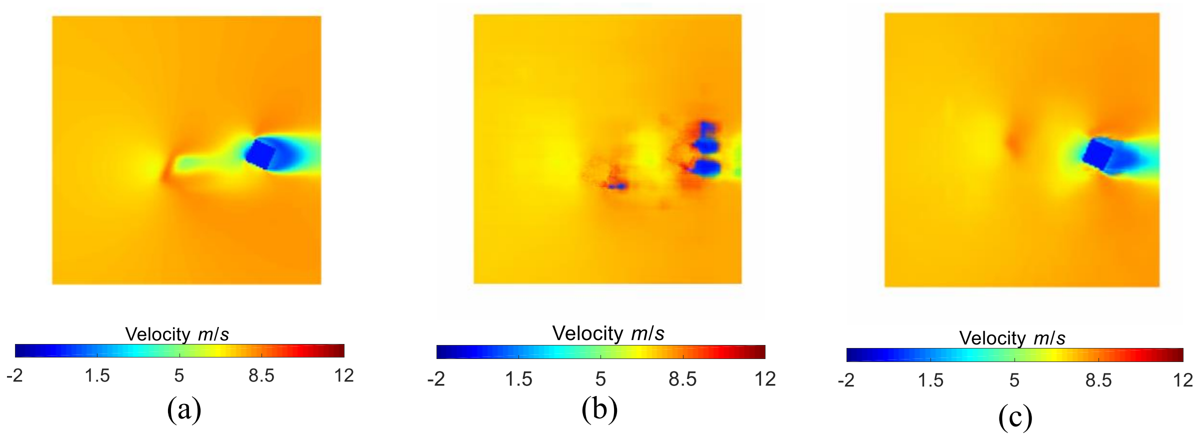

Figure 4.13 Comparison of the prediction results for two types of output images: (a) Ground truth (rotated) (b) Prediction with unrotated output images (c) Prediction with rotated output images

4.7 Discussions

The composition of the input and output images is critical for developing the cGANs models efficiently. As mentioned in Section 4.4, a new set of input images are constructed for the wind field between the rooftops of the two buildings to only include the projection of the target building. The height difference between the two buildings is used instead of the absolute height of the target building. Although relative height is used in the input images for wind field in this region, the information of absolute height, which determines the magnitude of wind velocity in Atmospheric Boundary Layer, is not lost since the height of the target building is fixed in this study. To investigate the improvement of the new set of input images for the wind field in this region (i.e. images with only the projection of the target building), additional prediction models are trained with the original input images which include the projection of two buildings. The comparison of prediction results between the data-driven models with the two types of input images are shown in Fig. 4.12. The performance of the prediction models with new input images is much better with the limited size of training data compared to the prediction accuracy with the input images including the projection of two buildings.

The output images are directly obtained from the wind velocity contour in CFD simulations. Rotating the entire building cluster instead of changing the inflow wind direction is a common approach for considering different wind directions in CFD simulations especially with a

Table 4.5 Values of the input parameters for test dataset

Test case	$dx\ (m)$	$dy\ (m)$	$hs\ (m)$	$\alpha\ (°)$	Test case	$dx\ (m)$	$dy\ (m)$	$hs\ (m)$	$\alpha\ (°)$
1	64.12	5.04	61.6	-15	16	73.36	59.08	104	-11
2	119.28	74.2	104.4	7	17	81.48	63.56	99.6	-25
3	106.4	21.84	100	-20	18	135.52	66.36	77.6	5
4	71.96	66.08	76.4	-1	19	66.36	4.76	94	12
5	133.28	83.44	59.2	-27	20	115.64	66.64	73.2	2
6	115.36	38.92	59.2	11	21	118.72	40.04	74.8	-6
7	82.6	15.68	100	27	22	87.08	39.2	103.2	13
8	94.36	29.12	85.6	-27	23	85.68	42	78	-8
9	133.84	45.92	66	-20	24	81.48	31.36	80.8	-1
10	64.68	9.52	70.8	11	25	130.76	17.08	87.2	-29
11	117.04	14	110.4	12	26	129.36	78.68	79.6	19
12	136.08	66.08	74.4	-3	27	102.76	33.6	96.4	-7
13	61.6	81.48	71.6	23	28	125.44	22.68	81.6	-30
14	116.76	22.96	110	-1	29	78.4	30.8	100	-22
15	99.68	83.44	69.2	26	30	66.36	41.72	65.6	21

Table 4.6 Prediction error for U_m, U_x and U_y

Velocity component	Prediction model	R^2 Mean	R^2 Std	R^2 Margin of error	Prediction model	R^2 Mean	R^2 Std	R^2 Margin of error
U_m	$M_{0.2}^{U_m}$	0.8844	0.0443	0.0133	$M_{1.2}^{U_m}$	0.9161	0.0461	0.0139
	$M_{0.4}^{U_m}$	0.9192	0.0386	0.0116	$M_{1.4}^{U_m}$	0.9365	0.0423	0.0127
	$M_{0.6}^{U_m}$	0.9404	0.0307	0.0092	$M_{1.6}^{U_m}$	0.9454	0.0405	0.0122
	$M_{0.8}^{U_m}$	0.9553	0.0231	0.0070	$M_{1.8}^{U_m}$	0.9545	0.0346	0.0104
	$M_{1}^{U_m}$	0.9294	0.0333	0.0100	$M_{2}^{U_m}$	0.9516	0.0280	0.0084
U_x	$M_{0.2}^{U_x}$	0.9117	0.0410	0.0123	$M_{1.2}^{U_x}$	0.9024	0.0499	0.0150
	$M_{0.4}^{U_x}$	0.9286	0.0343	0.0103	$M_{1.4}^{U_x}$	0.9258	0.0497	0.0149
	$M_{0.6}^{U_x}$	0.9343	0.0400	0.0120	$M_{1.6}^{U_x}$	0.9334	0.0473	0.0142
	$M_{0.8}^{U_x}$	0.9576	0.0264	0.0079	$M_{1.8}^{U_x}$	0.9487	0.0379	0.0114
	$M_{1}^{U_x}$	0.9342	0.0313	0.0094	$M_{2}^{U_x}$	0.9516	0.0326	0.0098
U_y	$M_{0.2}^{U_y}$	0.8264	0.1153	0.0346	$M_{1.2}^{U_y}$	0.5199	0.3024	0.0908
	$M_{0.4}^{U_y}$	0.8610	0.1037	0.0312	$M_{1.4}^{U_y}$	0.5849	0.3102	0.0932
	$M_{0.6}^{U_y}$	0.7858	0.0818	0.0246	$M_{1.6}^{U_y}$	0.6681	0.2033	0.0611
	$M_{0.8}^{U_y}$	0.8643	0.0805	0.0242	$M_{1.8}^{U_y}$	0.6303	0.2317	0.0696
	$M_{1}^{U_y}$	0.8156	0.0791	0.0238	$M_{2}^{U_y}$	0.5656	0.1808	0.0543

triangular computation domain. Thus, the wind velocity contour obtained from CFD simulations is rotated. In this study, the rotated wind velocity contour is used as the output images in the data-driven model considering the consistency of the input images and output images, which is critical to train cGANs model efficiently. It should be noted that the predicted wind velocity components U_x, U_y, and U_z are calculated based on the rotated coordinate system in CFD simulations and the wind velocity component should be transformed to local coordinate system for evaluating the flight trajectory of debris. Besides, the studied region of wind velocity field slightly varies with different inflow wind directions. Thus, the studied region of wind velocity field should be sufficiently large to include all necessary wind velocity data for debris damage assessment. Using the unrotated wind velocity as the output images is also an option for training prediction models. In this way, the boundaries of all the studied region are the same and no coordinate transformation is needed in simulating debris trajectory. The prediction results of wind velocity field with these two types of output images are shown in Fig. 4.13. The prediction results with the unrotated wind field are much worse compared to the results with rotated input images, suggesting that the rotating input images is necessary.

4.8 Concluding remarks

In this study, prediction models for 3D wind field over urban building clusters are proposed. The building cluster investigated is composed of one source building and one target building in the context of debris damage assessment. The predicted wind field can be readily used in simulating the trajectory of debris generated from the source building. These prediction models can also be used in the risk assessment and resilience planning of urban communities under hurricanes. The proposed machine learning based prediction model can provide refined wind conditions at the local scale and allow quick estimation of damage for a significant amount of hurricane scenarios which is common in resilience planning of urban communities. The following conclusions are drawn:

- Both the configuration of buildings and inflow wind conditions are taken into consideration as input parameters for predicting urban wind field with arbitrary building configurations and inflow wind conditions. Considering the complexity of the aerodynamic interference between the high-rise buildings and surroundings, as a start, the number of buildings investigated in this study is limited to two and the future works will focus on increasing the number of buildings in the prediction models.
- The data-driven prediction models are generated using cGANs models. The training dataset

is obtained from RANS models and the wind tunnel test data from TPU dataset are used to validate the numerical simulations. The comparison results between CFD simulation and model prediction indicate a high accuracy of predicting urban wind field using cGANs models with a limited training dataset.

- Sensitivity analysis is applied for determining the sampling strategy of training dataset considering the high cost of CFD simulations. The influence of input parameters on the accuracy of prediction models with the increased size of training dataset is investigated with the OAT technique. This sampling strategy can indicate an efficient direction for increasing the size of training dataset and improve the performance of the prediction models with limited training dataset.
- The performance of cGANs models is greatly affected by the composition of the input images and the output images. The prediction results in this study indicate that the similarity between the input images and the output images should be taken into account for improving the performance of cGANs model. The overfitting issue induced by the small size of dataset is alleviated by guaranteeing the consistency of the number and the rotation angle of building projections in the input and output images to reduce the model complexity.

CHAPTER 5 UNCERTAINTY ANALYSIS AND PROPAGATION FOR WINDBORNE DEBRIS DAMAGE ASSESSMENT

In previous Chapters, the subsystems of hurricane simulation, modeling debris induced damage and predicting urban wind velocity field are discussed. The risk of debris induced damage under hurricane hazards can be estimated through integration of these subsystems. The whole procedure of risk assessment is quite complicated and involves several models and a number of parameters. Therefore, determining the uncertainties in each subsystem and propagating the uncertainties among these subsystems are critical. Furthermore, some assumptions are used in this study to simplify the procedure of debris damage assessment considering the high computation cost and the complexity of systems. For example, the process of downscaling hurricane wind speed from the gradient level to the local building cluster level is simplified using a boundary layer model. It is important to understand the impact of these simplifications on accuracy of the debris damage risk assessment. Thus, sensitivity analysis is conducted to evaluate the importance of each subsystem in damage assessment. This sensitivity analysis can provide insights into the directions of further study aimed at reducing the uncertainty.

5.1 Uncertainty sources in windborne debris damage assessment

In previous Chapters, some of the uncertainties in the risk assessment of debris induced damage are briefly discussed. In this subsection, a comprehensive analysis of uncertainty sources in each subsystem is identified to facility the further uncertainty quantification and propagation in the following subsections.

Typically, uncertainties can be classified into two types. One is aleatoric uncertainty, while the other is epistemic uncertainty. Aleatoric uncertainty represents the inherent randomness in the data, and it cannot be reduced by improving models with more data. Noise in the measured data is a typical source of aleatoric uncertainty. Epistemic uncertainty is induced by the lack of knowledge or understanding about the underlying physics or the lack of data. The epistemic uncertainty often can be reduced by obtaining more data. Aleatoric uncertainty and epistemic uncertainty are usually not independent; in contrast, these two types of uncertainties often occur simultaneously for a model or parameter. Furthermore, aleatoric uncertainty and epistemic uncertainty for a model or a parameter sometime are fully coupled and cannot be easily distinguished in practice. For instance, the noise in the measurement data can be induced by the inherent uncertainty in data (aleatoric) and inaccurate measurement (epistemic).

5.1.1 Uncertainty sources in subsystem of hurricane simulation

In Chapter 2, synthetic hurricane scenarios are simulated with statistical models (Vickery et.al., 2000a) obtained based on historical hurricane data. The hurricane wind velocity (and direction) fields are then simulated for each synthetic hurricane scenario during the passage of the hurricane determined by the hurricane wind field model and the hurricane track model. Accordingly, the uncertainties in the wind direction and velocity at a site stem from the uncertainties of wind velocity field model and hurricane track model. Thus, the uncertainties of wind velocity field model and hurricane track model for a scenario hurricane are discussed in the following.

Uncertainties associated with hurricane track model: The pressure deficit Δp is modeled following Eq. 2.2 and the constant coefficients $c_0,\ldots,c_5$ in the equation are determined through regression models for historical data. The uncertainty in the constant coefficients is classified as epistemic uncertainty. Similarly, the uncertainties in the translation speed s and the translation direction (heading angle) θ are also classified as epistemic uncertainty.

Uncertainties associated with hurricane wind field model: Based on Eqs. 2.5 and 2.6, the uncertainties in the regression parameters for modeling the radius of maximum wind velocity *RMW*, the Holland's pressure profile parameter B, are also classified as epistemic uncertainty. Besides, the inherent aleatoric uncertainties of these parameters in both track and hurricane models also exist due to the stochastic behavior of natural hazard.

Sampling error of return period hurricane wind speed: In this study, the ensemble of hurricane scenarios corresponding to a stipulated return period hurricane wind speed are investigated. Thus, the sampling error in the return period hurricane wind speed are also involved in the final debris damage assessment.

5.1.2 Uncertainty sources in subsystem of modeling debris induced damage

In Chapter 3, the generation, transportation and impact mechanism of windborne debris are investigated for risk assessment. Epistemic uncertainties are associated with the models of debris generation, transport and impact. Besides, there are also epistemic uncertainties in the empirical reduced-order model of the time-varying mean wind speed and the surrogate model of debris trajectory. Aleatoric uncertainties stem from the stochastic behavior of debris generation rate, turbulence component in the inflow wind, debris size and the resistance of window panels.

5.1.3 Uncertainty sources in subsystem of predicting urban wind velocity

In Chapter 4, data-driven prediction models for urban wind field are proposed using the cGANs machine learning. Epistemic uncertainty is involved in both CFD simulations and the machine learning models.

5.2 Uncertainty quantification and propagation

5.2.1 Quantification of uncertainties in subsystem of hurricane simulation

According to the limitations of computational power and lack of data, only some critical uncertainties are quantified in this Chapter. Vickery (2009) conducted a comprehensive study about the uncertainty in U.S. hurricane wind speed, similar approaches are adopted to quantify the uncertainty in this section. It should be noted that only the hurricane scenarios with a stipulated return period and the minimum distance between the hurricane center and the centroid of the community less than 250 *km* are investigated. Moreover, most of the uncertainties in the studied hurricane wind velocity originate from the uncertainty in hurricane intensity (Vickery 2009). Therefore, this section focuses on quantifying uncertainties associated with the hurricane intensity, while the uncertainties in hurricane track and annual frequency of occurrence are not investigated. In this case, only a synthetic hurricane scenario with a stipulated return period and fixed track is used for uncertainty quantification instead of running the procedure of simulating hurricane tracks in 200,000 years for many times. The uncertainties of Δp, B and *RMW* are considered by adding an error term with zero mean value as shown in Eqs. 2.2, 2.5 and 2.6. Besides, the uncertainty in translation speed which is less important is considered by adding a multiplicative wind speed error term with unity mean value and coefficient of variation (CoV) equal to 0.02 (Vickery 2009). Similarly, the epistemic uncertainty of the hurricane wind velocity model is quantified by adding a multiplicative wind speed error term with unity mean value and CoV equal to 0.1 based on the comparison of simulated and observed wind speed data (Vickery 2009).

The sampling error for a stipulated return period hurricane wind speed originates from the sampling error for hurricane pressure deficit. In this Chapter, the City of Miami, FL is used as an example for uncertainty quantification and propagation in the simulation of hurricane scenarios. The historical hurricane landfall pressure deficit in the City of Miami, FL is assumed to follow a Type I (Gumbel) distribution (Vickery 2009) to evaluate the sampling error. The two parameters of Gumbel distribution are estimated using the method of moments with the following equations:

$$\beta = \sqrt{{\sigma_x}^2 \frac{6}{\pi^2}} \tag{5.1}$$

$$\mu = \bar{x} - \beta\gamma \tag{5.2}$$

$$F_X(x) = e^{-e^{-(x-\mu)/\beta}} \tag{5.3}$$

where $\bar{x}$ is the estimated expectation of x, σ_x is the estimated standard deviation of x, μ is the estimated location parameter, β is the estimated scale parameter and γ is the Euler-Mascheroni constant equal to 0.5772.

The estimated standard deviation of sampling error for *N*-yr return period with the method of moments is calculated using the following equations (Simiu et al. 1979):

$$\sigma_x(1-\frac{1}{N\cdot FS}) = \sqrt{\left[\frac{\pi^2}{6} + \frac{1.1396(y-0.5772)}{\sqrt{6}} + 1.1(y-0.5772)^2\right]}\frac{\beta}{\sqrt{n}} \tag{5.4}$$

$$y = -\ln\left(-\ln\left(1-\frac{1}{N\cdot FS}\right)\right) \tag{5.5}$$

where *FS* is the annual frequency of occurrence, $\sigma_x(1-\frac{1}{N\cdot FS})$ is the estimated standard deviation of sampling error for *N*-yr return period and *n* is sample size.

There are several approaches for unbiased estimation of the location and scale parameters, e.g., probability plots and maximum likelihood estimation. The standard deviation of sampling error varies with different estimation approaches. The low bound of the estimated sample error, which is referred to Cramer-Rao lower bound is calculated by the following equation:

$$\sigma_x^{CR}(1-\frac{1}{N\cdot FS}) = \sqrt{\left(0.60793y^2 + 0.514y + 1.10866\right)}\frac{\beta}{\sqrt{n}} \tag{5.6}$$

Totally 42 hurricanes with all categories from 1842 to 2022 with minimum distance between hurricane center and the centroid of Miami less than 250 *km* according to the National Oceanic and Atmospheric Administration (NOAA) Hurricane Track Tool are used for the analysis (NOAA, 2020). The annual frequency of occurrence for all category hurricane is 0.2333; the estimated expectation of landfall pressure deficit is 54.0595 *hPa*; the estimated standard deviation of landfall pressure deficit is 21.1513 *hPa*; the estimated location parameter and scale parameter are 44.5406 *hPa*, 16.4916 *hPa*, respectively; the estimated standard deviation of sampling error using the method of moments and the low bound are 10.8316 *hPa* and 9.5975 *hPa*, respectively. Here 300-yr return period hurricane wind is used as an example to illustrate the quantification of sampling error. Specifically, the estimated landfall pressure for 300-yr return period hurricane is 114.4866 *hPa*. Thus, one hurricane scenario simulated in Chapter 2 with landfall pressure deficit close to 114.4866 *hPa* is selected for uncertainty analysis. The landfall pressure deficit and corresponding radius of maximum wind speed and parameter *B* are 118.5143 *hPa*, 19.9684 *km* and 1.5359 respectively, which are assumed to be the reference values. The sampling error is considered by adding an error term $\kappa\sigma_x(1-\frac{1}{N\cdot FS})$, where κ is a random variable following normal distribution with zero mean and standard deviation of 1. The uncertainty of wind velocity can be calculated through uncertainty propagation from the aforementioned parameters (Δp, B and *RMW*) using Monte Carlo approaches. The estimated mean CoV of maximum hurricane velocity at landfall on gradient level for the selected hurricane scenario with the stipulated return period (300-yr in this example) is about 0.18.

5.2.2 Quantification of uncertainties in subsystem of modeling debris induced damage

Epistemic uncertainties associated with physics-based debris damage model: The epistemic uncertainty associated with the models involved in the process of debris generation, transport and impact, e.g., the debris trajectory model based on Newton's Second Law, is not considered due to the lack of knowledge or data.

Aleatoric uncertainties associated with stochastic nature of the physics: The debris generation process is modeled as a Poisson process and the corresponding aleatoric uncertainty can be quantified via random sampling of the stochastic process. A similar quantification approach is applied for the fluctuating component of inflow wind velocity, which is also treated as a stochastic process with von Karman turbulence spectrum. The size of debris is assumed to follow a normal distribution, while the resistance of window panels is assumed to follow a lognormal distribution. Consequently, the corresponding aleatoric uncertainties are explicitly quantified.

Uncertainties associated with reduced order hurricane wind speed model: The uncertainty in reduced-order model is investigated by comparing the modeled time varying wind velocity profile with the wind speed at the centroid of Miami under the simulated hurricane events. As mentioned in Chapter 3, there are two types of time varying wind velocity profile; one has only one peak and the other has two peaks. The mean RMSE error between the modeled wind speed and the simulated wind speed with one peak is 7.05 *m*/*s*, while the mean RMSE error for wind speed with two peaks is 16.02 *m*/*s*. Besides, the overall mean RMSE error for wind speed are 11.45 *m*/*s*. Therefore, the uncertainty in the reduced-order model is quantified by adding an error term ε_m to the modeled wind speed, where ε_m follows normal distribution with zero mean and standard deviation equal to 11.45 *m*/*s*.

Uncertainties associated with the surrogate model for simulating the debris trajectory: As mentioned in Chapter 3, kriging approaches are utilized to build a surrogate model for simulating the debris trajectory. The kriging approximation is generated using a MATLAB toolbox DACE (Design and Analysis of Computer Experiments) (Lophaven et.al., 2002). The kriging approach provides estimation of the prediction error based on spatial correlation between sampling data and the selected regression model, which quantifies the aleatoric and epistemic uncertainties in the surrogate model. The mean standard deviation of the impact location and velocity for the selected example hurricane scenario are around 5.2 *m* and 2.4 *m*/*s*. Therefore, the uncertainty in the surrogate model is quantified by adding an error term ε_{loc} to the predicted impact location and another error term ε_{vel} to the predicted impact velocity , where ε_{loc} follows normal distribution with zero mean and standard deviation equal to 5.2 *m*, and ε_{vel} follows normal distribution with zero mean and standard deviation equal to 2.4 *m*/*s*.

5.2.3 Quantification of uncertainties in subsystem of predicting urban wind velocity

The epistemic uncertainty in the CFD wind velocity simulations is not considered due to the high cost of repeating CFD simulations and the lack of measurement data of urban wind field, while the epistemic uncertainty associated with the cGANs model is quantified using Monte Carlo (MC) dropout approach (Gal and Ghahramani, 2016). Dropout is a regularization method used in the training to avoid overfitting through randomly drop units from the neural network. In MC dropout, dropout is also used during the testing time. In this case, many different neural networks are treated as Monte Carlo samples from the space of all possible cGANs models. Thus, MC dropout can offer an approximation for uncertainties in the prediction results. The estimated mean CoV for the predicted wind field data with the input space in Chapter 4 is around 0.05 using MC dropout.

5.2.4 Propagation of uncertainties among sub-systems

MC approaches are not directly used in the whole procedure of debris damage assessment due to extremely high computational cost. Instead, the MC approaches are utilized for uncertainty propagation in each subsystem subsequently. In the subsystem of hurricane simulation, the uncertainty in the inflow wind velocity is quantified through uncertainty propagation. Meanwhile, the uncertainty in the local wind velocity field is also quantified through uncertainty propagation in the subsystem of predicting local urban wind velocity. Then, MC approaches involving only the inflow wind velocity, local wind velocity field and parameter in the subsystem of modeling debris induced damage are applied to quantify the uncertainty in debris damage. In this case, much less parameters are included in the MC approaches, which is more efficient comparing with directly applying MC approaches on all the parameters involved in all three subsystems simultaneously. The CoV of the parameter studied in this uncertainty analysis and the final results of debris induced damage (represented by the ratio of damaged window on the building envelop with the example hurricane scenario and building cluster) are listed in Table 5.1.

Table 5.1 The CoV of factors and the debris induced damage

Factors	CoV	Factors	CoV
Pressure deficit	0.202	Reduced-order wind velocity model	0.176
Holland Parameter B	0.15	Surrogate model for debris trajectory	0.178
RMW	0.413	Tine interval between generation of successive debris	0.007
Translation speed	0.02	Debris size	0.458
Holland wind velocity model	0.1	Resistance of window panel	0.206
Inflow wind velocity	0.183*	Debris induced damage	0.422*
Prediction model of local wind field	0.05*		

Note: * represents uncertainty in the output of each subsystem after uncertainty propagation

5.3 Sensitivity analysis of critical factors

A sensitivity study is conducted to identify the critical factors in the debris risk assessment, which can help identify future directions of research effort. For example, if the debris damage is found to be sensitive to a certain factor, then improving the modeling in this aspect in the future is critical. As mentioned before, the whole procedure of risk assessment is composed of three subsystems. The central piece of the risk assessment is subsystem for modeling debris induced damage, while the subsystem for simulating scenario hurricanes provides the inflow wind profile and the subsystem for predicting urban wind field provides the local urban wind velocity field around building clusters, which drives the movement of debris. The importance of the latter two subsystems is investigated by studying the sensitivity of the debris damage to the change of inflow wind speed and local wind velocity field. Within the subsystem for modeling debris induced damage, the importance of debris generation modeling is studied via a sensitivity study, because we have the least knowledge on the debris generation mechanism on the roof top. In this case, the arrival rate of Poisson process is the parameter of the sensitivity study. In summary, *three critical factors* are considered in the sensitivity study, i.e. inflow wind speed, local wind velocity field and the arrival rate of Poisson process. The one at a time (OAT) technique is used in the sensitivity analysis. The baseline for the aforementioned three critical factors is the reference value used in the uncertainty analysis. Each time, one critical factor is modified by 5%, while the other two factors are kept unchanged. Meanwhile, MC approaches are applied to propagate uncertainties of other sources, e.g. the turbulence of inflow wind speed. The changes in the ratio of damaged window induced by 5% changes in inflow wind speed, the local wind velocity field and arrival rate of Poisson process are around 10.1%, 3.9% and 8.4%, respectively. As mentioned in Chapter 4, the inflow wind speed is considered as a scaling factor for the predicted local wind velocity field. Thus, the change in the inflow wind speed can cause same magnitude of changes in the local wind field. However, changes in the inflow wind speed also affects the flow structure of vortices on the rooftop, which explains why the debris induced damage is more sensitive to the inflow wind profile than the local urban wind field.

Since the aforementioned sensitivity study revealed that the debris damage is most sensitive to the inflow wind speed, it is worthwhile to investigate importance of the critical factors in the subsystem for hurricane simulation, including Δp, B and *RMW.* Similarly, these three factors are also modified by 5% each time using the OAT technique. The changes in the wind velocity corresponding to Δp can be estimated using the following regression model proposed by Vickery (2009):

$$\frac{\Delta V_3}{V_3} = 1.049\left[\sqrt{1+\frac{\Delta(\Delta p)}{\Delta p}} - 1\right] \tag{5.7}$$

The changes in the wind velocity due to the changes to B and *RMW* can be estimated using the following partial derivatives with the reference value of B and *RMW*:

$$V_G(r) = \left\{ \left(\frac{RMW}{r}\right)^B \frac{B\Delta p \exp\left[-\left(\frac{RMW}{r}\right)^B\right]}{\rho} \right\}^{1/2} \tag{5.8}$$

$$\Delta V_3 \approx \frac{\partial V_G}{\partial B}\Delta B \frac{1}{fa} \tag{5.9}$$

$$\Delta V_3 \approx \frac{\partial V_G}{\partial RMW}\Delta RMW \frac{1}{fa} \tag{5.10}$$

where V_3 is the 3-sec gust wind speed, V_G is the gradient wind speed, r is distance between the hurricane center and centroid of Miami, ρ is the air density, fa is a conversion factor from the gradient wind speed to the 3-sec gust wind speed. The reference value of r corresponding to the maximum wind velocity at the centroid of Miami is around 19 km. Thus, the changes in the maximum wind speed induced by the 5% changes in Δp, B and *RMW* are round 2.6%, 2.5%, 0.3%, respectively. Therefore, Δp, B are much more important than *RMW* for simulating the inflow wind speed.

The sensitivity analysis shows that the debris damage risk assessment is sensitive to inflow wind condition. It should also be noted that the downscaling process of hurricane wind speed from mesoscale to microscale is involved in the subsystems of hurricane simulation and predicting urban wind velocity. The boundary layer wind model is employed to consider the suburban exposure. However, the influence of specific surrounding built environment on wind field around a local building cluster is not detailed modeled. This simplified downscaling process may induce large uncertainties in simulating inflow wind conditions, thus amplifying the uncertainty in assessing debris damage for complex real urban communities. Thus, improving downscaling process is an important future research direction.

5.4 Conclusions

A comprehensive discussion about the uncertainty involved in the procedure of evaluating the risk of windborne debris is presented in this Chapter. The uncertainty in the assessment of windborne debris induced damage is estimated through the uncertainty quantification of factors involved in the three subsystems, and uncertainty propagation both in each subsystem and between the subsystems. Due to the lack of knowledge or data, only part of the uncertainties discussed Section 5.1 are quantified, and this may induce underestimation of the uncertainty in debris risk. For example, the uncertainties associated with the CFD models and the physics-based debris trajectory model are not considered. Future studies may be needed to quantify these uncertainties, which requires the collection of wind field data and debris trajectory data for urban building clusters. Large uncertainty (CoV=0.42) is seen in the debris damage risk, which is expected considering the complexity of the whole procedure for damage assessment. Thus, further study about reducing the uncertainty is necessary for improving the risk assessment model. To facilitate the identification of future direction of research efforts towards reducing the uncertainty, sensitivity studies are also conducted. It is found that the accurate estimation of inflow wind speed including the simulation of hurricanes and the downscaling from mesoscale to microscale is a critical direction for further study.

CHAPTER 6 ASSESSMENT OF DEBRIS DAMAGE OVER AN URBAN COMMUNITY

To illustrate the damage assessment procedure of windborne debris on community level, the debris induced damage on building envelopes in an urban community under hurricanes are investigated. A virtual urban community with several building clusters that are vulnerable to windborne debris is studied instead of a real urban community in this Chapter since the proposed prediction model of urban wind field can only deal with simple building clusters at present. The virtual urban community is designed based on Miami city.

6.1 Assumption of building clusters and hurricane scenarios

Building clusters used in the virtual urban community are assumed to be similar to the building clusters studied in prediction model of urban wind field, which includes one source building and one target building. The baseline configuration of the building cluster is shown in Fig. 6.1. The size of the source building is $28m \times 28m \times 84m$; the size of the target building is $28m \times 28m \times 112m$; the horizontal and vertical distance between the centroid of the two buildings are 0 *m* and 61.6 *m*, respectively. The building clusters in the virtual community are designed with two purposes: (1) to investigate the influence of the spatial distribution of hurricane wind velocity field on the debris induced damage in building clusters located at different locations; and (2) to investigate the uncertainty of debris induced damage in building clusters with different building configurations (orientations) under the same hurricane scenario. For the first purpose, three building clusters with the same building configuration are placed in the northern corner, centroid and southern corner of the community as shown in Fig. 6.2. The size of building clusters is amplified in the map for visualization. For the second purpose, three cases of virtual community are studied. The three building clusters are designed by rotating the baseline of building clusters by 0 degree (case 1), 15 degree (case 2) and -15 degree (case 3) for the three cases as shown in Figs. 6.2 to 6.4.

Hurricane events corresponding to the 700-yr return period of wind speed at centroid at Miami are simulated in Chapter 2 and these hurricane events are also used for investigating the debris induced damage in the virtual urban community. These hurricane scenarios are de-aggregated with the same parameters as in Chapter 3 and the 18 hurricane scenarios under the top highest probability mass in Fig. 2.2(a), which represent the dominant contributors to the 700-yr event, are selected to investigate the uncertainty in the debris damage assessment at a community level.

6.2 Fragilities for damage assessment

The fragilities for the debris induced damage in the building clusters are generated following the approaches described in Chapter 3. It should be noted that the local wind velocity field around buildings is calculated using the predicted model in Chapter 4. The predicted wind velocity field is scaled according to magnitude of the time varying inflow wind velocity as mentioned in Chapter 4. Besides, the wind velocity field for inflow wind direction is in the range of -30° to 30° and predicted with an interval of 1°. The inflow wind direction out of this range is assumed to cause no debris induced damage according to prior research of the range of inflow wind direction with potential risk of debris damage on the studied building clusters in Chapter 3. The wind velocity fields for arbitrary inflow wind directions between the 1° grid points are predicted through linear interpolation of the pre-predicted wind velocity data without running the data-driven prediction model, which can save 99% of computational time by avoiding the image processing in the data-driven model. Only the fragilities for one building configuration are required, since the building clusters in the virtual community are designed by rotating the baseline configuration of building cluster which is equivalent to changing the inflow wind direction. The range of the input parameters, including the maximum inflow wind speed $V_{\max}$, the inflow wind direction $\theta_{\max}$

corresponding to $V_{\max}$ and the duration of hurricane events ΔT, are based on the selected 700-yr hurricane events. The fragilities for this building cluster are developed for $V_{\max} \in [64, 80]\, m/s$, $\theta_{\max} \in [-60°, 60°]$ and $\Delta T \in [4, 14]\, h$. Similar to the construction of fragilities in Chapter 4, both the component level and building level fragilities for the building cluster are modeled. The size of window panel on the target building envelope is $1\, m \times 1\, m$ and the number of windows is $84 \times 28 = 2352$. Five windows located in the center and four corners of the front wall, as shown in Fig. 6.5, are selected for constructing component level fragilities and the building level fragilities are constructed based on the classification of damage state shown in Table 3.2 in Chapter 3. Since most 700-yr hurricane events can induce debris damage exceeding damage state 3, only the probability of exceeding damage state 4 is investigated in this Chapter. As mentioned in Chapter 3, fragility surfaces on component level and building level as a function of two intensity measures are shown in Figs. 6.6 to 6.11 with the third intensity measure fixed for visualizing the three-dimensional fragilities.

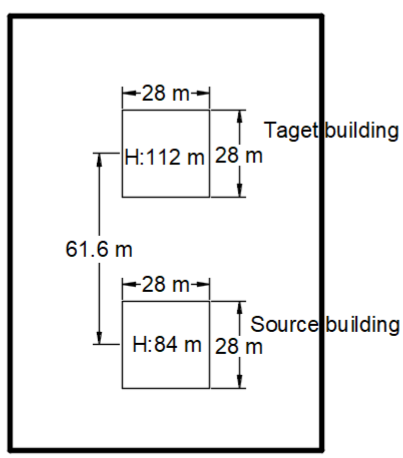

Figure 6.1 Baseline configuration of the building cluster

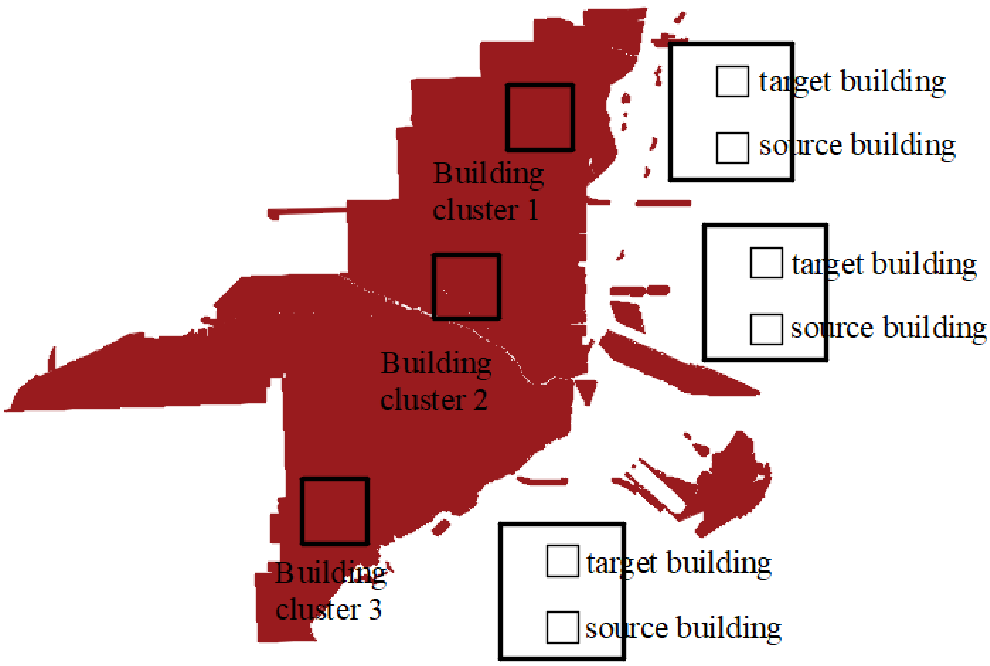

Figure 6.2 Building clusters in the virtual community (case 1)

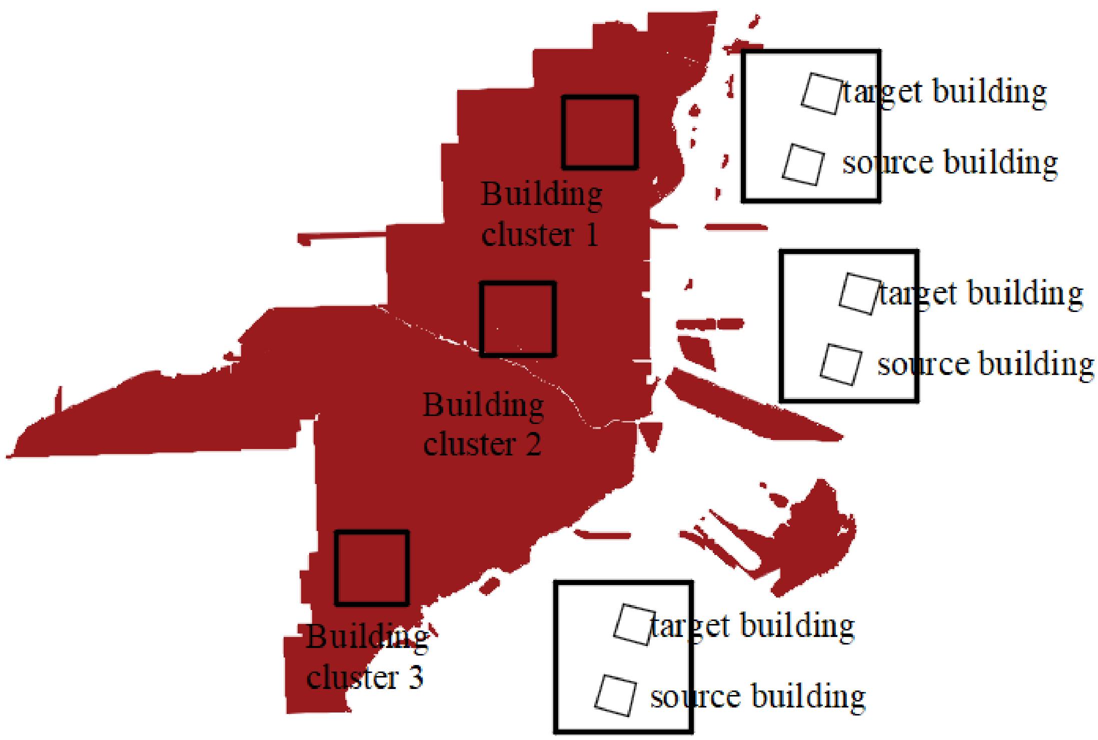

Figure 6.3 Building clusters in the virtual community (case 2)

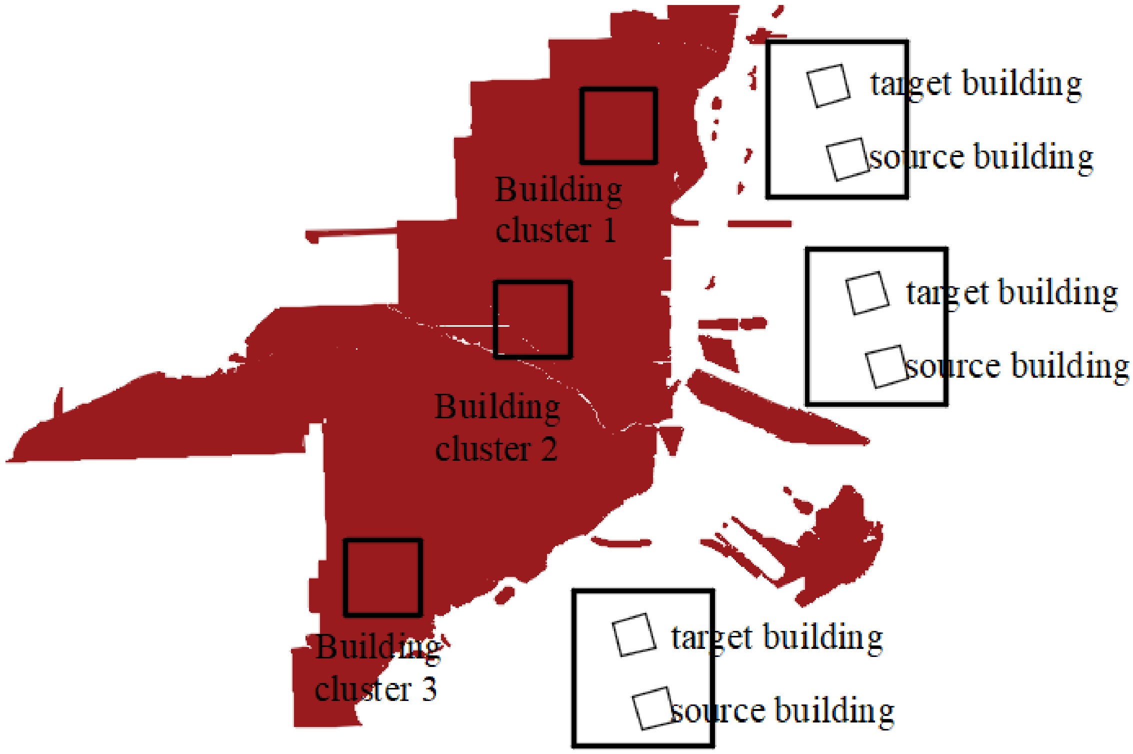

Figure 6.4 Building clusters in the virtual community (case 3)

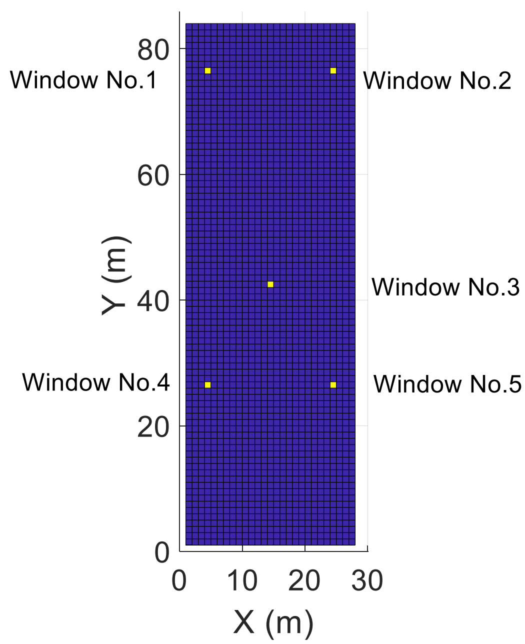

Figure 6.5 Locations of window No.1 to No.5

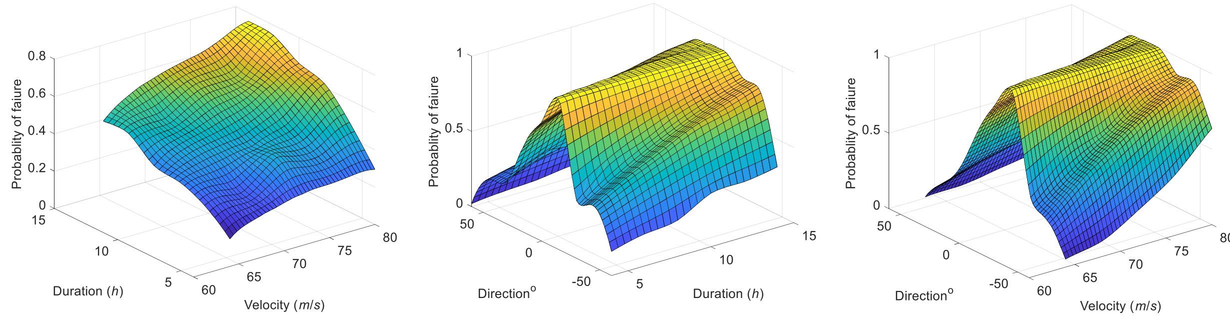

(a) (b) (c)

Figure 6.6 Component level fragility for Window No. 1: (a) $\theta_{\max} = 30^{\circ}$, (b) $V_{\max} = 72$ m/s, (c) $\Delta T = 8\ h$

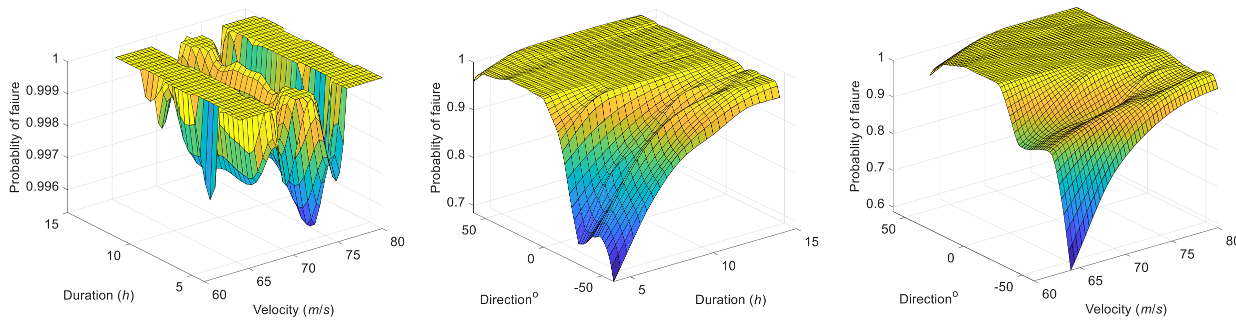

(a) (b) (c)

Figure 6.7 Component level fragility for Window No. 2: (a) $\theta_{\max} = 30^{\circ}$, (b) $V_{\max} = 72$ m/s, (c) $\Delta T = 8\ h$

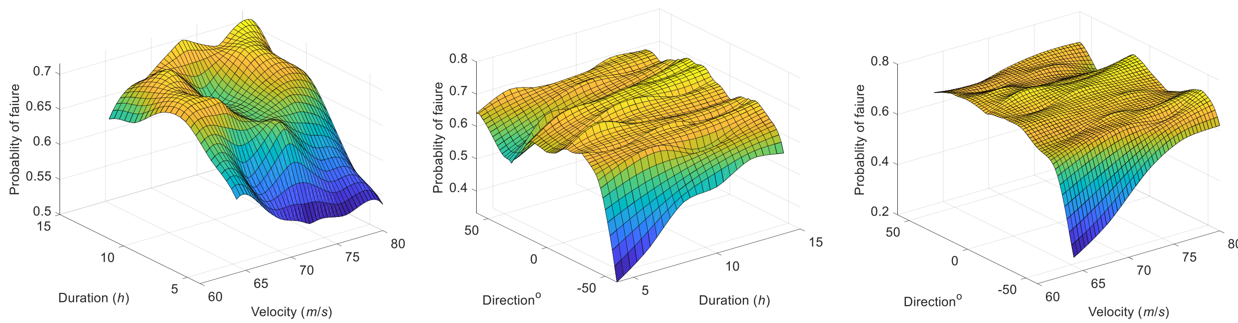

(a) (b) (c)

Figure 6.8 Component level fragility for Window No. 3: (a) $\theta_{\max} = 30^{\circ}$, (b) $V_{\max} = 72$ m/s, (c) $\Delta T = 8\ h$

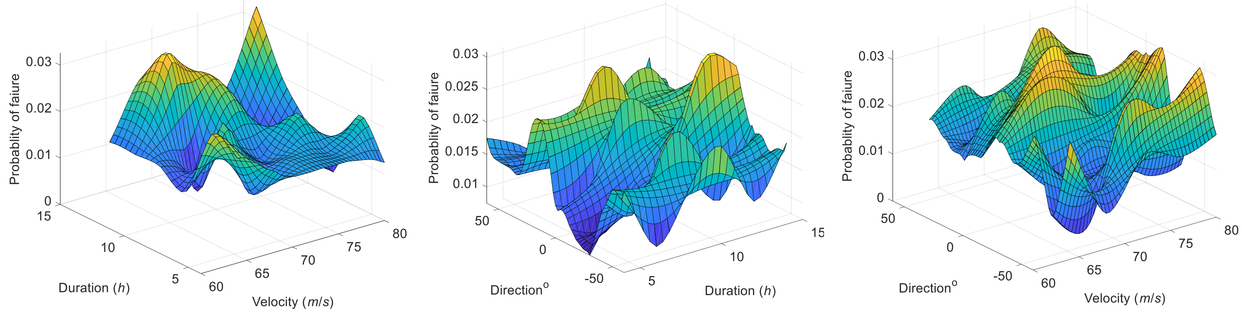

(a) (b) (c)

Figure 6.9 Component level fragility for Window No. 4: (a) $\theta_{\max} = 30^{\circ}$, (b) $V_{\max} = 72$ m/s, (c) $\Delta T = 8\ \ h$

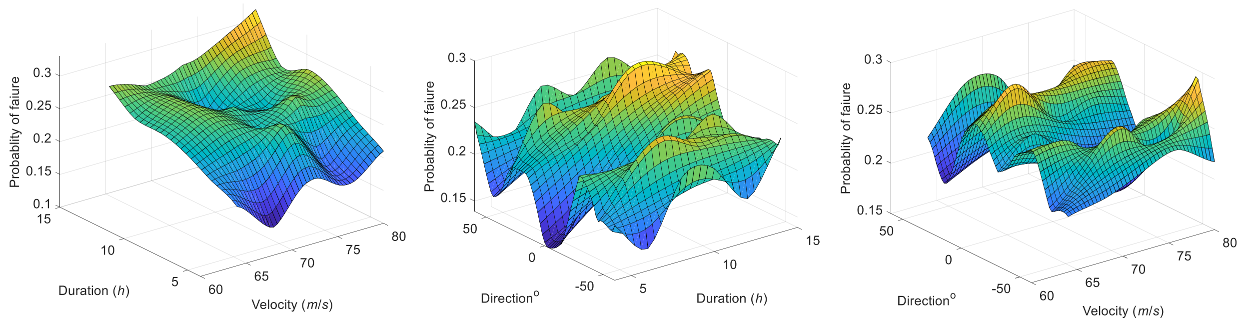

(a) (b) (c)

Figure 6.10 Component level fragility for Window No. 5: (a) $\theta_{\max} = 30^{\circ}$, (b) $V_{\max} = 72$ m/s, (c) $\Delta T = 8\ \ h$

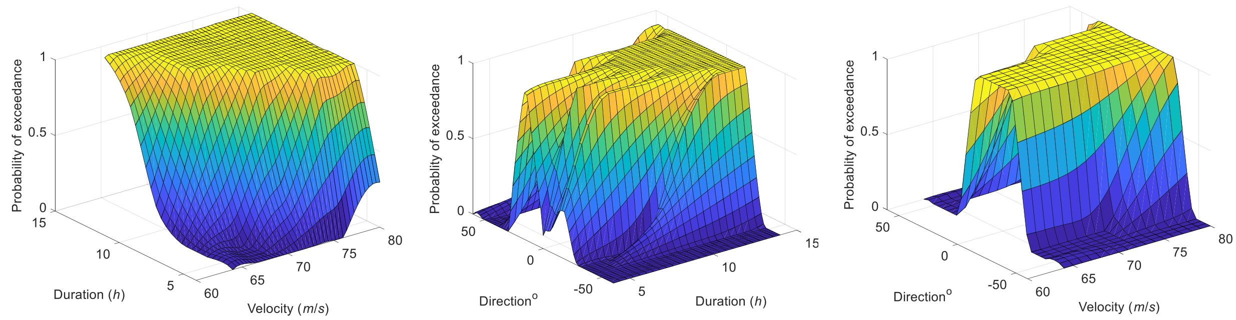

(a) (b) (c)

Figure 6.11 Building level fragility for damage state 4: (a) $\theta_{\max} = 30^{\circ}$, (b) $V_{\max} = 72$ m/s, (c) $\Delta T = 8\ \ h$

The ranges of $V_{\max}$ and ΔT can cover most of the inflow wind profiles corresponding to the studied hurricane scenarios and building clusters in this Chapter while $\theta_{\max}$ only covers 51% of the inflow wind profiles. Since the inflow wind profile with the $\theta_{\max}$ out of the selected range usually indicate small wind velocity in the potential wind direction range of debris damage, -30° to 30° and the computing cost for extending the range of input parameter of multidimensional fragilities is high, it is not worthy to including out of range $\theta_{\max}$ in the fragilities. Thus, the debris induced damage for inflow wind profiles with out of range $\theta_{\max}$ is estimated by multiplying the fragility value of the closest data point in the input space with a reduction factor determined by comparing the duration and maximum wind speed corresponding to the wind direction in the range of -30° to 30°. For instance, one of 700-yr hurricane event has $V_{\max} = 72.12\, m/s, \theta_{\max} = 78.57°$ and $\Delta T = 8.27$ at one building cluster, the closest data point in the input space of fragility has $V_{\max} = 72.12\, m/s, \theta_{\max} = 60°$ and $\Delta T = 8.27\, h$. The duration with wind direction in the range of -30° to 30° for the hurricane event is 6501 sec, while the duration for the data point is 8503 sec. Besides, the maximum wind velocity with wind direction in the range of -30° to 30° for the hurricane event is 47.72 *m/s*, while the maximum wind velocity for the data point is 62.46 *m/s*. Therefore, the reduction factor is $(6501/8503) \times (47.72/62.46) = 0.5841$.

6.3 Results and discussions

The probability of failure for window No.1 to No.5 under 700-yr hurricane events for the three building clusters in virtual urban communities for case 1 to 3, are listed in Tables 6.1 to 6.5. The assessment result of building level damage is shown in Table 6.6. The large CoV values of both component level and building level damage indicate large uncertainty in the wind-borne debris induced damage under hurricane events with the same return period. Thus, directly using the return period of wind speed at the centroid of the community for de-aggregation of debris induced damage, which works well for the wind pressure induced damage, might not be the best option, since the debris induced damage is influenced not only by the maximum wind speed but also the wind direction and duration as shown in Fig. 6.11 (b). Finding a better de-aggregation index instead of the return period of wind speed should be an important task in future research.

As mentioned in Section 6.1, the uncertainty of debris induced damage in one building cluster under different hurricanes is first investigated. As shown in Tables 6.1 to 6.5, the debris damage on window No.1 has the largest CoV and the CoV for other windows are much smaller. Thus, the uncertainty of debris damage on windows in the top-left region of the building wall should be a dominant contributor to the large uncertainty in the probability of exceeding damage state 4 at the building level. The influence of spatial distribution of wind velocity field on the debris induced damage is investigated by comparing the damage assessment results between the three building clusters in the same community under the same hurricane scenario. Similar to the uncertainty of debris damage under different hurricane scenarios, the debris damage for window No.1 also shows a significant difference among building clusters, while the debris damage for other windows looks similar among building clusters. For instance, the standard deviation of probability of failure for window No. 1 of the three building clusters in community case 1 under hurricane No. 4 is 0.244, while the values for windows No. 2 to No. 5 are 0, 0.0173, 0.004, 0.02. The significant difference in the debris damage on building level in different building clusters as shown in Table 6.6 indicates the importance of considering the spatial distribution in evaluating the debris induced damage using de-aggregated hurricane scenarios. Finally, the uncertainty in debris damage with different building configurations under the same hurricane scenario is studied by comparing the debris damage of the three building clusters for case 1 and the corresponding rotated building clusters for

Cases 2 and 3. The influence of rotating building configuration on debris damage is associated with hurricane scenarios. For instance, the probability of failure of window No. 1 to No. 5 is quite similar among building cluster 1 under hurricane scenario No. 1 in community Cases 1 ,2 and 3, while debris damage in building cluster 1 under hurricane scenario No. 5 have a large uncertainty among community Cases 1, 2 and 3 (Tables 6.1-6.5).

Table 6.1 Probability of failure for window No. 1

Scenario	Case1 Building cluster 1	Case1 Building cluster 2	Case1 Building cluster 3	Case2 Building cluster 1	Case2 Building cluster 2	Case2 Building cluster 3	Case3 Building cluster 1	Case3 Building cluster 2	Case3 Building cluster 3
1	0.9943	0.8568	0.7617	0.9064	0.8332	0.4278	0.9584	0.9991	0.8596
2	0.6535	0.5451	0.4774	0.3026	0.8842	0.5391	0.6961	0.4698	0.1200
3	0.1688	0.0186	0.0065	0.4558	0.0880	0.0121	0.0633	0.0093	0.0006
4	0.7965	0.4554	0.3243	0.9386	0.7562	0.4103	0.5029	0.3190	0.0579
5	0.0304	0.0105	0.1017	0.0757	0.0549	0.0386	0.1159	0.1100	0.1017
6	0.0313	0.0038	0.0171	0.0528	0.0105	0.0039	0.0089	0.0190	0.0171
7	0.6262	0.5384	0.1727	0.9268	0.5940	0.4428	0.5172	0.1248	0.0622
8	0.8947	0.9107	0.9633	0.7742	0.8157	0.9945	0.9911	0.9909	0.8196
9	0.0303	0.0195	0.0885	0.0572	0.0565	0.0341	0.0023	0.0948	0.0885
10	0.8068	1.0000	0.3780	0.6169	0.6588	0.1999	0.9581	1.0000	0.6917
11	0.9094	0.6243	0.3776	0.9912	0.8525	0.6498	0.7459	0.3724	0.2383
12	0.1955	0.2241	0.2010	0.3383	0.3610	0.3676	0.0269	0.0370	0.0408
13	1.0000	0.8380	0.9888	1.0000	0.9491	0.7637	0.7654	0.5068	0.9225
14	0.0195	0.0701	0.0702	0.0628	0.0276	0.0163	0.1101	0.0701	0.0702
15	0.0936	0.0394	0.0384	0.0936	0.0394	0.0384	0.0936	0.0394	0.0384
16	0.4574	0.5665	0.3513	0.1777	0.2843	0.1713	0.5828	0.7776	0.5850
17	0.0928	0.0542	0.0165	0.2477	0.1020	0.0570	0.0433	0.0046	0.1008
18	0.2671	0.2750	0.2802	0.2671	0.2750	0.2802	0.2671	0.2750	0.2802
CoV	0.8508	0.9069	0.9987	0.8013	0.8464	0.9733	0.8955	1.0585	1.1603

Table 6.2 Probability of failure for window No. 2

Scenario	Case1			Case2			Case3		
	Building cluster 1	Building cluster 2	Building cluster 3	Building cluster 1	Building cluster 2	Building cluster 3	Building cluster 1	Building cluster 2	Building cluster 3
1	0.9998	0.9875	0.9855	0.9908	0.9881	0.9040	0.9995	1.0000	0.9897
2	0.9444	1.0000	0.9991	0.9000	1.0000	1.0000	0.9212	0.9993	0.9998
3	0.9999	0.6209	0.2801	0.9996	0.8121	0.5251	0.7188	0.3096	0.0244
4	1.0000	1.0000	1.0000	0.9900	1.0000	1.0000	1.0000	0.9968	0.9523
5	0.2617	0.0954	0.9978	0.6521	0.4983	0.3784	0.9986	0.9981	0.9978
6	0.5437	0.1918	0.9331	0.9182	0.5279	0.2105	0.1549	0.9505	0.9331
7	0.9999	0.9983	0.9999	0.9997	1.0000	0.9996	0.9981	0.9990	0.7281
8	0.9899	0.9927	0.9986	0.9878	0.9882	0.9997	0.9978	0.9990	0.9990
9	0.4352	0.2060	0.9999	0.8212	0.5961	0.3851	0.0337	0.9998	0.9999
10	0.9393	1.0000	0.8512	0.9048	1.0000	0.4502	0.9968	1.0000	1.0000
11	1.0000	0.9999	0.9991	0.9950	1.0000	1.0000	1.0000	0.9989	0.9963
12	0.9920	0.9955	0.9980	0.9990	0.9993	0.9992	0.8792	0.8867	0.8382
13	1.0000	1.0000	0.9972	1.0000	0.9989	0.9416	1.0000	0.9998	1.0000
14	0.1768	1.0000	1.0000	0.5701	0.3946	0.2323	0.9996	1.0000	1.0000
15	0.9999	0.9847	0.9842	0.9999	0.9847	0.9842	0.9999	0.9847	0.9842
16	0.9063	0.9751	0.8849	0.7707	0.8128	0.6686	0.8981	0.9849	0.9140
17	0.7528	0.4508	0.1633	1.0000	0.8478	0.5636	0.3515	0.0386	0.9978
18	0.8639	0.8589	0.8618	0.8639	0.8589	0.8618	0.8639	0.8589	0.8618
CoV	0.3334	0.4115	0.2795	0.1427	0.2412	0.4088	0.3766	0.3007	0.2566

Table 6.3 Probability of failure for window No. 3

Scenario	Case1			Case2			Case3		
	Building cluster 1	Building cluster 2	Building cluster 3	Building cluster 1	Building cluster 2	Building cluster 3	Building cluster 1	Building cluster 2	Building cluster 3
1	0.6827	0.6568	0.6569	0.6691	0.6564	0.5724	0.6977	0.6639	0.6504
2	0.6598	0.6657	0.6810	0.5302	0.7052	0.6645	0.6696	0.6835	0.6642
3	0.6643	0.4120	0.1866	0.6771	0.5174	0.3497	0.4737	0.2055	0.0162
4	0.6938	0.6623	0.6655	0.6895	0.6958	0.6537	0.6686	0.6388	0.6295
5	0.1799	0.0653	0.6840	0.4483	0.3411	0.2594	0.6865	0.6833	0.6840
6	0.3590	0.1290	0.6382	0.6062	0.3551	0.1439	0.1023	0.6394	0.6382
7	0.6984	0.6637	0.6653	0.7216	0.6722	0.6732	0.6815	0.6917	0.4812
8	0.6684	0.6514	0.6945	0.6667	0.6518	0.6721	0.6768	0.6703	0.6924
9	0.2891	0.1380	0.6753	0.5455	0.3994	0.2601	0.0224	0.6698	0.6753
10	0.6834	0.7600	0.5188	0.6585	0.6984	0.2744	0.6918	0.7786	0.6776
11	0.6895	0.6812	0.6498	0.6964	0.6875	0.6877	0.6932	0.6462	0.6480
12	0.6472	0.6530	0.6583	0.6601	0.6544	0.6513	0.5758	0.5883	0.5616
13	0.8074	0.6967	0.6904	0.7790	0.6911	0.6752	0.7988	0.6607	0.6987
14	0.1190	0.6678	0.6679	0.3838	0.2635	0.1552	0.6729	0.6678	0.6679
15	0.6651	0.6649	0.6658	0.6651	0.6649	0.6658	0.6651	0.6649	0.6658
16	0.6080	0.6176	0.5449	0.4176	0.4891	0.3695	0.6628	0.6466	0.6658
17	0.5144	0.3081	0.1120	0.7037	0.5796	0.3864	0.2402	0.0264	0.6841
18	0.4782	0.4703	0.4739	0.4782	0.4703	0.4739	0.4782	0.4703	0.4739
CoV	0.3510	0.4197	0.2917	0.1883	0.2572	0.4215	0.3912	0.3133	0.2665

Table 6.4 Probability of failure for window No. 4

	Case1			Case2			Case3		
Scenario	Building cluster 1	Building cluster 2	Building cluster 3	Building cluster 1	Building cluster 2	Building cluster 3	Building cluster 1	Building cluster 2	Building cluster 3
1	0.0272	0.0111	0.0167	0.0196	0.0166	0.0128	0.0201	0.0337	0.0115
2	0.0226	0.0184	0.0179	0.0155	0.0186	0.0185	0.0111	0.0168	0.0175
3	0.0174	0.0118	0.0052	0.0166	0.0143	0.0097	0.0128	0.0059	0.0004
4	0.0231	0.0158	0.0168	0.0182	0.0218	0.0149	0.0179	0.0141	0.0137
5	0.0048	0.0021	0.0222	0.0120	0.0110	0.0084	0.0183	0.0219	0.0222
6	0.0074	0.0033	0.0146	0.0124	0.0091	0.0033	0.0021	0.0165	0.0146
7	0.0178	0.0249	0.0178	0.0231	0.0190	0.0173	0.0217	0.0135	0.0131
8	0.0214	0.0208	0.0191	0.0153	0.0131	0.0265	0.0260	0.0266	0.0189
9	0.0074	0.0032	0.0140	0.0139	0.0093	0.0054	0.0006	0.0157	0.0140
10	0.0113	0.0196	0.0190	0.0155	0.0250	0.0101	0.0132	0.0196	0.0213
11	0.0197	0.0202	0.0142	0.0127	0.0198	0.0214	0.0240	0.0144	0.0142
12	0.0152	0.0153	0.0147	0.0164	0.0150	0.0145	0.0145	0.0128	0.0113
13	0.0271	0.0232	0.0146	0.0243	0.0171	0.0113	0.0213	0.0172	0.0207
14	0.0028	0.0184	0.0184	0.0091	0.0072	0.0043	0.0159	0.0184	0.0184
15	0.0166	0.0171	0.0169	0.0166	0.0171	0.0169	0.0166	0.0171	0.0169
16	0.0171	0.0133	0.0172	0.0134	0.0099	0.0116	0.0126	0.0129	0.0179
17	0.0163	0.0098	0.0036	0.0223	0.0184	0.0125	0.0076	0.0008	0.0222
18	0.0132	0.0127	0.0128	0.0132	0.0127	0.0128	0.0132	0.0127	0.0128
CoV	0.4465	0.4649	0.2997	0.2539	0.3167	0.4592	0.4576	0.4404	0.3339

Table 6.5 Probability of failure for window No. 5

Scenario	Case1			Case2			Case3		
	Building cluster 1	Building cluster 2	Building cluster 3	Building cluster 1	Building cluster 2	Building cluster 3	Building cluster 1	Building cluster 2	Building cluster 3
1	0.2373	0.2501	0.2455	0.2460	0.2550	0.1845	0.2445	0.2523	0.2536
2	0.2492	0.2488	0.2096	0.2207	0.2704	0.2455	0.2326	0.2104	0.2330
3	0.2276	0.1528	0.0687	0.2150	0.1751	0.1287	0.1682	0.0762	0.0060
4	0.2279	0.2499	0.2106	0.1987	0.2182	0.2351	0.2446	0.2047	0.2339
5	0.0626	0.0226	0.2357	0.1561	0.1179	0.0894	0.2391	0.2361	0.2357
6	0.1351	0.0473	0.2338	0.2282	0.1303	0.0527	0.0385	0.2346	0.2338
7	0.2705	0.2174	0.2271	0.2672	0.2390	0.2163	0.2283	0.2412	0.1705
8	0.2397	0.2540	0.2528	0.2406	0.2530	0.2467	0.2483	0.2516	0.2696
9	0.1032	0.0492	0.2451	0.1948	0.1423	0.0944	0.0080	0.2387	0.2451
10	0.2127	0.2524	0.2103	0.2401	0.2633	0.1112	0.1874	0.2597	0.2493
11	0.1943	0.2360	0.2371	0.1903	0.1994	0.2338	0.2331	0.2278	0.2020
12	0.2170	0.2146	0.2167	0.2324	0.2307	0.2240	0.2242	0.2178	0.1988
13	0.2911	0.2237	0.1876	0.2940	0.1914	0.2244	0.3060	0.2418	0.2068
14	0.0416	0.2320	0.2319	0.1341	0.0915	0.0539	0.2351	0.2320	0.2319
15	0.2363	0.2214	0.2203	0.2363	0.2214	0.2203	0.2363	0.2214	0.2203
16	0.2459	0.2208	0.2262	0.1980	0.1563	0.1619	0.2356	0.2511	0.2451
17	0.1786	0.1069	0.0386	0.2436	0.2010	0.1331	0.0834	0.0091	0.2356
18	0.1975	0.1937	0.1955	0.1975	0.1937	0.1955	0.1975	0.1937	0.1955
CoV	0.3504	0.4138	0.2825	0.1743	0.2673	0.3979	0.3924	0.3067	0.2677

Table 6.6 Probability of exceeding damage state 4 at building level

Scenario	Case1 Building cluster 1	Case1 Building cluster 2	Case1 Building cluster 3	Case2 Building cluster 1	Case2 Building cluster 2	Case2 Building cluster 3	Case3 Building cluster 1	Case3 Building cluster 2	Case3 Building cluster 3
1	1.0000	0.9478	0.1335	0.9477	0.1445	0.0000	1.0000	1.0000	0.8269
2	0.0042	1.0000	0.5144	0.0000	1.0000	1.0000	0.1814	0.4767	0.0272
3	0.0711	0.0000	0.0000	0.4694	0.0000	0.0000	0.0000	0.0000	0.0000
4	1.0000	0.5930	0.0433	0.9995	1.0000	0.8654	0.7376	0.0855	0.0000
5	0.0029	0.0012	0.0075	0.0073	0.0064	0.0028	0.0111	0.0128	0.0075
6	0.0000	0.0000	0.0000	0.0000	0.0000	0.0000	0.0000	0.0000	0.0000
7	0.9990	0.9210	0.0738	1.0000	1.0000	0.4708	0.9299	0.0171	0.0000
8	0.9142	0.9931	1.0000	0.3944	0.4789	1.0000	1.0000	1.0000	1.0000
9	0.0000	0.0000	0.0000	0.0000	0.0000	0.0000	0.0000	0.0000	0.0000
10	0.5004	0.6054	0.0000	0.0263	0.1139	0.0000	1.0000	1.0000	0.0977
11	1.0000	0.8679	0.4165	1.0000	1.0000	0.8837	0.9750	0.4080	0.0008
12	0.0000	0.0000	0.0004	0.3879	0.4874	0.4259	0.0000	0.0000	0.0000
13	1.0000	1.0000	1.0000	1.0000	1.0000	0.3592	1.0000	0.8842	1.0000
14	0.0000	0.0000	0.0000	0.0000	0.0000	0.0000	0.0000	0.0000	0.0000
15	0.0000	0.0000	0.0000	0.0000	0.0000	0.0000	0.0000	0.0000	0.0000
16	0.0000	0.0000	0.0000	0.0000	0.0000	0.0000	0.0069	0.4892	0.0040
17	0.0159	0.0087	0.0011	0.2913	0.0163	0.0039	0.0074	0.0007	0.0069
18	0.0000	0.0000	0.0000	0.0000	0.0000	0.0000	0.0000	0.0000	0.0000
CoV	1.2968	1.1822	1.8849	1.1867	1.2757	1.4224	1.2402	1.3637	2.1814

CHAPTER 7 SUMMARY AND FUTURE STUDIES

7.1 Summary and conclusions

A comprehensive approach for risk assessment of windborne debris induced damage on community level under hurricanes is proposed in this dissertation. This approach involves the selection of hurricane scenarios for a stipulated return period hazard level through de-aggregation approach (Chapter 2), construction of the fragilities for debris induced damage in individual building cluster using the proposed damage assessment model (Chapter 3), and efficient and accurate estimation of urban wind velocity field for arbitrary building clusters in communities through the proposed machine learning based data-driven prediction models (Chapter 4). In addition, uncertainty analysis for the procedure of risk assessment of windborne debris induced damage is conducted in Chapter 5 considering the system complexity. As an illustrative example, this approach is applied to estimate the debris induced damage in a virtual community in Chapter 6. The conclusions and findings obtained from investigating this risk assessment approach in this dissertation are summarized in the following:

(1) Synthetic hurricane scenarios over 200,000 years are generated with statistical hurricane genesis and track transportation model for conducting scenario-based damage assessment. The scenarios with the highest probability of occurrence, given the return period stipulated, are studied for damage assessment of the city of Miami, FL. These hurricane scenarios represent the dominant contributors to community risk at this return period and provide a basis for the resilience and risk assessment of coastal communities. This scenario-based approach can capture the spatial variation in the hurricane wind speed and properly evaluate damage at the community level. This community level damage assessment of Miami involves many building archetypes, e.g., commercial buildings,

schools, public assembly buildings, fire stations, police stations and the hospitals. The results show that there is a distinct possibility that the damages estimated from a single hurricane scenario, or a historical hurricane will underestimate the damage sustained by the community by a significant margin. Systematically selecting multiple hurricane scenarios is necessary to achieve unbiased estimation of community level damage.

(2) A windborne debris induced damage assessment model, including the debris generation, transportation, and impact, is proposed in Chapter 3. This damage assessment model is used to construct fragilities of debris induced damage, which is critical for community resilience. The intensity measurements of hurricane, including the maximum wind speed at the site, the wind direction corresponding to the maximum wind speed and the duration, compose the input space of fragilities for debris damage. Accordingly, a reduced-order model of the time varying hurricane wind speed with the three intensity measurements is proposed to facilitate the construction of the fragility. Furthermore, a kriging based surrogate model for the physical-based debris trajectory model is developed to reduce the computing cost to make the calculation of fragilities achievable. Both the fragilities on component level and building level are developed in this study. According to the fragilities constructed for a tall building in Miami, hurricanes with longer duration might be destructive for building envelopes even with low wind speed. The translation speed of hurricanes tends to decrease in the future due to climate change, which may increase the risk of building envelopes under hurricanes.

(3) A machine learning based data-driven wind velocity prediction model developed using cGANs model is proposed to offer efficient and accurate estimation of local wind field around arbitrary building cluster for community level damage assessment in Chapter 4. Although this study starts with simple building clusters comprised of two buildings, all the important input

variables (including the building height and geometry, the relative location of buildings and inflow wind direction) in inflow wind profile and building configurations are considered in this prediction model. The biggest challenge in this study is the high computational cost of obtaining training data. Thus, several methods are applied to reduce the complexity of the system that cGANs model needs to learn, e.g. keeping the similarity for the input and output, and developing separate prediction model for each velocity component at each height level. Furthermore, an efficient sampling approach is proposed by determining the most efficient direction for increasing the sample size of training data. The proposed prediction models show low prediction error on the test dataset except for the prediction of wind velocity component in cross wind direction and in the vortex region over the rooftop. Developing separate prediction models for the vortex region might be necessary in the future since the vortex region over rooftop is critical for the generation of compact debris (roof gravel) generation.

(4) Uncertainty quantification for factors involved in the procedure of risk assessment of windborne debris induced damage is conducted in Chapter 5. Uncertainty propagation within and among subsystems is investigated. The results of uncertainty propagation reveal that the uncertainty in assessing debris induced damage is large (CoV in the order 40%). The sensitivity analysis results indicate that the debris induced damage is sensitive to the inflow wind velocity. Thus, the downscaling from mesoscale wind to microscale wind to better estimate inflow wind velocity are worthy to study in future. The pressure deficit and Holland parameter B are dominant factors contributing to the uncertainty in the inflow wind velocity. When the Holland-type model is involved in the downscaling, one may focus on improving the models of pressure deficit and parameter B in future studies.

(5) Risk assessment of debris induced damage on community level is illustrated using a virtual community in Chapter 6. The fragilities for the target building in building clusters are developed with the local wind field predicted using the data-driven models developed in Chapter 4. The hurricane scenarios used in the damage assessment of windborne debris are the same as those used for the damage assessment of wind pressure in Chapter 2. The windborne debris damage assessment results show the following. 1) The debris induced damage in one building cluster under different hurricane scenarios has large uncertainty. 2) The spatial distribution of wind velocity field has large influence on the debris induced damage. 3) The influence of changing building configuration on the debris damage is associated with the hurricane scenarios. Even rotating the building cluster with a small angle can greatly affect the debris damage under some hurricane scenarios.

7.2 Summary of contributions to the profession

The research effort proposed herein provides the following contributions to the research communities:

De-aggregation of wind speeds for hurricane scenarios: The proposed de-aggregation approach for hurricane scenarios establishes a relation between hurricane scenario selection for community resilience assessment and the building regulatory process, which is based on wind speeds associated with a stipulated return period. In contrast to existing scenario approaches, the de-aggregation process herein permits a rigorous consideration of uncertainties of hurricane winds in community resilience analysis, thereby leading to improved estimates of severe hurricane wind fields and windborne debris damage at the community level and represents an advance for estimating statistics of damage and loss realistically for community decision-making.

Fragility model for windborne debris damage: A new fragility modeling approach for urban high/mid-rise buildings envelopes subjected to hurricane-driven windborne debris hazards at both the component and building level is proposed. Since the debris-induced damage is sensitive to the configuration of building clusters, the proposed fragility modeling approach explicitly considers the geometric configuration of building clusters through modeling urban wind fields and the environment of debris sources. This type of fragility functions for urban high/mid-rise buildings have not been developed to this point in the literature. To facilitate the development of the fragility models, a new computationally efficient approach to simulate the complex hurricane urban wind field that integrating the Holland wind field model, parametric model of local wind vortex, and deep learning approaches is proposed. This new approach to simulate hurricane-induced urban wind enables the efficient simulation of debris impact process in an urban building cluster. In addition, the proposed surrogate model for debris trajectory and the reduced order wind speed model significantly reduces the cost of developing fragility models.

Machine learning based prediction model of urban wind field: The proposed machine learning based prediction model reduces the computational cost of simulating the local wind field over different building clusters for windborne debris damage assessment. Most of the existing machine learning based studies for predicting wind field focus on the wind pressure acting on individual buildings, while the prediction models for directly estimating the wind velocity field around building clusters are lacking. The proposed predication model for wind field is the first-of-its-kind. An efficient sampling strategy and other methods, e.g., building separate data-driven models for each height levels and maintaining the similarity between input images and output images, are proposed for achieving high prediction accuracy with limited size of training data. These methods are not only valid for the two-building cluster investigated in this study, but also useful for reducing the size of training data in the future study of more complex building clusters. This type of intelligent sampling strategy has not been reported in other studies on machine learning models in the wind engineering field and is expected to help guide data generation in both wind tunnel experiments and CFD simulations in similar applications.

Uncertainty analysis and propagation for windborne debris damage assessment: A comprehensive analysis of uncertainty in various factors involved in the procedure of windborne debris damage assessment is conducted. The uncertainty quantification, uncertainty propagation and sensitivity analysis results indicate the major contributors to the uncertainty in debris damage assessment, which helps identify the directions of future research towards further reduction of uncertainties.

Community resilience framework for windborne debris damage to high-rise buildings: With the proposed fragility model and de-aggregation for hurricane scenarios, unbiased damage assessment of windborne debris to high-rise buildings within building clusters at a community level was enabled. In addition, the hurricane scenarios obtained through the de-aggregation based on RP wind speed in windborne debris damage assessment can also be used for assessment of the wind pressure-induced damage (structural or nonstructural), which is dominate by the wind speed, under the community resilience framework for hurricane risk.

7.3 Directions of future studies

Possible improvements or extensions to the windborne debris damage assessment based on current research are discussed in the following:

Involving more physics in simulation models for hurricanes: The main issue in the subsystem of hurricane simulation is the uncertainty in the wind velocity. As shown in Table 5.1, the CoV of wind velocity is 0.18 under that condition that not all the uncertainties in the hurricane simulation have been studied in this dissertation. This uncertainty might not be small for simulating hurricanes with statistical approaches, since most of those statistical approaches are developed based on the historical hurricanes occurred in the past 200 years, which is a rather short time period. Thus, in future studies, physical based approaches will be applied for future hurricane simulation to reduce the uncertainty in wind velocity. For example, Emanuel et al. (2004) proposed a physical based prediction model for hurricane intensity called Coupled Hurricane Intensity Prediction System (CHIPS). This prediction model is a simple coupled atmosphere-ocean model. Although the genesis of hurricane is random, the intensity evolution of hurricane is deterministic and physics based. It is demonstrated that CHIPS can offer accurate prediction of hurricane intensity (Emanuel et al., 2004). Furthermore, considering climate change effect in the CHIPS through updating parameter in the coupled atmosphere-ocean model is intuitive. Many atmosphere models and parameters in the ocean model, e.g., sea surface temperature, under climate change are easy to access and can be injected to CHIPS model to simulate hurricanes in future climate.

De-aggregation approach for joint hazards of windborne debris and pressure induced damage: The de-aggregation results for the wind pressure induced damage assessment in Miami city are directly used for the windborne debris damage assessment in virtual communities. The relatively large uncertainties shown in Tables 6.1 to 6.6 in the debris damage in different building clusters under different hurricane scenarios indicate that de-aggregation for return period wind speed may not the best option for debris damage assessment on community level. Compared to the wind pressure induced damage, debris damage is dominated by the local wind velocity field and the damage pattern is associated with time history of wind speed rather than the maximum wind speed. To obtain the de-aggregation index that works for both the wind pressure and debris induced damage, the joint probability distribution of the two types of damage will be calculated with synthetic hurricanes. Then, the return period of this joint event will be used as basis for de-aggregation.

Exploration of additional debris type and mechanisms of debris generation and transportation: Only the compact debris is investigated in the subsystem of modeling debris induced damage. This will be extended by investigating plate-type debris in the future. Furthermore, the assumption of debris generation mechanism for high-rise building lacks the support of field test data. Some empirical parameters in debris generation are adopted from the field test data of low-rise buildings. Also, the uncertainty of debris trajectory model under urban winds was not quantified due to lack of data. In future studies, 1) some field tests may be needed for investigating the debris generation mechanism for high-rise building; 2) the behavior of the plate-type debris under urban winds needs to be investigated through wind tunnel test; 3) Measurement data in field and wind tunnel are needed to quantify epistemic uncertainties in the debris trajectory model.

Improvement of prediction accuracy of local wind field model: The prediction accuracy is important in the subsystem of predicting the local wind field with data-driven models. A parametrical model is used to evaluate the wind velocity field in the vortex region over the rooftop instead of using the predicted wind velocity data from data-driven models. This is because the flow pattern in the vortex region is quite complicated, and the CFD simulations with RANS model may not provide accurate wind velocity field in the vortex region. Thus, more specific data-driven models should be developed to capture the details in the vortex region. In addition, the data-driven models for the vortex region and other regions might be developed separately to reduce the computing cost. Furthermore, the uncertainties of CFD models used to generate the training data need to be quantified, which requires collection of urban wind field data through wind tunnel tests or full-scale measurements if possible.

Generalization of prediction model of local wind field: The prediction model proposed in this dissertation only works for building clusters with two buildings. This prediction model should be extended to cover more types of building cluster. However, extending the prediction model usually means that more training data is required. The required size for extra training data varies with the different types of parameters. For instance, extending the prediction with the number of buildings would need much more training data than varying geometry of buildings. This difference is determined by the importance of parameters on predicting the wind velocity field. Therefore, sensitivity analysis of parameters for the wind velocity field should be done before extending the prediction model to inform the data needs. The sampling strategy proposed in Chapter 4 should be used for efficient sampling of training data when extending the prediction model. For instance, the two-building cluster in the dissertation can be extended to three-building cluster in future work. In this case, two extra distance and one extra height information are added to the input space. In this case, a total of seven parameters are considered in generating training data. Sensitivity analysis for the wind velocity field will be conducted and the sampling size for each parameter will be increased to follow the order of importance of each parameter.

REFERENCES

Alphonso, T.C. and Barbato, M. 2014. " Experimental fragility curves for aluminum storm panels subject to windborne debris impact. " *J. Wind Eng. Ind. Aerodyn*., 134, 44-55. https://doi.org/10.1016/j.jweia.2014.08.010.

ASCE. 2016. Minimum Design Loads and Associated Criteria for Buildings and Other Structures. Reston, VA: ASCE.

ASTM 2000. *Standard Specification For Mineral Aggregate Used On Built-Up Roofs*. ASTM D1863-93. West Conshohoken, Pa: ASTM.

ASTM 2013. *Standard Test Method for Performance of Exterior Windows, Curtain Walls and Storm Shutters Impacted by Missile(s) and Exposed to Cyclic Pressure Differentials*. ASTM E1886-13a. West Conshohoken, Pa: ASTM.

ASTM. 2021. Standard test method for water penetration of exterior windows, doors, and curtain walls by uniform static air pressure difference, ASTM E 330-02. West Conshohoken, Pa: ASTM.

Banks, D., and Meroney, R. N. 2001. "A model of roof-top surface pressures produced by conical vortices: Model development." *J. Wind Struct*., 4(3), 227-246. https://doi.org/10.12989/was.2001.4.3.227

Barbato, M., Petrini, F., Unnikrishnan, V. U. and Ciampoli, M. 2013. "Performance-based hurricane engineering (PBHE) framework. " *Struct. Saf*., 45, 24-35. https://doi.org/10.1016/j.strusafe.2013.07.002

Behr, R.A., and Minor, J.E. 1994. "A survey of glazing system behavior in multistory buildings during hurricane andrew." *Struct. Des. Tall Build*., 3(3), 143-161. https://doi.org/10.1002/tal.4320030302

Bourgault, G. 2021. "Probability Transform of Kriging Estimates and Its Effects on Selection Bias and Conditional Bias. " *Math. Geosci*., 54(2), 345-362. https://doi.org/10.1007/s11004-021-09974-6

Calzolari, G. and Liu, W. 2021. "Deep learning to replace, improve, or aid CFD analysis in built environment applications: A review. " *Build Environ*., 206, 108315. https://doi.org/10.1016/j.buildenv.2021.108315

Chen, W., Hao, H., Li, J. 2015. "Fragility curves for corrugated structural panel subjected to windborne debris impact " In *Proc*., *International Conference on Performance-based and Life-cycle Structural Engineering*, 877-883. Brisbane, Australia.

Ciampoli, M., Petrini, F. and Augusti, G. 2011. "Performance-based wind engineering: towards a general procedure. " Struct. Saf., 33(6), 367-378. https://doi.org/10.1016/j.strusafe.2011.07.001

Creswell, A., White, T., Dumoulin, V., Arulkumaran, K., Sengupta, B. and Bharath, A. A. 2018. "Generative adversarial networks: An overview. " IEEE *Signal Process*. Mag., 35(1), 53-65. https://doi.org/10.1109/MSP.2017.2765202

Dagnew, A. K., and Bitsuamlak, G. T. 2014. "Computational evaluation of wind loads on a standard tall building using LES. " *Wind Struct*., 18(5), 567-598. https://doi.org/10.12989/was.2014.18.5.567

Darling, R. W. R. 1991. "Estimating probabilities of hurricane wind speeds using a large-scale empirical model. " *J. Clim*., 4(10), 1035-1046. https://doi.org/10.1175/1520-0442(1991)004<1035:EPOHWS>2.0.CO;2

Ding, C. and Lam, K. P. 2019. "Data-driven model for cross ventilation potential in high-density cities based on coupled CFD simulation and machine learning. " *Build Environ*., 165, 106394. https://doi.org/10.1016/j.buildenv.2019.106394

Dong, Y., Guo, Y., Ellingwood, B. R., & Mahmoud, H. N. 2022. "Deaggregation of Wind Speeds for Hurricane Scenarios Used in Risk-Informed Resilience Assessment of Coastal Communities. " *J. Struct. Eng*., 148(11), 04022175. https://doi.org/10.1061/(ASCE)ST.1943-541X.0003410

Dong Y, Guo Y, van de Lindt JW. 2023. "Fragility Modeling of Urban Building Envelopes Subjected to Windborne Debris Hazards." *J. Struct. Eng*. 149(5), 04023041. https://doi.org/10.1061/JSENDH.STENG-11732

Ellingwood, B. 1990. "Validation studies of seismic PRAs." *Nuclear Engr. and Des*., 123(2), 189-196. https://doi.org/10.1016/0029-5493(90)90237-R

Ellingwood, B. R., Rosowsky, D. V., Li, Y., and Kim, J. H. 2004. "Fragility assessment of light-frame wood construction subjected to wind and earthquake hazards." *J. Struct. Eng*., 130(12), 1921-1930. https://doi.org/10.1061/(ASCE)0733-9445(2004)130:12(1921)

Elshaer, A., Aboshosha, H., Bitsuamlak, G., El Damatty, A., and Dagnew, A. 2016. "LES evaluation of wind-induced responses for an isolated and a surrounded tall building. " *Eng. Struct*., 115, 179-195. https://doi.org/10.1016/j.engstruct.2016.02.026

Elshaer, A., Gairola, A., Adamek, K., and Bitsuamlak, G. 2017. "Variations in wind load on tall buildings due to urban development. " *Sustain. Cities Soc*., 34, 264-277. https://doi.org/10.1016/j.scs.2017.06.008

Emanuel, K. A. 1988. "The maximum intensity of hurricanes. " *J. Atmos. Sci*., 45(7), 1143–1155. https://doi.org/10.1175/1520-0469(1988)045<1143:TMIOH>2.0.C O;2

Emanuel K, DesAutels C, Holloway C, Korty R. 2004. “Environmental control of tropical cyclone intensity”. *J. Atmos*.;61(7):843-58.

FEMA (Federal Emergency Management Agency). 2015. *HAZUS-MH 2.1 hurricane model* *technical manual*. U.S. Department of Homeland Security, Mitigation Division, Washington, DC:FEMA. Accessed June 2, 2022. https://www.hsdl.org/?view&did=701256

Georgiou, P. N. 1985. "Design windspeeds in tropical cyclone-prone regions." PhD thesis, University of Western Ontario, London, Ontario, Canada.

Gal, Y., & Ghahramani, Z. 2016. "Dropout as a bayesian approximation: Representing model uncertainty in deep learning." In proceeding international conference on machine learning (pp. 1050-1059). PMLR.

Georgiou, P. N. 1985. "Design windspeeds in tropical cyclone-prone regions." PhD thesis, University of Western Ontario, London, Ontario, Canada.

Giusti, A.C. 2020. "Lake Charles Tower's Window Damage Perplexes Engineers." *Engineering News-Record*, September 24, 2020. Accessed June 2, 2022. https://www.enr.com/articles/50130-lake-charles-towers-window-damage-perplexes-engineers

Gu, J., Wang, Z., Kuen, J., Ma, L., Shahroudy, A., Shuai, B., Liu, T., Wang, X., Wang, G., Cai, J., and Chen, T. 2018. "Recent advances in convolutional neural networks. " *Pattern recognition*, 77, 354-377. https://doi.org/10.1016/j.patcog.2017.10.013

Gui, J., Sun, Z., Wen, Y., Tao, D., and Ye, J. 2021. "A review on generative adversarial networks: Algorithms, theory, and applications. " IEEE *Trans. Knowl. Data Eng*.

Guo, Y., and van de Lindt, J. W. 2019. "Simulation of Hurricane Wind Fields for Community Resilience Applications: A Data-Driven Approach Using Integrated Asymmetric Holland Models for Inner and Outer Core Regions." *J. Struct. Eng*., 145 (9), 04019089. https://doi.org/10.1061/(ASCE)ST.1943-541X.0002366

Gurley, K., Pinelli, J.P., Subramanian, C., Cope, A., Zhang, L., Murphree, J., Artiles, A., Misra, P., Gulati, S., and Simiu, E. 2005. "Florida public hurricane loss projection model engineering team:

Final report." International Hurricane ResearchCenter, Florida International Univ., Miami, FL.

Hager, W. H. 2018. "Bed-load transport: advances up to 1945 and outlook into the future. " *J. Hydraul. Res*., 56(5), 596-607. https://doi.org/10.1080/00221686.2017.1405370

Harmsen, S., and A. Frankel 2001. "Geographic de-aggregation of seismic hazard in the United States", *Bull. Seism. Soc. Am*. 91, 13–26.

Harper, B. A., Kepert, J. D., and Ginger, J. D. 2010. "Guidelines for converting between various wind averaging periods in tropical cyclone conditions." Geneva, Switzerland: WMO.

Hassan, E. and Mahmoud, H. 2019. "Full Functionality and Recovery Assessment Framework for a Hospital Subjected to a Scenario Earthquake Event." *Eng. Struct*., 188, 165-177, https://doi.org/10.1016/j.engstruct.2019.03.008

Hassan, E. and Mahmoud, H. 2020. "An Integrated Socio-Technical Approach for Post-Earthquake Recovery of Interdependent Healthcare System." *Reliab. Eng. Syst. Saf*. 201, https://doi.org/10.1016/j.ress.2020.106953

He, J., and Song, C. C. 1997. "A numerical study of wind flow around the TTU building and the roof corner vortex." *J. Wind Eng. Ind. Aerodyn*., 67, 547-558. https://doi.org/10.1016/S0167-6105(97)00099-8

Hemida, H., Šarkić, A., Gillmeier, S., and Höffer, R. 2015. "Experimental investigation of wind flow above the roof of a high-rise building." In *Proc*., *WINERCOST Workshop Trends and Challenges for Wind Energy Harvesting*, 25-34, Coimbra, Portugal

Hinton, G and coauthors.2012. "Deep neural networks for acoustic modeling in speech recognition. " IEEE *Signal Process*. 29, 82–97. https://doi.org/10.1109/MSP.2012.2205597

Holland, G. J. 1980. "An analytic model of the wind and pressure profiles in hurricanes." *Mon. Weather Rev*., 108(8), 1212-1218. https://doi.org/10.1175/1520-0493(1980)108<1212:AAM

OTW>2.0.CO;2

Holmes, J. D. 2004. "Trajectories of spheres in strong winds with application to wind-borne debris." *J. Wind Eng. Ind. Aerodyn.*, 92(1), 9-22. https://doi.org/10.1016/j.jweia.2003.09.031

Hong, Y. 2013. "On computing the distribution function for the Poisson binomial distribution." *Comput. Stat. Data Anal*., 59, 41-51. https://doi.org/10.1016/j.csda.2012.10.006

Hu, G., Liu, L., Tao, D., Song, J., Tse, K. T. and Kwok, K. C. 2020. "Deep learning-based investigation of wind pressures on tall building under interference effects. " *J. Wind Eng. Ind. Aerodyn*., 201, 104138. https://doi.org/10.1016/j.jweia.2020.104138

Isola, P., Zhu, J. Y., Zhou, T., & Efros, A. A. 2017. "Image-to-image translation with conditional adversarial networks." In *Proc*., *IEEE conference on computer vision and pattern recognition*. 1125-1134.

Jain, A. 2015. "Hurricane wind-generated debris impact damage to the glazing of a high-rise building. " *Forensic Engineering*. 361-370.

Jia, G., and Taflanidis, A. A. 2013. "Kriging metamodeling for approximation of high-dimensional wave and surge responses in real-time storm/hurricane risk assessment." *Comput. Methods Appl. Mech. Eng*., 261, 24-38. https://doi.org/10.1016/j.cma.2013.03.012

Kalnay, E., Kanamitsu, M., Kistler, R., Collins, W., Deaven, D., Gandin, L., Iredell, M., Saha, S., White, G., Woollen, J., Zhu, Y., Leetmaa, A., Reynolds, B., Chelliah, M., Ebisuzaki, W., Higgins, W., Janowiak, J., Mo, K. C., Ropelewski, C., Wang, J. Jenne, R., and Joseph, D. 1996. "The NCEP/NCAR 40-year reanalysis project." *Bull. Am. Meteorol. Soc*., 77(3), 437–471. https://doi.org/10.1175/1520-0477(1996)077<0437:TNYRP>2.0.CO;2

Kang, D., Ko, K., and Huh, J. 2015. "Determination of extreme wind values using the Gumbel distribution." *Energy*, 86, 51-58. https://doi.org/10.1016/j.energy.2015.03.126

Kareem, A. 1985. "Structural performance and wind speed damage correlation in Hurricane Alicia." *J. Struct. Eng*., 111(12), 2596-2610. https://doi.org/10.1061/(ASCE)0733-9445(1985)111:12(2596)

Kareem, A. 1986. "Performance of cladding in Hurricane Alicia. " *J. Struct. Eng*. 112(12), 2679-2693. https://doi.org/10.1061/(ASCE)0733-9445(1986)112:12(2679)

Kareem, A., and Bashor, R.2006. "Performance of glass/cladding of high-rise buildings in Hurricane Katrina." Natural Hazards Modeling Laboratory, University of Notre Dame. Accessed June 2, 2022. https://nathaz.nd.edu/documents/Katrina_AAWE_9-21.pdf

Karimpour, A., and Kaye, N. B. 2012. "The critical velocity for aggregate blow-off from a built-up roof." *J. Wind Eng. Ind. Aerodyn.*, 107, 83-93. https://doi.org/10.1016/j.jweia.2012.03.031

Kim, B., Lee, D. E., Preethaa, K. S., Hu, G., Natarajan, Y. and Kwok, K. C. 2021. "Predicting wind flow around buildings using deep learning." *J. Wind Eng. Ind. Aerodyn*., 219, 104820. https://doi.org/10.10 16/j.jweia.2021.104820

Kind, R.J., and Wardlaw, R.L. 1977. "The Development of a Procedure for the Design of Rooftops Against Gravel Blow-off and Scour in High Winds." In *Proc*., *Symposium on Roofing Technology*, 112-123, Gaithersburg, Md.

Kind, R.J., and Wardlaw, R.L. 1984. "Behavior in Wind of Loose-Laid Roof Insulation Systems, Part I: Stone Scour and Blow-Off." In *Proc*., *4th Canadian Workshop on Wind Engineering*, 141-149. Toronto, Canada.

Kind, R. J. 1986. "Measurement in small wind tunnels of wind speeds for gravel scour and blowoff from rooftops." *J. Wind Eng. Ind. Aerodyn.*, 23, 223-235. https://doi.org/10.1016/0167-6105(86)90044-9

Konka, S., Govindray, S. R., Rajasekharan, S. G. and Rao, P. N. 2021. "Estimation of wind pressure coefficients on multi-building configurations using data-driven approach." *Wind Struct*., 32(2), 127-142. https://doi.org/10.12989/was.2021.32.2.127

Kossin, J. P. 2018. "A global slowdown of tropical-cyclone translation speed." *Nature*, 558, 104-107. https://doi.org/10.1038/s41586-018-0158-3

Krizhevsky, A., Sutskever, I. and Hinton, G. 2012. "ImageNet classification with deep convolutional neural networks. " *In Proc., Advances in Neural Information Processing Systems* 25, 1090–1098.

Kutler P. and Mehta U. 1984. "Computational aerodynamics and artificial intelligence." *In Proc., 17th Fluid Dynamics, Plasma Dynamics, and Lasers Conference*, 1531, Snowmass, CO. https://doi.org/10.2514/6.1984-1531

Landsea, C. W., Feuer, S., Hagen, A., Glenn, D. A., Sims, J., Perez, R., Chenowethm, M.,and Anderson, N. 2012. "A reanalysis of the 1921–30 Atlantic hurricane database." *J. Clim*., 25(3), 865-885. https://doi.org/10.1175/JCLI-D-11-00026.1

LeCun, Y., Bengio, Y. and Hinton, G. 2015. "Deep learning. " *Nature*, 521(7553), 436-444. https://doi.org/10.1038/nature14539

Li, SH., Hong, HP. 2016. "Typhoon wind hazard estimation for China using an empirical track model. " *Natural Hazards*.82:1009-29.

Li, Y., and Ellingwood, B. R. 2006, "Hurricane damage to residential construction in the US: Importance of uncertainty modelling in risk assessment," *Eng. Struct*. 28(7), 1009-1018. https://doi.org/10.1016/j.engstruct.2005.11.005

Li, Y. and Ellingwood, B. R. 2009, "Framework for multi-hazard risk assessment and mitigation for wood-frame residential construction." *J. Struct. Eng*. 135(2), 159-168. https://doi.org/10.1061/

(ASCE) 0733-9445(2009)135:2(159)

Liu, J., and Niu, J. 2016. "CFD simulation of the wind environment around an isolated high-rise building: An evaluation of SRANS, LES and DES models. " *Build Environ*, 96, 91-106.

Lophaven SN, Nielsen HB and Søndergaard J. 2002. " Aspects of the matlab toolbox DACE. IMM, Informatics and Mathematical Modelling." The Technical University of Denmark.

Lin, J.X., Surry, D., and Tieleman, H.W. 1995. "The distribution of pressure near roof corners of flat roof low buildings." *J. Wind Eng. Ind. Aerodyn*., 56, 235-265. https://doi.org/10.1016/0167-6105(94)00089-V

Lin, N., 2005. "Simulation of windborne debris trajectories. " PhD thesis. Princeton University. Princeton, NJ

Lin, N., Letchford, C. and Holmes, J.D. 2006. "Investigations of plate-type windborne debris. Part I. Experiments in wind tunnel and full scale" *J. Wind Eng. Ind. Aerodyn*., 94, 51-76. https://doi.org/10.1016/j.jweia.2005.12.005

Manning, B. R., and Nichols, G. G. 1991. "Hugo-lessons learned. " *In Proc., Hurricane Hugo One Year Later*, 186–194, Reston, VA: ASCE.

McAllister, T. P. 2016. "Research needs for developing a risk-Informed methodology for community resilience. " *J. Struct. Eng.*, 142(8): C4015008. https://doi.org/10.1061/(ASCE)ST.1943-541X.0001379.

Mei, W., Pasquero, C., and Primeau, F. 2012. "The effect of translation speed upon the intensity of tropical cyclones over the tropical ocean. " *Geophys. Res. Lett*., 39(7). https://doi.org/10.1029/2011GL050765

Meng, Y., and HIBI, K. 1998. "Turbulent measurements of the flow field around high-rise buildings."[In Japanese.] *Wind Engineers, JAWE,* 76. 55-64. https://doi.org/10.5359/jawe.1998.76_55

Meroney, R. N., Leitl, B. M., Rafailidis, S., and Schatzmann, M. 1999. "Wind-tunnel and numerical modeling of flow and dispersion about several building shapes." *J. Wind Eng. Ind. Aerodyn.*, 81(1-3), 333-345. https://doi.org/10.1016/S0167-6105(99)00028-8

Minor, J.E. 1994. "Wind-Borne Debris and the Building Envelope." *J. Wind Eng. Ind. Aerodyn.*, 53, 207-227. https://doi.org/10.1016/0167-6105(94)90027-2

Minor, J. E. 2005. "Lessons learned from failures of the building envelope in windstorms." *J. Archit. Eng.*, 11(1), 10–13. https://doi.org/10.1061/(ASCE)1076-0431(2005)11:1(10)

Moghim, F., Xia, F. T., and Caracoglia, L. 2015. "Experimental analysis of a stochastic model for estimating wind-borne compact debris trajectory in turbulent winds." *J. Fluids Struct.*, 54, 900-924. https://doi.org/10.1016/j.jfluidstructs.2015.02.007

Morris, M. D. 1991. "Factorial sampling plans for preliminary computational experiments." *Technometrics*, 33(2), 161-174. https://doi.org/10.1080/00401706.1991.10484804

Neunlist, J.B. 1983. "Questionnaire for glass industries." Report to Building Code Review Committee, Construction Industry Council, Houston, TX.

NOAA. (2020). Historical hurricane tracks tool. Available at: https://coast.noaa .gov/hurricanes/#map/ (Accessed April 5, 2023).

Noda, M. and Nagao, F. 2010. "Simulation of 6DOF motion of 3D flying debris. " *In Proc., 5th International Symposium on Computational Wind Engineering*, 23-27. Chapel Hill, North Carolina, USA.

Ouyang, Z., and Spence, S. M. 2020. "A performance-based wind engineering framework for envelope systems of engineered buildings subject to directional wind and rain hazards. " *J. Struct.*

Eng., 146(5), 04020049. https://doi.org/10.1061/(ASCE)ST.1943-541X.0002568

Porter, K., Farokhnia, K., Vamvatksikos, D., and Cho. I. 2015. "Guidelines for Component-Based Analytical Vulnerability Assessment of Buildings and Nonstructural Elements." Accessed June 2, 2022. http://www.sparisk.com/pubs/Porter-2015-GEM-Analytical-Vulnerability.pdf

Powell, M. D., Houston, S. H., Amat, L. R., and Morisseau-Leroy, N. 1998. "The HRD real-time hurricane wind analysis system." *J. Wind Eng. Ind. Aerodyn*., 77–78, 53–64. https://doi.org/10.1016/S0167-6105(98)00131-7

Powell, M. D., Murillo, S., Dodge, P., Uhlhorn, E., Gamache, J., Cardone, V., Cox, A., Otero, S., Carrasco, N., Annane, B., and Fleur, R. S. 2010. "Reconstruction of Hurricane Katrina's wind fields for storm surge and wave hindcasting." *Ocean Eng*., 37(1), 26-36. https://doi.org/10.1016/j.oceaneng.2009.08.014.

Rai, M.M. and Madavan, N.K. 2001. "Application of artificial neural networks to the design of turbomachinery airfoils" J. Propul. Power., 17 (1), 176-183. https://doi.org/10.2514/2.5725

Richards, P. J., Williams, N., Laing, B., McCarty, M., and Pond, M. 2008. "Numerical calculation of the three-dimensional motion of wind-borne debris." *J. Wind Eng. Ind. Aerodyn.*, 96(10-11), 2188-2202. https://doi.org/10.1016/j.jweia.2008.02.060

Rose, S., and Apt, J. 2012. "Generating wind time series as a hybrid of measured and simulated data." *Wind Energy*, 15(5), 699-715. https://doi.org/10.1002/we.499

Rosowsky, D. V., and Ellingwood, B. R. 2002. "Performance-based engineering of wood frame housing: Fragility analysis methodology. " *J. Struct. Eng*., 128(1), 32-38. https://doi.org/10.1061/(ASCE)0733-9445(2002)128:1(32)

Shinozuka, M., Feng, M.Q., Lee, J., and Naganuma, T. 2000. "Statistical analysis of fragility curves. " *J. Eng. Mech*. 126(12), 1224-1231. https://doi.org/10.1061/(ASCE)0733-9399(2000)

126:12(1224)

Simiu, E., Changery, M. J., and Filliben, J. J. 1979. "Extreme wind speeds at 129 stations in the contiguous United States". US Department of Commerce, National Bureau of Standards. 118.

Simiu, E., Vickery, P., and Kareem, A. 2007. "Relation between Saffir–Simpson hurricane scale wind speeds and peak 3-s gust speeds over open terrain." *J. Struct. Eng*., 133(7), 1043-1045. https://doi.org/10. 1061/(ASCE)0733-9445(2007)133:7(1043)

Simiu, E., and Yeo, D. 2019. *Wind effects on structures: Modern structural design for wind*. 4th ed, Hoboken, NJ: John Wiley & Sons.

Singhal, A. and Kiremidjian, A.S. 1996. "Methods for probabilistic evaluation of seismic structural damage. " *J. Struct. Eng*., 122(12), 1459-1467. https://doi.org/10.1061/(ASCE)0733-9445(1996) 122:12(1459)

Snaiki, R., Wu, T., Whittaker, A. S., and Atkinson, J. F. 2020. "Hurricane wind and storm surge effects on coastal bridges under a changing climate." *Transp. Res. Rec*., 2674(6), 23-32. https://doi.org/10.1177%2F0361198120917671

Solari, G., and Tubino, F. 2002. "A turbulence model based on principal components." *Probabilistic Eng. Mech*., 17(4), 327-335. https://doi.org/10.1016/S0266-8920(02)00016-4

Sparks, P.R., Schiff, S.D., and Reinhold, T.A. 1994. "Wind damage to envelopes of houses and consequent insurance losses." *J. Wind Eng. Ind. Aerodyn*., 53(1-2), 145–155. http://dx.doi.org/10.1016/0167-6105(94)90023-X

Tachikawa, M. 1983. "Trajectories of flat plates in uniform flow with application to wind-generated missiles. " *J. Wind Eng. Ind. Aerod*., 14(1-3), 443-453. https://doi.org/10.1016/0167-6105(83)90045-4

Tachikawa, M. 1988. "A method for estimating the distribution range of trajectories of wind-borne missiles. " *J. Wind Eng. Ind. Aerod.*, 29 (1-3), 175-184. https://doi.org/10.1016/0167-6105(88)90156-0

Taichi S., Yoshihide T., Ryuichiro Y., Akashi M., Hiroshi Y., Hiroto K. and Tsuyoshi N. 2003. "Development of cfd method for predicting wind environment around a high-rise building: Part2: The cross comparison of CFD results using various k-ε models for the flowfield around a building model with 4:4:1 shape." [In Japanese.] *AIJ J. Technol. Des*., 9(18),169-174. https://doi.org/10.31 30/aijt.9.1 69_2

Teo, C., Lim, K., Hong, G. and Yeo M. 1991. "A neural net approach in analyzing photograph in PIV*" In Proc., 1991 IEEE International Conference on Systems*, Man, and Cybernetics, 1535-1538. https://doi.org/10.1109/icsmc.1991.169906

Thibault, J. and Grandjean, B.P. 1991. "A neural network methodology for heat transfer data analysis." *Int. J. Heat Mass Transfer*., 34 (8), 2063-2070. https://doi.org/10.1016/0017-9310(91)90217-3

Thordal, M. S., Bennetsen, J. C., and Koss, H. H. H. 2019. "Review for practical application of CFD for the determination of wind load on high-rise buildings". *J. Wind Eng. Ind. Aerod*., 186, 155-168. https://doi.org/10.1016/j.jweia.2018.12.019

Tryggeson, H., and Lyberg, M. D. 2010. "Stationary vortices attached to flat roofs." *J. Wind Eng. Ind. Aerodyn.*, 98(1), 47-54. https://doi.or g/10.1016/j.jweia.2009.09.001

Twisdale, L.A., Vickery, P.J. and Steckley, A.C. 1996. "Analysis of hurricane windborne debris impact risk for residential structures. " Report 5303, Applied Research Associates, Inc. Raleigh, NC, USA.

U.S. Geological Survey. 2014. U.S.G.S. Unified Hazard Tool. Accessed December 29, 2021. https://earthquake.usgs.gov/hazards/interactive/

Uhlhorn, EW., Black, PG., Franklin, JL., Goodberlet, M., Carswell, J. and Goldstein, AS. 2007"Hurricane surface wind measurements from an operational stepped frequency microwave radiometer. " *Mon Weather Rev*. 135(9):3070-85.

van de Lindt, J. W., Graettinger, A., Gupta, R., Skaggs, T., Pryor, S., and Fridley, K. J. 2007. "Performance of wood-frame structures during Hurricane Katrina." *J. Perform. Constr. Facil*., 21(2), 108–116. https://doi.org/10.1061/(ASCE)0887-3828(2007)21:2(108)

van de Lindt, J. W., and Dao, T. N. 2009. "Performance-based wind engineering for wood-frame buildings." *J. Struct. Eng*., 135(2), 169-177. https://doi.org/10.1061/(ASCE)0733-9445(2009)135:2(169)

Vickery, P. J., and Twisdale, L. A. 1995. "Wind-field and filling models for hurricane wind-speed predictions. " *J. Struct. Eng*., 121(11), 1700-1709. https://doi.org/10.1061/(ASCE)0733-9445(1995)121:11(1700)

Vickery, P. J., Skerlj, P. F., and Twisdale, L. A. 2000a. "Simulation of hurricane risk in the US using empirical track model. " *J. Struct. Eng*., 126(10), 1222-1237. https://doi.org/10.1061/(ASCE)0733-9445(2000)126:10(1222)

Vickery, P. J., Skerlj, P. F., Steckley, A. C., and Twisdale, L. A. 2000b. "Hurricane wind field model for use in hurricane simulations. " *J. Struct. Eng*., 126(10), 1203-1221. https://doi.org/10.1061/(ASCE)0733-9445(2000)126:10(1203)

Vickery, P. J., and Wadhera, D. 2008. "Statistical models of Holland pressure profile parameter and radius to maximum winds of hurricanes from flight level pressure and H* wind data." *J. Appl. Meteorol. Climatol*., 47, 2497–2517. https://doi.org/10.1175/2008JAMC1837.1

Vickery, P. J., Skerlj, P. F., Lin, J., Twisdale, L. A., Young, M. A., and Lavelle, F. M. 2006. "HAZUS-MH hurricane model methodology. II: Damage and loss estimation." *Nat. Hazards Rev*., 7(2), 94–103. https://doi.org/10.1061/(ASCE)1527-6988(2006)7:2(94)

Vickery, P. J., Wadhera, D., Twisdale Jr, L. A., and Lavelle, F. M. 2009a. "U.S. Hurricane Wind Speed Risk and Uncertainty." *J. Struct. Eng*., 135(3), 301-320. https://doi.org/10.1061/(ASCE)0733-9445(2009)135:3(301)

Vickery, P. J., Wadhera, D., Powell, M. D., and Chen, Y. 2009b. "A hurricane boundary layer and wind field model for use in engineering applications. " *J. Appl. Meteorol. Climatol*., 48(2), 381-405. https://doi.org/10.1175/2008JAMC1841.1

Vickery, P. J., Masters, F. J., Powell, M. D., and Wadhera, D. 2009c. "Hurricane hazard modeling: The past, present, and future. " *J. Wind Eng. Ind. Aerodyn*., 97(7-8), 392-405. https://doi.org/10.1016/j.jweia.2009.05.005

Wang, H., and Wu, T. 2022. "Statistical investigation of wind duration using a refined hurricane track model." *J. Wind Eng. Ind. Aerodyn*., 221, 104908. https://doi.org/10.1016/j.jweia.2022.104908

Wang, K., Gou, C., Duan, Y., Lin, Y., Zheng, X. and Wang, F. Y. 2017. "Generative adversarial networks: introduction and outlook. " IEEE/CAA *J. Autom. Sin*., 4(4), 588-598. https://doi.org/10.1109/JAS.2017.7510583

Warey, A., Kaushik, S., Khalighi, B., Cruse, M. and Venkatesan, G. 2020. "Data-driven prediction of vehicle cabin thermal comfort: using machine learning and high-fidelity simulation results." Int. *J. Heat Mass Transf*., 148, 119083. https://doi.org/10.1016/j.ijheatmasstransfer.2019.119083

Yamashita, R., Nishio, M., Do, R. K. G., and Togashi, K. 2018. "Convolutional neural networks: an overview and application in radiology. " *Insights into imaging*. 9, 611-629.

Yoshie, R., Mochida, A., Tominaga, Y., Kataoka, H., Harimoto, K., Nozu, T., and Shirasawa, T. 2007. "Cooperative project for CFD prediction of pedestrian wind environment in the Architectural Institute of Japan." *J. Wind Eng. Ind. Aerodyn.*, 95(9-11), 1551-1578. https://doi.org/10.1016/j.jweia.2007.02.023

Yu, N., Yiu, N., Yu, Y., and Tsang, P. 2020. "Glass damages study in Hong Kong in Typhoon Mangkhut" In *Proc., 4th Hong Kong Wind Eng. Soc. Work*., Hong Kong, China.

Zhang L., Akiyama M., Huang K., Sugiyama H. and Ninomiya N. 1996. "Estimation of flow patterns by applying artificial neural networks" *In Proc., 1996 IEEE International Conference on Systems, Man and Cybernetics.* Information Intelligence and Systems (Cat. No. 96CH35929), 2, 1358-1363, Beijing, China. https://doi.org/10.1109/ICSMC.1996.571309

Zhang, T. H.and You, X. Y. 2013. "Applying neural networks to solve the inverse problem of indoor environment. " *Indoor Built Environ*., 23 (8), 1187-1195, https://doi.org/10.1177/1420326x13499596

APPENDIX A:

CALCULATION OF THE CENTRAL PRESSURE

The central pressure is replaced with the relative intensity parameter in the intensity model and the following calculation of central pressure is based on the definition of the relative intensity parameter (Darling 1991):

$$p_0 = 1013 + (1 - RH)e_s - I(1 - x)(1013 - (RH \times e_s) \tag{A.1}$$

$$e_s = 6.112 \exp\left\{\frac{17.67\left(T_s - 273\right)}{T_s - 29.5}\right\} \tag{A.2}$$

where p_0 = central pressure, RH = relative humidity of ambient air, taken to be 0.75, e_s = saturation vapor pressure, T_s = the sea surface temperature, I = the relative intensity parameter, x is the solution of the following nonlinear equation:

$$\ln(x) = -A\left[\frac{1}{x} - B\right] \tag{A.3}$$

where quantities A and B are defined as:

$$A = \frac{\frac{T_s - T_0}{T_s}\left[2.5 \times 10^6 - 2320(T_s - 273)\right]}{(1 - \frac{T_s - T_0}{T_s})R_v T_s (1013 - RH \times e_s)} \tag{A.4}$$

$$B = RH\left[1 + \frac{e_s \ln(RH)}{(1013 - RH \times e_s)A}\right] \tag{A.5}$$

where R_v = the gas constant of water vapor, taken to be 461 $J/(kg \cdot K)$ and T_0 = the temperature at the top of the troposphere, taken to be 203°K (Emanuel 1988).

APPENDIX B:

ADDITIONAL FIGURES AND TABLES

This appendix presents additional figures and tables involved in Chapter 3

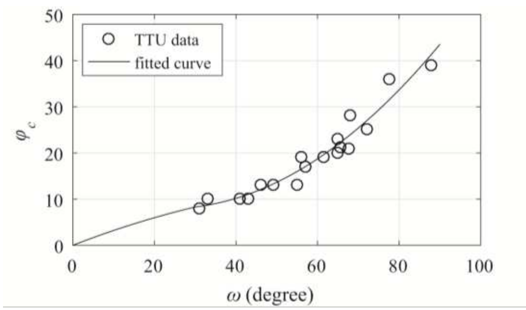

(a)

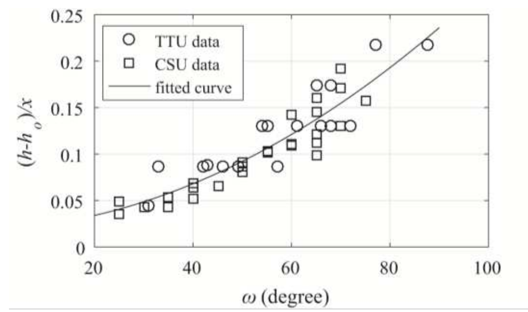

(b)

Figure B.1(a) ϕ_c and (b) h estimated by experimental data

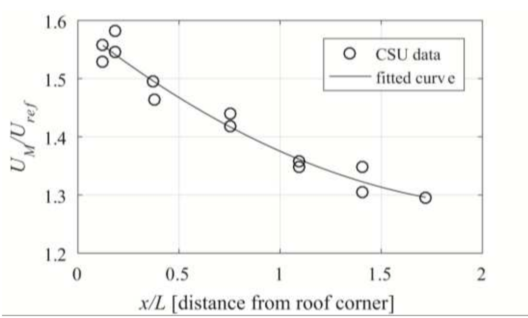

Figure B.2 “Speed-up ratio” estimated by experimental data

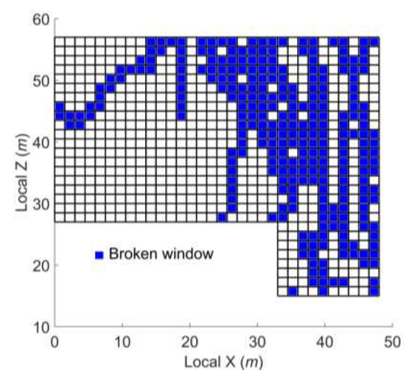

Figure B.3 Window damage without considering turbulence in the main flow

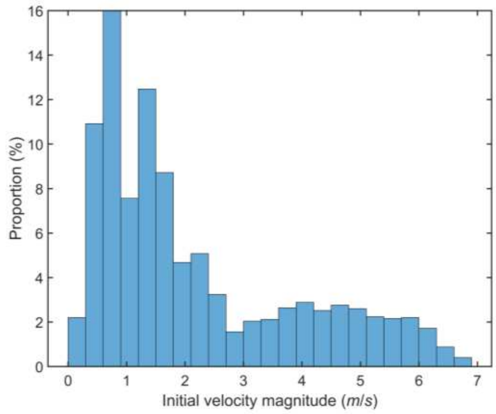

Figure B. 4 Histogram of initial velocity magnitude

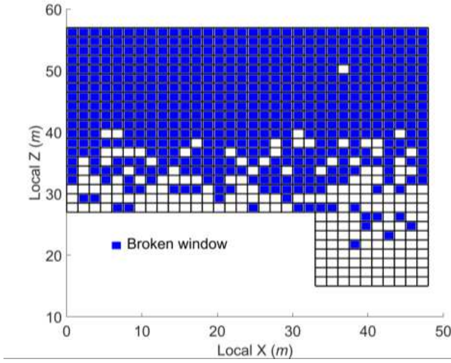

Figure B.5 Window damage without considering the wake effect

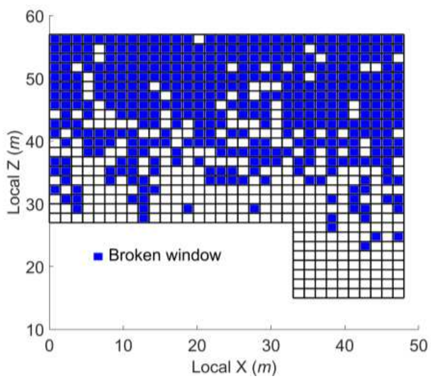

(a)

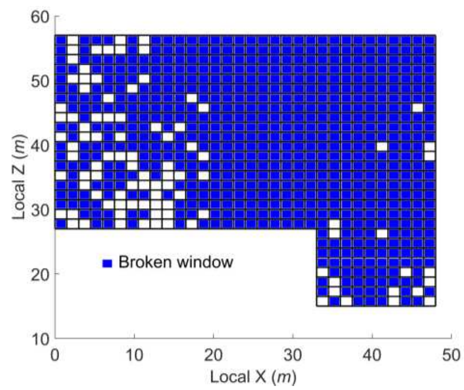

(b)

Figure B.6 Window damage caused by debris with different sizes (a) 12 *mm* (b) 15 *mm*

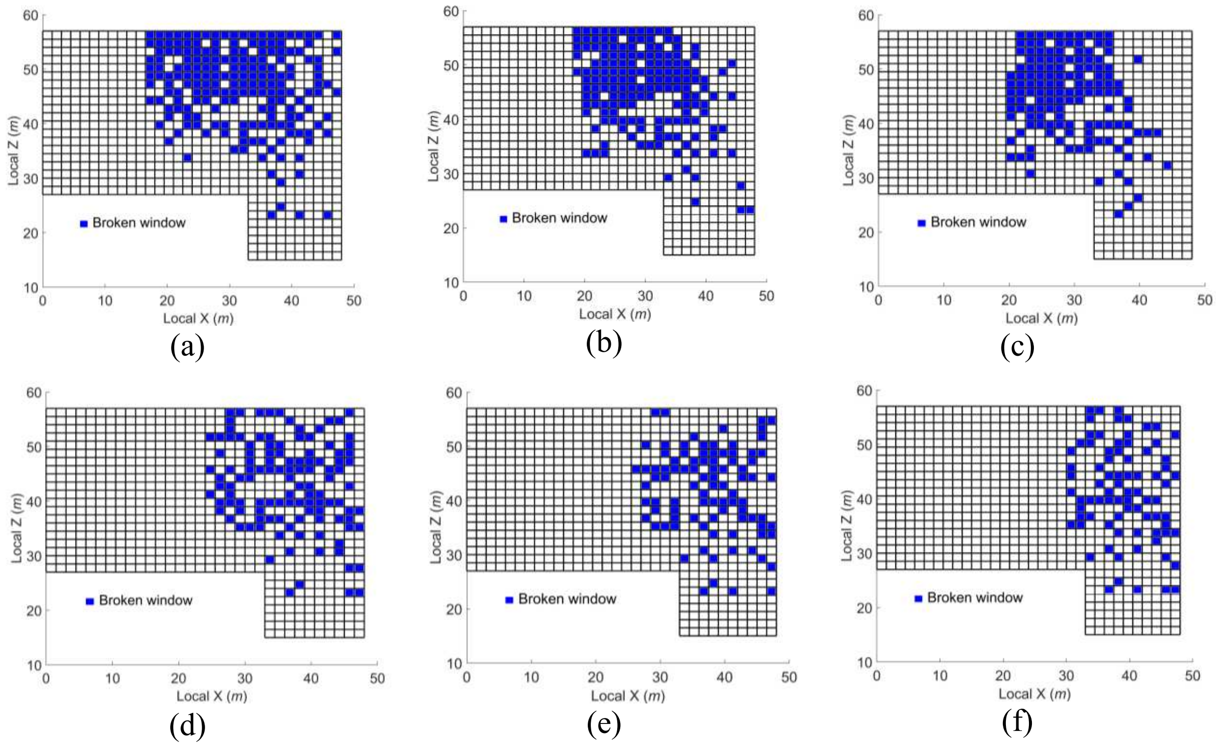

Figure B.7 Window damage caused by debris generated at different locations (a) location1 (b) location 2 (c) location 3 (d) location 4 (e) location 5 (f) location 6

Table B.1 Parametric model of the velocity profile for conical vortices

Range	Description	Velocity equation
$a=-1$	Roof surface	$U=0$
$-a_2 < a < -a_1$	Between roof and vortex core	$U(a) = -U_{a_2} \cdot \sqrt{a / -a_2}$
$\lvert a \rvert < a_1$	Viscous vortex core	$U(a) = U_{a_1} \cdot a / a_1$
$a_1 < a < a_2$	Vortex, above the core	$U(a) = U_{a_2} \cdot \sqrt{a / a_2}$
$a_2 < a < a_3$	Transition region	$U(a) = \dfrac{U_{\max} \cdot 2 \cdot (a / a_{\max})}{1 + (a / a_{\max})^2}$
$a_3 < a$	Potential flow region	$U(a) = U_{a_3} \sqrt{e^{\int_{a_3}^{a} \frac{-2}{(Rc/h)} dn'}}$

Note: $a_1 = 0.2$, $a_2 = 1$, $a_3 = 2$, $a_{\max} = 1.5$ and $U_{\max} = 1.05 U_M$

Table B.2 Comparison of the two approaches for considering turbulence

Method	x_m (m)	x_{std} (m)	z_m (m)	z_{std} (m)	V_{xm} (m/s)	V_{xstd} (m/s)	V_{zm} (m/s)	V_{zstd} (m/s)	T (s)
1	118.5	7.0	0.0	0.4	28.0	1.7	28.0	0.1	5.7
2	119.6	8.2	0.0	0.3	28.5	1.7	28.5	0.0	5.7